PHYSICS OF GEOLOGICAL PROCESSES
DEPARTMENT OF PHYSICS, UNIVERSITY OF OSLO, NORWAY

Andreas HAFVER

Drainage by fracturing: a mechanism for primary migration

THESIS SUBMITTED FOR THE DEGREE OF PHILOSOPHIA DOCTOR

October 29, 2014

Series of dissertations submitted to the
Faculty of Mathematics and Natural Sciences, University of Oslo
No. 1575

ISSN 1501-7710

Cover: Hanne Baadsgaard Utigard.
Printed in Norway: AIT Oslo AS.

Produced in co-operation with Akademika Publishing.
The thesis is produced by Akademika Publishing merely in connection with the thesis defence. Kindly direct all inquiries regarding the thesis to the copyright holder or the unit which grants the doctorate.

Principal supervisors:

Anders MALTHE-SØRENSSEN,
Physics of Geological Processes, University of Oslo, Norway;

Subsidiary supervisors:

Paul MEAKIN,
Physics of Geological Processes, University of Oslo, Norway
and
Department of Physics, Temple University, Philadelphia, USA

Bjørn JAMTVEIT,
Physics of Geological Processes, University of Oslo, Norway.

Acknowledgements

I submit this thesis after three and a half exciting and challenging years as a PhD student at the Physics of Geological Processes institute (PGP) at the University of Oslo. Many people supported and guided me through this time, and I take this opportunity to thank them.

First of all, I would like to thank my supervisors, Anders Malthe-Sørenssen, Paul Meakin and Bjørn Jamtveit. Thank you, Anders, for always believing in me, encouraging me and pointing me in the right direction at times when I was struggling. Thank you, Paul, for sharing your vast knowledge with me and for helping me appreciate the wider context of my work. Thank you, Bjørn, for giving me the opportunity to be part of the creative research environment at PGP and for enabling me to carry out my research.

I would also like to express my appreciation to my other colleagues at PGP, and, in particular, to the people that I have worked closely with during these years. Thank you, Dag Kristian Dysthe and Maya Kobchenko, for involving me in your project with the gelatine experiments two years ago. Thank you, Dag Kristian, for always being available whenever I had things I needed to discuss, and for being someone that I could turn to for advice. Thanks also to Jens Feder, who always came by my office whenever he visited PGP. Thank you for the many interesting conversations we have had, for all your advice and for showing much interest in my work. I would also like to thank Ole Ivar Ulven, who started his PhD around the same time as me. Thank you for all the interesting lunchtime conversations as well as the many useful discussions around our respective projects. In addition, I would like to thank Jørgen Trømborg and Kjetil Thøgersen, my officemates for most of my time at PGP.

I also extend my gratitude to Espen Jettestuen at the International Research Institute of Stavanger, from whom I have learnt a lot during our weekly meetings. Many of the ideas that the papers in this thesis are based on were conceived or first discussed in the meetings with you, and I want to thank you for sharing

your ideas and advice.

My participation at the Wolfram Science Summer School in July 2013 was in many ways a turning point during my PhD time, and an experience that has significantly impacted my perspectives on science and research. I would like to thank the fellow summer school students and the staff from Wolfram Research, and in particular Stephen Wolfram, who enthusiastically listened to my ideas and helped me turn them into a concrete model. I would also like to thank Jan Baetens, who was my project supervisor at the summer school, and whom I have later continued collaboration with and visited at the University of Ghent. Thank you for hosting me in Belgium, for all your help with coding and writing, for taking such an interest in my work and for exposing me to your own work.

During this time at PGP I have been fortunate to have the support of my family and particularly my wife, Tandi. Thank you for being patient with me, believing in me and pushing me to accomplish this work.

Lastly, I would like to mention two people who have had an enormous impact on me, but whose lives ended tragically in two separate accidents during the course of my PhD. Xolisa Gomba was my closest friend during my student years in South Africa, and as a geologist he was excited to see me take the step into geoscience. Ntokozo Buthelezi was my "twin brother", born on the same day as me, on the 9th of March 1985, and I got to know him as an exchange student in my high school years. Both Xolisa and Ntokozo were exceptional and talented individuals who, despite difficult circumstances, already had achieved great things in their lives. They could both have accomplished so much more, and it is therefore with great admiration and respect that I dedicate this thesis to them.

Andreas Hafver Oslo, 03.07.2014

Contents

Introduction

1 General context

The main focus of this thesis is primary migration - how oil and gas is transported through and expelled from the source rock in which it is generated by thermal decomposition of organic matter. This topic, which is discussed in more detail in section 4, can be viewed in a broader context, as an example of a process where the generation and transport of a fluid inside a porous medium is coupled mechanically to deformation and fracturing of the host medium. Such phenomena are common in both natural and engineered systems, and the coupling mechanisms can be manyfold. In some systems, the fluid, which may either be trapped inside, injected into, migrating through or draining from the solid, may act mechanically on the solid via fluid pressure forces exerted on external or internal surfaces. In other systems the coupling may be mediated by chemical or thermal interactions between the fluid and solid components, which causes the solid to expand or contract [1] and induces stresses that may lead to fracturing. The fluid may also undergo phase transitions within the porous host medium, generating stresses as crystals grow from a supersaturated or supercooled liquid [2, 3] or as the pressure of exsolved gases accumulates in the pore space. While the fluid may drive deformation and fracturing of the solid, fracturing may also affect transport and provide new migration pathways for the fluid to drain from or enter the system. This may, in turn, inhibit further fracturing, by relieving fluid pressure, or accelerate fracturing, for example by increasing the supply of fluid available for volume-changing chemical reactions. Evidently, these are complex processes which can lead to varied and rich dynamics.

Geology provides a range of examples of coupled transport, deformation and fracturing processes, occurring on every scale. Water, wind and ice shape the surface of our planet, on large scales by erosion and on smaller scales by weathering of exposed rocks. In the subsurface, the transport, consumption

and production of fluids control metamorphic transformation of rocks, which in turn determines the composition of the lithosphere, from the nanometer to tectonic scale [4]. The fluid released by dehydration of subducting rocks may induce sufficient pressure to trigger earthquakes [5]. Another geological example, where drainage of fluid is associated with fracturing, is the decomposition of methane hydrate in sediments [6], which may play a significant role in the carbon cycle. Fluid magma penetrating the Earth's crust in explosive volcanic events is a large-scale example, and even if the magma cannot reach the surface, intrusive complexes of dikes and sills permeate the subsurface and can serve as an energy source for other geological processes. For example, the heat from magmatic complexes can trigger the release of over-pressured fluids from clay or organic rich sediments, manifested in the form of mud volcanoes [7]. Similarly, hydrothermal vents may be formed when organic rich and wet rock is heated by magmatic intrusions, and this could be an important source of hydrocarbon emissions, which can impact our climate and may have contributed to massive extinctions in the past [8, 9]. The slow heating of sedimentary rock during burial may drive decomposition of organic contents into hydrocarbons of lower density, and it is believed that fracturing is an important mechanism of primary migration, which allows the oil and gas to migrate into distant reservoirs [10, 11, 12].

Understanding coupled processes like these is important, from environmental, safety and economic perspectives. For example, the infiltration of water into concrete could lead to formation of ice or salt crystals in the pore space, and is a cause of damage to constructions [2, 3]. Fracturing of nuclear fuel pellets due to generation of fission gases is a challenge in the nuclear energy industry [13]. Understanding how chemical or nuclear waste is transported in and interact with rock formations is essential for evaluating contamination risks, and knowledge of how precipitation or irrigation water infiltrate soil is important for farming and for geological hazard assessment. Similarly, sequestration of CO_2 by injection into aquifers or petroleum reservoirs is a potential mitigation mechanism against global warming, but understanding the coupling to deformation and fracturing of the host rock is important in establishing the viability of storage sites [14]. For the oil and gas industry, understanding how petroleum resources migrate and accumulate in the subsurface is essential in predicting commercial prospects of basins and to increase exploration success.

Over the past decades, hydraulic fracturing by injection of fluids has become a popular technology for extracting oil and gas from tight shales. This technology is driving a major shift in energy markets, which is impacting on the world's geopolitical balance. However, there is wide concern in the public and among professionals that the method may be associated with undesirable environmental and health risks [15, 16].

As mentioned above, this thesis was primarily motivated by an interest in the primary migration problem, however, it may also be relevant to several of the other examples mentioned above. The scientific contributions of the thesis are contained in a collection of six enclosed papers. The remainder of this introduction provides relevant background information, and is structured as follows: The next two sections provide brief introductions to the mechanics (section 2) and mechanisms of fluid migration (section 3) in porous solids. Primary migration, and the mechanisms by which it may happen, are then reviewed in section 4. Section 5 outlines the scope of the thesis and provides an overview of the papers.

2 Mechanics of porous solids

In this section, the basics of solid mechanics is reviewed and related to porous solids, and rock in particular. The intention is not to cover every detail of the subject, but rather to convey the background theory relevant for the applications in this thesis. For a more complete account of solid mechanics and the theory of elasticity, the reader may wish to confer sources such as the book by Landau and Lifshitz [17]. Poromechanics is reviewed in detail by Coussy [18]. A survey of fracture mechanics is provided by Anderson [19], and an account of elasticity and fracture mechanics in the context of geology is given by Pollard and Fletcher [20].

2.1 Displacement and the strain tensor

The configuration of a solid body may be described by the position of the points in the body. Suppose the initial position of a point is $\vec{X}$ and that the current position of the same point, after deformation, is $\vec{x}$. The current position is a function of the initial position, i.e. $\vec{x} = \vec{x}(\vec{X})$, and one may define a displacement field, quantifying the motion of the point relative to its original position, as

$$\vec{u}(\vec{X}) = \vec{x}(\vec{X}) - \vec{X}. \tag{1}$$

Consider two points, initially at positions $\vec{X}$ and $\vec{X}' = \vec{X} + d\vec{X}$, where $d\vec{X}$ is a small separation. After deformation, the separation of the two points is

$$\begin{aligned} d\vec{x} &= (\vec{X}' + \vec{u}(\vec{X}')) - (\vec{X} + \vec{u}(\vec{X})) \\ &= (\vec{X}' - \vec{X}) + (\vec{u}(\vec{X}') - \vec{u}(\vec{X})) \\ &= d\vec{X} + d\vec{u}, \end{aligned} \tag{2}$$

where $d\vec{u} = \vec{u}(\vec{X}') - \vec{u}(\vec{X})$. If $d\vec{u}$ is small, it may be approximated by its first order Taylor expansion around the point $\vec{X}$,

$$\begin{aligned} d\vec{u} &= \vec{u}(\vec{X}') - \vec{u}(\vec{X}) \\ &= \vec{u}(\vec{X}) + \nabla_{\vec{X}}\vec{u}(\vec{X}) \cdot d\vec{X} - \vec{u}(\vec{X}) \\ &= \nabla_{\vec{X}}\vec{u}(\vec{X}) \cdot d\vec{X}, \end{aligned} \tag{3}$$

where $\nabla_{\vec{X}}$ denotes the gradient with respect to the initial configuration. Hence,

equation 2 may be expressed as

$$d\vec{x} = F(\vec{X}) \cdot d\vec{X}, \tag{4}$$

where $F(\vec{X}) = I + \nabla_{\vec{X}} \vec{u}(\vec{X})$ is the second order deformation tensor field.

Local deformation can be quantified by how two points $\vec{X}^1 = \vec{X} + d\vec{X}^1$ and $\vec{X}^2 = \vec{X} + d\vec{X}^2$, near position $\vec{X}$ in the undeformed solid, transform relative to each other. According to equation 4, the separation vectors after deformation are $d\vec{x}^1 = F(\vec{X}) \cdot d\vec{X}^1$ and $d\vec{x}^2 = F(\vec{X}) \cdot d\vec{X}^2$, and the scalar product of these deformed vectors becomes

$$\begin{aligned} d\vec{x}^1 \cdot d\vec{x}^2 &= d\vec{X}^1 \cdot F(\vec{X})^T F(\vec{X}) \cdot d\vec{X}^2 \\ &= d\vec{X}^1 \cdot \Big[I + (\nabla_{\vec{X}} \vec{u}(\vec{X}))^T + \nabla_{\vec{X}} \vec{u}(\vec{X}) \\ &\quad + (\nabla_{\vec{X}} \vec{u}(\vec{X}))^T \nabla_{\vec{X}} \vec{u}(\vec{X}) \Big] \cdot d\vec{X}^2 \\ &\approx d\vec{X}^2 \cdot \Big(I + (\nabla_{\vec{X}} \vec{u}(\vec{X}))^T + \nabla_{\vec{X}} \vec{u}(\vec{X}) \Big) \cdot d\vec{X}^2. \end{aligned} \tag{5}$$

In the last step, it was assumed that he deformation is small, such that the second order term may be ignored. Equation 5 can be written as

$$d\vec{x}^1 \cdot d\vec{x}^2 = d\vec{X}^1 \cdot \Big(I + 2\varepsilon(\vec{X}) \Big) \cdot d\vec{X}^2, \tag{6}$$

where $\varepsilon(\vec{X})$ is a second order strain tensor field, defined by

$$\varepsilon(\vec{X}) = \frac{1}{2} \Big(\nabla_{\vec{X}} \vec{u}(\vec{X})^T + \nabla_{\vec{X}} \vec{u}(\vec{X}) \Big). \tag{7}$$

The strain tensor field contains information about local deformation, and, from the definition, it is evident that it is symmetric. Hence, there are three independent strain components in two dimensions, and six in three dimensions. The individual tensor elements of the strain field at a point $\vec{X}$ may be expressed explicitly as

$$\varepsilon_{i,j}(\vec{X}) = \frac{1}{2} \left(\frac{\partial u_i}{\partial X_j} + \frac{\partial u_j}{\partial X_i} \right). \tag{8}$$

The stress tensor ε may be diagonalised by expressing it in the coordinate system of its three orthogonal eigenvectors. The form of the stress tensor is

then, in terms of the eigen strains $\{\varepsilon_1, \varepsilon_2, \varepsilon_3\}$,

$$\varepsilon = \begin{pmatrix} \varepsilon_1 & 0 & 0 \\ 0 & \varepsilon_2 & 0 \\ 0 & 0 & \varepsilon_3 \end{pmatrix}. \tag{9}$$

Using equation 6 in the eigenbasis and assuming that $d\vec{X}_i$ is a vector along the i^{th} eigen direction, one finds $|d\vec{x}_i| = \sqrt{1-2\varepsilon_i}|d\vec{X}_i| \approx (1+\varepsilon_i)\,|d\vec{X}_i|$. Hence, an infinitesimal volume, $V = d\vec{X}_1 \cdot (d\vec{X}_2 \times d\vec{X}_3)$, around the point $\vec{X}$ in the undeformed solid will deform to a volume $v = d\vec{x}_1 \cdot (d\vec{x}_2 \times d\vec{x}_3) = V(1+\varepsilon_1)(1+\varepsilon_2)(1+\varepsilon_3) \approx (1+\varepsilon_1+\varepsilon_2+\varepsilon_3) = (1+tr(\varepsilon))V$. The quantity

$$\epsilon = tr(\varepsilon) = \sum_{i=1}^{3} \varepsilon_{i,i}, \tag{10}$$

is termed volumetric strain, and is an invariant of the strain tensor which quantifies the local volume change (expansion or contraction) due to deformation.

2.2 The stress tensor

If a system is in mechanical equilibrium, the resultant force on any part of it must vanish. Consider the total force on a small volume Ω,

$$\vec{F} = \int_{\Omega} \vec{f}(\vec{X})\, dV, \tag{11}$$

where $\vec{f}(\vec{X})$ is the force per unit volume, and $\vec{f}(\vec{X})\, dV$ is the force on a volume element dV around the point $\vec{X}$. According to Newton's third law, if two volume elements dV_1 and dV_2 share an interface, they will exert equal and opposite forces on each other. As a consequence, it should be possible to rewrite equation 11 in terms of surface forces, and this can be done if $\vec{f}(\vec{X})$ is the divergence of a rank two tensor field, i.e.

$$\vec{f}(\vec{X}) = \nabla_{\vec{X}} \cdot \sigma(\vec{X}). \tag{12}$$

Using the divergence theorem one may then write equation 11 as

$$\vec{F} = \int_{\partial\Omega} \sigma(\vec{X}) \cdot d\vec{S}, \tag{13}$$

where $\partial\Omega$ is the boundary of the volume Ω and $d\vec{S}$ is the surface normal vector at any point on this boundary. In terms of individual components, equation 13 may be expressed as

$$F_i = \int_{\partial\Omega} \sum_{j=1}^{3} \sigma_{i,j}(\vec{X})\, dS_j. \tag{14}$$

From this one can see how σ, which is called the stress tensor, may be interpreted: $\sigma_{i,j}$ is the force per area in the i^{th} direction, on a unit surface with surface vector pointing in the j^{th} direction. This is illustrated in figure 1. By requiring conservation of moments, it may be shown that σ must be symmetric, i.e. $\sigma_{i,j} = \sigma_{j,i}$.

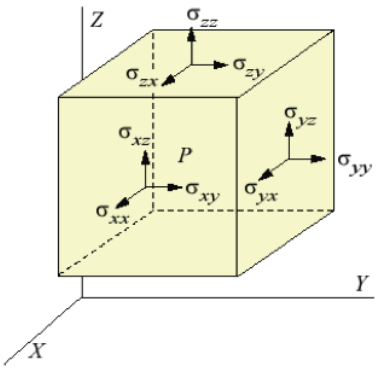

Figure 1: Interpretation of the components of the stress tensor.

The internal stresses and strains in a body may be determined from the boundary conditions. If the boundary forces at a point on the boundary is $\vec{P}$, mechanical equilibrium dictates that

$$\vec{P} - \sigma \cdot \hat{n} = 0, \tag{15}$$

where $\hat{n}$ is the normal vector at the given surface point.

σ may be diagonalised by expressing it in the coordinate system defined by its three orthogonal eigenvectors. The set of eigenvalues, $\{\sigma_1, \sigma_2, \sigma_3\}$, is called the set of principal stress components, and it is convention to sort the principal components such that $\sigma_1 \geq \sigma_2 \geq \sigma_3$. The stress state may be displayed as an ellipsoid with axes defined by the principal vectors (eigenvectors) and corresponding radii given by the principal components, as illustrated in figure 2A. Alternatively, it may be visualised in a Mohr diagram (figure 2B), which makes

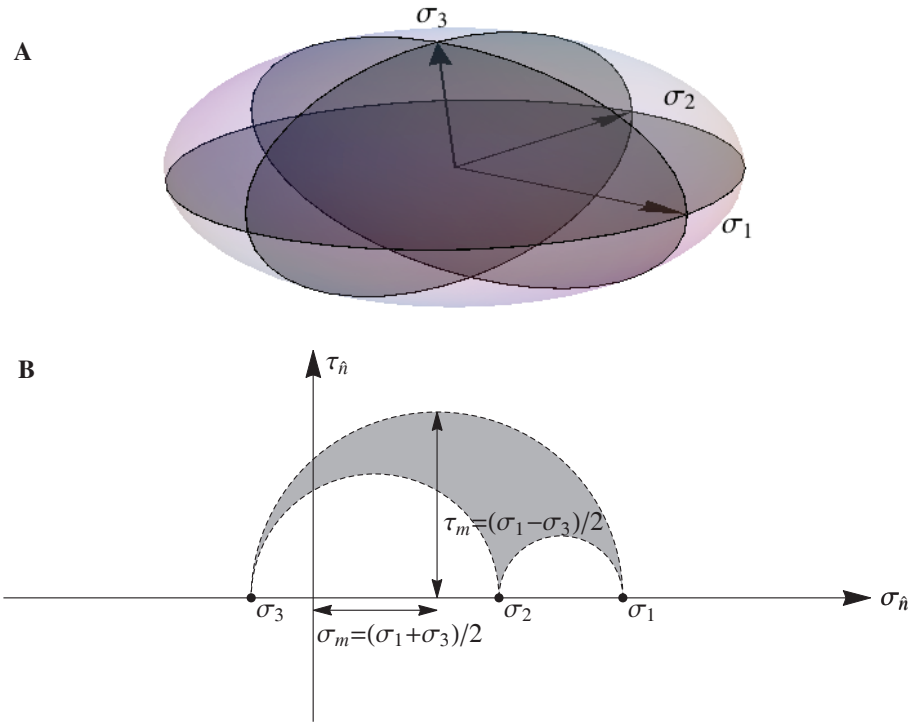

Figure 2: Visual representations of the stress state at a point. **A:** Stress ellipsoid, with axes are pointing in the principal stress directions and radii scaled by the principal components of the stress tensor; **B:** Mohr circle representation, in terms of normal stress, $\sigma_{\hat{n}}$, and shear stress, $\tau_{\hat{n}}$.

the shear and tensile components of the stress explicit. For any surface with normal vector $\hat{n}$ in a body, one may define the traction vector

$$\vec{T}_{\hat{n}} = \sigma \cdot \hat{n}. \tag{16}$$

The magnitude of the traction in direction $\hat{n}$ and in the plane perpendicular to it, are $\sigma_{\hat{n}}$ and $\tau_{\hat{n}}$, respectively. It may be shown that for any $\hat{n}$, the traction components $(\sigma_{\hat{n}}, \tau_{\hat{n}})$ will lie within the gray region in figure 2B.

2.3 Deformation and thermodynamics

The work required to induce a certain deformation may be related to the stress and strain fields. Suppose the displacement field $\vec{u}(\vec{X})$ of a deformed body is perturbed so that the new displacement field is $\vec{u}'(\vec{X}) = \vec{u}(\vec{X}) + \delta\vec{u}(\vec{X})$. The

work performed per unit volume is then given by

$$\delta W(\vec{X}) = \vec{f}(\vec{X}) \cdot \delta\vec{u}(\vec{X}). \tag{17}$$

Hence, the total work done on a volume Ω is

$$\begin{aligned} W &= \int_\Omega \delta W(\vec{X})\, dV \\ &= \int_\Omega \vec{f}(\vec{X}) \cdot \delta\vec{u}(\vec{X})\, dV \\ &= \int_\Omega \left(\vec{\nabla}_{\vec{X}} \cdot \sigma(\vec{X})\right) \cdot \delta\vec{u}(\vec{X})\, dV \\ &= \int_{\partial\Omega} \delta\vec{u}(\vec{X})\sigma(\vec{X}) \cdot d\vec{S} - \int_\Omega \sigma(\vec{X}) : \delta\left(\nabla_{\vec{X}}\vec{u}(\vec{X})\right)\, dV. \end{aligned} \tag{18}$$

Because of the symmetry of σ, we may substitute $\nabla_{\vec{X}}\vec{u}(\vec{X})$ in the last line with the strain tensor field, equation7. Furthermore, if the volume is considered to be infinite and the displacements vanish at infinity, the first term may be eliminated. The work, W, can then be expressed in terms of the stress and strain fields as

$$W = -\int_\Omega \sigma(\vec{X}) : \delta\varepsilon(\vec{X}). \tag{19}$$

W is the work done by internal stresses, and therefore, $-W$ is the work performed by the surroundings to deform the body. If the body is elastic, it must, by definition, return to its original configuration when the loading is relieved, and W will then vanish, because $\delta\vec{u} \to 0$.

Conservation energy may be stated in terms of the first law of thermodynamics as

$$\delta E = T\delta S - \delta W = T\delta S - \sigma : \delta\varepsilon, \tag{20}$$

where δE is the internal energy per unit volume, T is the absolute temperature and δS is entropy change. For hydrostatic pressure, $\sigma_{i,j} = P\delta_{i,j}$, where $\delta_{i,j}$ is the Dirac delta function, and hence $\sigma : \delta\varepsilon = \sum_{i,j}^{3} \sigma_{i,j}\delta\varepsilon_{i,j} = P\sum_{i,j}^{3} \delta_{i,j}\delta\varepsilon_{i,j} = P\, tr(\delta\varepsilon) = P\delta\epsilon$. As noted in section 2.1, the volumetric strain, ϵ, quantifies local volume change, and therefore equation 20 can be stated in the more familiar form in terms of P and δV,

$$\delta E = T\delta S - \delta W = T\delta S - P\delta V. \tag{21}$$

The Helmholtz free energy is defined as $F = E - TS$, and therefore

$$\delta F = S\delta T - \sigma : \delta\varepsilon. \tag{22}$$

Similarly, the Gibbs free energy becomes

$$G = F - \sigma : \varepsilon. \tag{23}$$

The stress and strain can be obtained from these free energies by the relations

$$\sigma_{i,j} = \left(\frac{\partial E}{\partial \varepsilon_{i,j}}\right)_S = \left(\frac{\partial F}{\partial \varepsilon_{i,j}}\right)_T, \tag{24}$$

and

$$\varepsilon_{i,j} = \left(\frac{\partial G}{\partial \sigma_{i,j}}\right)_T. \tag{25}$$

2.4 Stress as a function of strain

If strains are assumed to be small, the Helmholtz free energy, F, may be approximated by a Taylor expansion in the components $\varepsilon_{i,j}$ around the undeformed state where $\varepsilon = 0$. From equation 24 it follows that such an expansion cannot have a linear term. Furthermore, since F is a scalar and must be a invariant under change of coordinate system, only invariant second order terms may be included. It may be shown that, to second order,

$$F(T, \varepsilon) = F_0(T, \varepsilon) + \frac{1}{2}\lambda_1 tr(\varepsilon)^2 + \lambda_2 tr(\varepsilon \cdot \varepsilon), \tag{26}$$

where λ_1 and λ_2 are called Lamé coefficients.

A different notation is often convenient, where contributions to the free energy due to pure compression or expansion are kept separate from contributions from shear deformation. This may be achieved by writing

$$\varepsilon = e + \frac{\epsilon}{3} I, \tag{27}$$

with

$$e = \left[\varepsilon - \frac{\epsilon}{3} I\right]. \tag{28}$$

$\epsilon = tr(\varepsilon)$, as defined in equation 10, so that the trace of e vanishes. This shows that e only contributes a shear component to the deformation. Using equation 27

in equation 26 yields

$$F(T, \epsilon, e) = F_0(T, \epsilon, e) + \frac{K}{2}\epsilon^2 + Gtr(e \cdot e), \tag{29}$$

where $K = \lambda_1 + \frac{2}{3}\lambda_2$ is called the bulk modulus, and $G = \lambda_2$ is the shear modulus *.

By means of equation 24 the relationship between stress and strain can be found by differentiation of $F(T, \epsilon, e)$:

$$\sigma = K\epsilon I + 2Ge, \tag{30}$$

whics is a linear expression in the strain components $\varepsilon_{i,j}$. This is the continuum extension of Hooke's law, namely that the deformation of an elastic medium is proportional to the force applied to it. Taking the trace of equation 30 yields

$$tr(\sigma)/3 = K\epsilon. \tag{31}$$

The interpretation of this is that compression/expansion is caused by the diagonal part of σ, and the volumetric strain ϵ is proportional to the average tensile/compressive stress, $tr(\sigma)/3$. Inserting equation 31 back in equation 30 and solving for e gives

$$e = \frac{1}{2G}s, \tag{32}$$

where

$$s = \sigma - \frac{1}{3}tr(\sigma), \tag{33}$$

is called the deviatoric stress tensor, and accounts for the shear component of the stress.

2.5 Poroelastic coupling

The fluids in the pore space of a porous solid may induce mechanical deformation by exerting pressure on the pore surfaces. The effect of this is that equations 31 and 32, which describe the stress-strain relationship in standard

*The shear modulus is commonly denoted by the symbol μ. The symbol G is used here, to avoid confusion with chemical potential and viscosity, which are denoted by μ in section 3.

theory of elasticity, are replaced by the (Biot) poroelastic state equations [18],

$$tr(\sigma)/3 = K\epsilon - bP; \tag{34a}$$

$$\psi = b\epsilon + P/N; \tag{34b}$$

$$s = 2Ge. \tag{34c}$$

Note that equation 34c is identical to equation 32 and not affected by the presence of pore pressure. Equation 31 is modified to equation 34a, where b is the Biot coefficient, which can range from 0 to 1. This shows that pore fluid pressure counteracts compressive tensile stress. In equation 34b, N is the modulus that relates the pore pressure to the change in porosity, ψ. It shows that increased fluid pressure may cause both compression of the solid and rise in porosity.

If the solid is nearly incompressible, any volume change in the system is manifested as porosity change. Under such conditions, equation 34b reduces to $\psi \approx \epsilon$, and $b \approx 1$. By defining an effective stress

$$\sigma^{\text{eff}} = \sigma + PI, \tag{35}$$

one may then rewrite equations 34a-34c as

$$tr(\sigma^{\text{eff}}) = 3K\epsilon; \tag{36a}$$

$$\psi = \epsilon; \tag{36b}$$

$$s = 2Ge. \tag{36c}$$

The displacements in the elastic body are related to the strain, which is proportional to the effective stress. According to this, an increase in pore fluid pressure is equivalent to reducing the confining pressure by the same magnitude.

2.6 Fracture mechanics

Elastic deformations, where the system return to its original configuration when loading is removed, is usually restricted to small strains. When strained beyond its elastic regime, a system may behave in different ways, depending on factors such as material properties, loading conditions and temperature. A solid may deform in a ductile manner, by plastic flow, or in a brittle manner, by fracturing. Rock is brittle near the surface, but tends to become more ductile at depth.

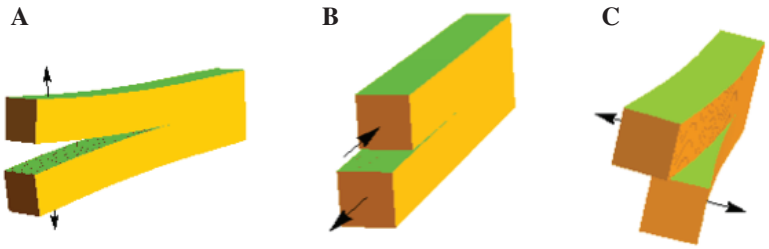

Figure 3: The three modes of fracturing: **A:** Mode I (opening mode); **B:** Mode II (sliding mode), and; **C:** Mode I (tearing mode).

The brittle/ductile transition depends on strain rate and rock type, and, in addition, fracturing and fracture healing on short length scales may result in ductile behaviour on long length scales.

Fracturing of brittle materials may happen in different modes, as illustrated in figure 3. In mode I, or opening mode, the opposing fracture surfaces are displaced normal to the fracture plane. This can result from tensile loading, i.e. stretching normal to the fracture plane. In contrast, shear fractures involve relative displacement of the fracture surfaces parallel to the fracture plane. Mode II fractures result from shear stress parallel to the plane of the fracture and perpendicular to the fracture front (tip). Mode III fractures, on the other hand, are activated by shear stresses parallel to both the fracture plane and the fracture front.

Since the failure of a material is independent of the choice of coordinate system, it is common to define fracture criteria in terms of principal stresses, $\sigma_1 \geq \sigma_2 \geq \sigma_3$. Among such criteria, the Mohr-Coulomb and Griffith criteria, discussed below, are most commonly used in geology and rock mechanics, and are found to agree well wit experiments [21, 20]. It should be noted, however, that a criterion of failure in terms of stress may be misleading. In reality it is the relative displacement of molecules in a body that cause bonds to break and leads to fracture, and this is more appropriately described by the strain field. In porous solids, subject to pore pressure, it is the effective stress that cause the strain, and, therefore, the subsequent fracturing. Hence, in the presence of pore pressure, the effective stress should be used when evaluating fracture criteria, such as the ones discussed below.

The Mohr-Coulomb fracture criterion

The Mohr-Coulomb criterion provides the condition for the formation of tensile or shear fractures in a given stress field. Tensile fractures is assumed to occur when the material is stretched beyond its tensile strength, T_C. Shear fracturing, on the other hand, is promoted by shear stress, but resisted by compressive stress.

Given a plane with normal vector $\hat{n}$, a traction vector can be defined according to equation 16. The magnitude of the tensile and shear components of the traction are, respectively,

$$\sigma_{\hat{n}} = \hat{n} \cdot \vec{T}_{\hat{n}} = \hat{n} \cdot \sigma \cdot \hat{n}, \tag{37}$$

and

$$\tau_{\hat{n}} = |\vec{T}_{\hat{n}} - \sigma_{\hat{n}} \hat{n}|. \tag{38}$$

The Mohr-Coulumb criterion states that tensile fracturing occurs along a plane with normal vector $\hat{n}$ if

$$\sigma_{\hat{n}} > T_c, \tag{39}$$

where σ_c is the tensile strength of the material. Otherwise, shear fracturing may occur if

$$\tau_{\hat{n}} > C + \sigma_{\hat{n}} \tan\theta. \tag{40}$$

In the latter inequality, C is the cohesion of the material, and θ is called the internal friction angle. Whether the conditions in equations 39 or 40 are met depends on the orientation of $\hat{n}$. However, $\sigma_{\hat{n}}$ and $\tau_{\hat{n}}$ for various orientations can be related to the principal stresses using a Mohr diagram, as shown in figure 2B. To predict failure, one may therefore check whether the Mohr circles intersect the Mohr-Coulomb failure envelope, as illustrated in figure 4. In the event of

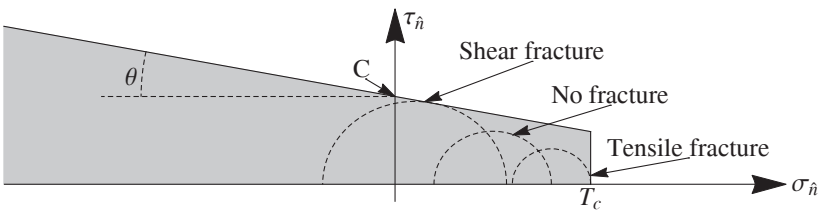

Figure 4: The Mohr-Coulomb failure envelope. The dashed circles correspond to the outermost circle in the Mohr circle diagram (figure 2 B).

fracture, the the fracture plane may also be recovered from the Mohr diagram in figure 2B.

The Griffith fracture criterion

Although the Mohr-Coulomb fracture criterion can be successfully fitted to experimental results, the cohesion and internal friction parameters can not be considered as real cohesion or friction. A more physically based criterion, that considers how fractures actually form is provided by Griffith [22].

Griffith realised that even under compression, the stress around a flaw in a material will be tensile at certain points. His fracture criterion is based on the assumption that a heterogenous material, such as rock, will contain many microflaws of various orientation (figure 5A), and these can serve as nucleation points for fractures. By approximating flaws as ellipsoids and calculating the stress field around them, Griffith derived the following fracture criterion (illustrated in figure 5B): A tensile fracture initiates in the plane perpendicular to the maximal principal stress σ_1, if $3\sigma_1 + \sigma_3 > 0$, when

$$\sigma_1 = T_C. \tag{41}$$

If $3\sigma_1 + \sigma_3 < 0$, a shear fracture initiates in the plane at angle

$$\theta = \frac{1}{2}\cos^{-1}\left(\frac{\sigma_1 - \sigma_3}{2(\sigma_1 + \sigma_3)}\right), \tag{42}$$

to the largest principal stress, when

$$(\sigma_1 - \sigma_3)^2 + 8T_C(\sigma_1 + \sigma_3) = 0. \tag{43}$$

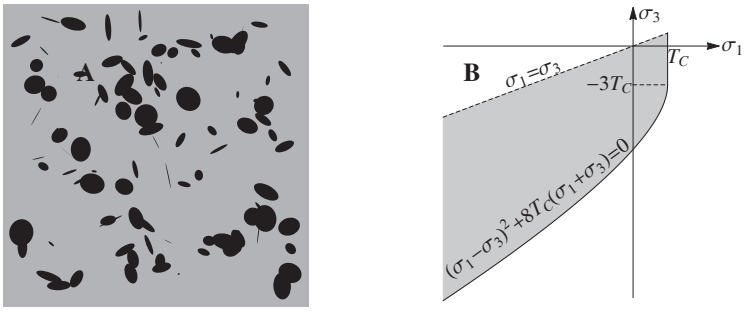

Figure 5: **A:** In Griffith's theory, fractures nucleate from stress concentration around material flaws. **B:** Griffith failure envelope in principal stress space (Failure beyond shaded region).

It can be argued that the Griffith and Mohr-Coulomb criteria lead to essentially the same predictions when applied in rock mechanics [21]. However, the Griffith criterion is founded on a physical basis, and has the advantage that fracture plane directions can be recovered easily from the criterion itself.

3 Fluid migration in porous media

The driving forces promoting fluid transport within a porous host medium, such as a rock, could be manyfold. A fluid may migrate into a solid in response to gradients in pressure or chemical potential, or driven by chemical reactions that consume the fluid. Alternatively, if a solid undergoes compaction or if fluids are being injected or generated by chemical transformations or phase transitions inside the solid, concentration or pressure gradients may build up, providing a driving force for fluid expulsion.

Which transport mechanisms are active in a particular system depends on the strength of the driving forces and the respective properties of the solid and fluid, as well as the thermal and chemical environment. Some of the mechanisms available for fluids to migrate in porous media are discussed below.

3.1 Diffusion

In a porous solid containing a fluid mixture (solvent), an individual fluid component (solute) may migrate through connected pore space by molecular diffusion through the solvent, driven by gradients in chemical potential*. If the concentration of the solute is c, the evolution of the concentration field is governed by the conservation equation

$$\frac{dc}{dt} + \nabla \cdot \vec{J} = \gamma, \tag{44}$$

where $\vec{J}$ is the flux vector, and γ is a source or sink term associated, for example, with production or consumption of the solute by chemical reactions or supply or drainage by an external system. In general, for dilute solutions, the diffusion flux vector may be expressed as

$$\begin{aligned} \vec{J} &= -\frac{Dc}{RT}\nabla\mu(c,P,T) \\ &= -\frac{Dc}{RT}\left(\left(\frac{\partial\mu}{\partial c}\right)_{P,T}\nabla c + \left(\frac{\partial\mu}{\partial P}\right)_{c,T}\nabla P + \left(\frac{\partial\mu}{\partial T}\right)_{c,P}\nabla T\right), \end{aligned} \tag{45}$$

where D is the diffusion coefficient, R is the universal gas constant, T is absolute temperature and $\mu(c,P,T)$ is the chemical potential. Note that the latter depends on the pressure, P, as well as concentration and temperature. Depend-

*In principle, molecular diffusion of a fluid molecule through the solid matrix itself is also possible, however diffusion through solids is typically order of magnitude slower than diffusion through liquids.

ing on the system studied, either pressure, concentration or temperature effects may be dominating or negligible. When pressure and temperature can be ignored, the flux reduces to Fick's first law, which is the most common form of diffusion,

$$\vec{J} = -D\nabla c. \tag{46}$$

However, in the absence of temperature gradients, and with constant concentration, one can also have pressure driven diffusion,

$$\vec{J} = -\frac{vDc}{RT}\nabla P, \tag{47}$$

where $v = (\partial\mu/\partial P)_{c,T}$ is the molar volume of the dissolved species.

Equation 44 is a first order differential equation in time and second order in space, and, as a result, the progression of a diffusion front in space scales as $\sqrt{t}$. Hence, diffusion is most effective over short distances and long time scales, but is ineffective over long distances and short time scales.

3.2 Darcy flow

If the permeability of the solid is sufficiently high, connected pore-space may provide effective pathways for bulk flow of a fluid or mixture of fluids. Pressure-driven slow or viscous flow through porous media is described by Darcy's law, which is based on empirical observations. The Darcy flow velocity, $\vec{U}$, is given by

$$\vec{U} = \frac{k}{\mu}\nabla P. \tag{48}$$

Here, μ is the viscosity of the fluid*, in units of $Pa \cdot s$, and k is the permeability of the porous space, with units of m^2. The oil industry commonly expresses the latter in units of *darcy* (1 *darcy* $\approx 1\mu m^2$). A Darcy mass flux may be defined as

$$\vec{J} = \rho\vec{U}, \tag{49}$$

where ρ is the fluid density.

Advective bulk flow described by Darcy's law scales linearly with time, and, hence, there is a crossover from diffusion dominated transport to advection dominated transport in a system as the length scale increases. However, the efficiency of Darcian flow is also dependent on permeability, k. According to

*The viscosity should not be confused with chemical potential, denoted by the same symbol in Section 3.1

Brace [23], the latter ranges from $10^{-1} - 10^{2}$ *darcy* for sand, $10^{-4} - 10^{0}$ *darcy* for sandstone and $10^{-10} - 10^{-2}$ *darcy* for limestone. If there is no percolating pore space, Darcy flow may not be possible at all over long distances. This may be the case in tight rock, such as shale, where the permeability may be as low as 10^{-11} *darcy*.

3.3 Fracturing as a flow enhancing mechanism

As noted in section 3.2, the efficiency of Darcy flow in a porous solid depends on the porosity and on how the pore space is connected. To a certain extent, fluid pressure may alter the porosity through elastic deformation, as indicated by equation 34b and equation 36b, and this may influence the flow. The porosity can also changed by fracturing, and fractures may provide new effective pathways for fluid flow and contribute to fluid drainage or infiltration. Similarly, the altered transport may in turn affect the progression of fracture.

The potential causes of fracturing are many, but a common cause is volume alterations in the solid [1]. Such volume alterations could result from volume changing chemical reactions between the solid and fluid, or non-uniform thermal expansion or contraction due to heating or cooling. The latter could, for example, occur if an infiltrating fluid is much hotter or colder than the solid host medium. Fracturing could also occur due to swelling of the solid during fluid infiltration or shrinkage associated with fluid withdrawal. Desiccation fractures in mud or gels is an example of the latter [24, 25].

Another mechanism of fracture formation is hydraulic fracturing. Stresses may build up in a solid if fluid pressure rises in the pore space at a higher rate than the system can compensate by fluid flow. The rise in fluid pressure could result via poro-mechanical coupling from compression of the solid, or from internal production of fluids, phase transitions or injection. The latter is exploited industrially to recover oil and gas from shale, and over a million oil and gas wells have already been hydraulically fractured [16]. There are also many examples of hydraulic fracturing occurring naturally. For example, crystals growing form a supersaturated solution or supercooled liquid may exert a so-called force of crystallisation on the pore walls. The force of crystallisation due to formation of salt or ice crystals can reach magnitudes of tens of megapascals, and be a significant cause of damage to building materials [2, 3]. Similarly, gas bubbles growing from a supersaturated pore liquid may induce stresses reaching

hundreds of megapascals [26, 27], sufficient to overcome lithostatic pressure at 10 kilometre depth. Cracks forming by bubble nucleation is a phenomenon observed in mud or gel-like materials [28]. Release of methane by fracturing during degassing of sediments is one example, which could have implications for the Earth's climate [6, 29]. Another example of hydrofracturing in nature is magma emplacements and intrusions in the earths crust, which may heat water or organic matter in rock and cause explosive release of fluids [9]. Release of fluids from hydrous minerals in subduction zones can trigger earthquakes [5]. Another process, where gases cause hydraulic fracturing, is the generation of fission gases in nuclear fuel pellets, which poses a challenge to the nuclear energy industry [13]. Finally, a hypothesis investigated in this thesis, and discussed in more detail in section 4, is that hydrofracturing may be an important mechanism for primary migration of hydrocarbons [10, 11, 12].

4 Primary migration

4.1 Background

Most of the petroleum resources consumed by humanity thus far has come from relatively accessible sources. Typically, reservoirs of accumulated oil and gas are found at shallow depth, in permeable rock such as sandstone or limestone, sealed by less permeable layers of sedimentary rock. These, so-called *conventional* petroleum resources, may be recovered by drilling wells through the cap rock, allowing the over-pressured oil and gas to escape. At some locations, petroleum naturally seeps to the ground, and has been used by people for lighting and medicine for generations.

Although natural gas may be formed at shallow depth by methanogenic microbes, the bulk of oil and gas is formed far from the conventional reservoirs, in organic-rich sedimentary source rock at larger depths. The source rock is typically shale, a sedimentary rock formed by compaction of silt ($0.0004 - 0.063$ μm size) and clay (< 0.0004 μm size). During burial, organic kerogen of high molecular weight in the source rock is thermally decomposed into lower mass and lower density hydrocarbons. The kinetics of this process, referred to as maturation, depends strongly on temperature, which in turn is correlated with burial depth, as illustrated in figure 6. The formation of oil from kerogen takes place at depths of $2 - 5$ km and temperatures of $50 - 150$ °C. Gas is formed at depths of $3 - 6$ km and temperatures of $100 - 250$ °C. At even lower depths hydrocarbon generation is superseded by graphite formation. The time frame for petroleum conversion under natural conditions is typically in the range $1 - 100$ million years.

The migration of hydrocarbons from its point of formation (in the source rock) to its point of accumulation (in the reservoir) may be divided into primary and secondary migration. Primary migration, which is the focus of this thesis, refers to the initial part; the migration within, and expulsion from, the source rock. The mechanisms by which it occurs are discussed in Section 4.3. Secondary migration refers to the later stage; the transport of the expelled hydrocarbon fluids towards the reservoir. The latter process is predominantly buoyancy driven and takes place by bulk flow through a relatively permeable carrier bed.

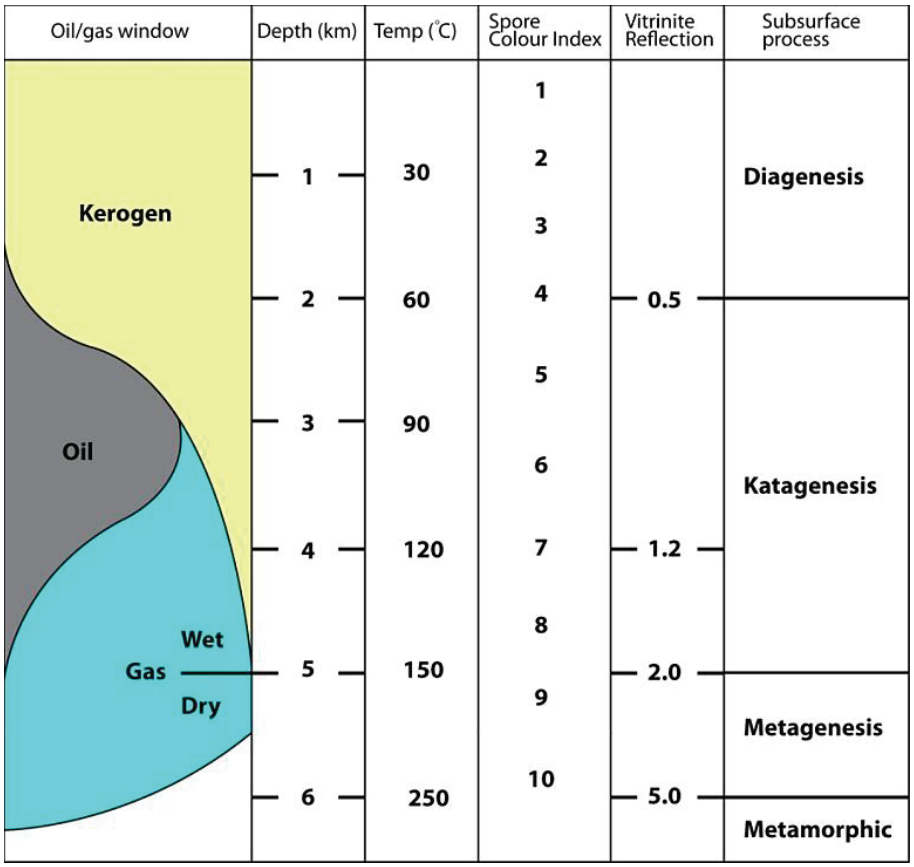

Figure 6: Overview of conversion of kerogen to oil and gas. Source: [10].

4.2 Unconventional oil and gas

Immature source rock may contain significant amounts of kerogen that has not been converted to oil and gas, or may contain oil and gas that has not been expelled. Even in mature source rock, significant amounts of oil and gas will be retained by sorption, and the expulsion from fine-grained shales is counteracted by capillary forces. Over the past decades, increasing energy demands, depletion of conventional reservoirs and the introduction of new technology has made production directly from source rock commercially viable. These petroleum resources are referred to as *unconventional reservoirs*. The geology of unconventional oil and gas is summarised in figure 7. The unconventional reservoirs are typically located at larger depths than conventional reservoirs, often in stratified layers of low permeability shale. These shale formations typically range in thickness from tens to hundreds of meters. For example, in some places, the Green River Shale is over $800\ \mathrm{m}$ thick. The Marcellus and Utica shales are both up to about $270 - 300\ \mathrm{m}$ thick. The Bakken shale is much thinner, up to about $40\ \mathrm{m}$.

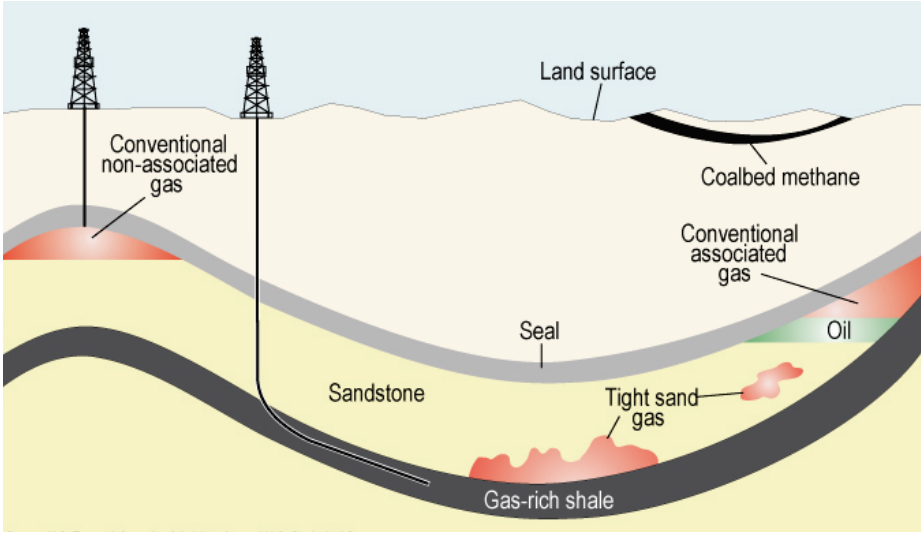

Figure 7: Geology of conventional and unconventional oil and gas resources. (Source: U.S. Energy Information Administration, `http://www.eia.gov/todayinenergy/detail.cfm?id=110`)

Horizontal drilling and hydraulic fracturing are among the technologies that the industry exploit to extract oil and gas from low permeability reservoirs.

A

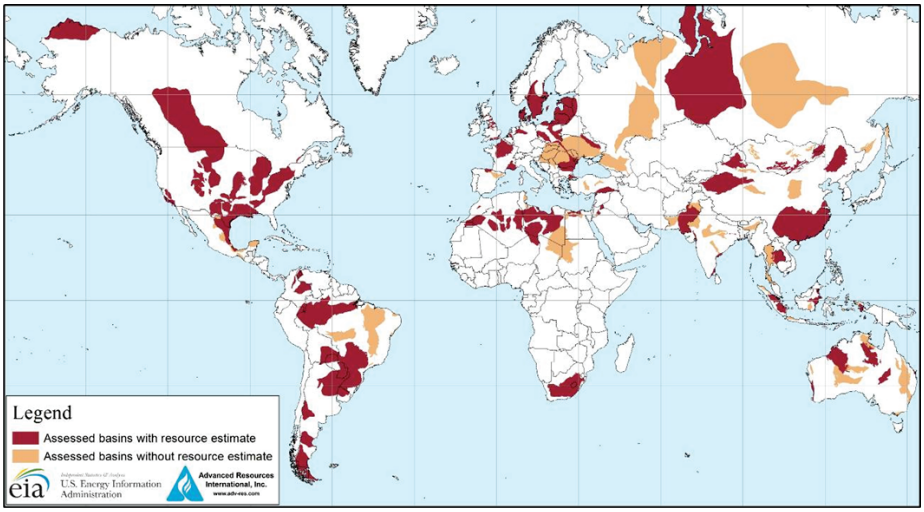

B

Rank	Country	Shale oil (billion barrels)	
1	Russia	75	
2	U.S.[1]	58	(48)
3	China	32	
4	Argentina	27	
5	Libya	26	
6	Australia	18	
7	Venezuela	13	
8	Mexico	13	
9	Pakistan	9	
10	Canada	9	
	World Total	**345**	**(335)**

C

Rank	Country	Shale gas (trillion cubic feet)	
1	China	1,115	
2	Argentina	802	
3	Algeria	707	
4	U.S.[1]	665	(1,161)
5	Canada	573	
6	Mexico	545	
7	Australia	437	
8	South Africa	390	
9	Russia	285	
10	Brazil	245	
	World Total	**7,299**	**(7,795)**

Figure 8: **A:** Overview of worldwide basins with assed formations of shale oil/gas. **B:** Top ten countries in terms of technically recoverable shale oil resources. **C:** Top ten countries in terms of technically recoverable shale gas resources. (Source: U.S. Energy Information Administration, `http://www.eia.gov/todayinenergy/detail.cfm?id=11611`)

To date, more than a million oil and gas wells have been hydraulically fractured [16]. Artificial heating is another method to induce hydrocarbon generation and fracturing off immature shale.

The boom in shale gas and oil comes with vast geopolitical consequences. For example, North America (the United States and Canada) are close to becoming energy independent, for the first time in decades. In 2005 the US petroleum production was 69% of consumption, but in 2012 this number had risen to 84%, and it is projected to reach 101% by 2035 [30]. Figure 8A shows a map of the basins around the world where prospects for oil and gas recovery have been assessed. Figures 8B-C show the top 10 countries, ranked according to the known unconventional reservoirs of oil and gas, respectively.

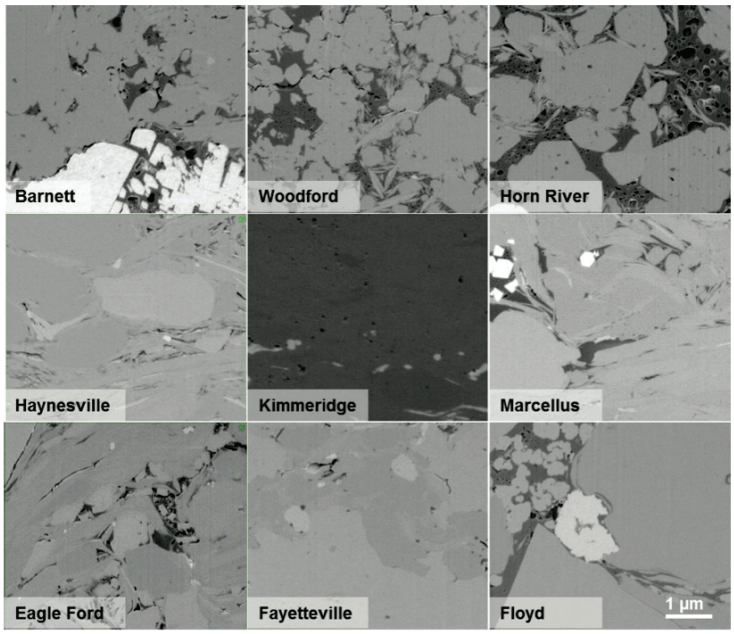

Figure 9: Scanning electron microscope (SEM) images of samples from different shale formations, with varying TOC. (Source: [31])

Various measures are used to asses the commercial potential of unconventional reservoirs. One parameter is the total organic carbon content (TOC), i.e. the total amount of kerogen as percent of the mass. Figure 9 show scanning electron microscope images of shale samples with varying TOC from various basins. Another assessment quantity is the thermal maturity of the rock, which measures the extent of organic metamorphism. It may be used to infer the maxi-

mum temperature that the rock has been subjected to. Methods used to quantify the maturity include measuring the reflectance of certain minerals, such as vitrinite, or the colour of spores and pollen, which are sensitive to temperature. The correlation of reflectivity and spore colour index to depth and temperature is indicated in figure 6. Other quantities that may be measured to evaluate commercial prospect are the reservoir porosity and the fraction of adsorbed and free gas, as well as the physical dimensions (thickness and extent) of a shale formation.

4.3 Mechanisms of primary migration

How primary migration occurs is still poorly understood. To observe it in action, in geological settings at depth, is not possible, as the process is too slow to observe. What is certain, however, is that the process involves vastly different length scales, from the thermal decomposition of kerogen on the nanometer scale, to kerogen networks on the $100\ \mu\mathrm{m}$ scale and reservoirs on the $\gg 1\ \mathrm{m}$ scale. This is illustrated well by Stainforth and Reinders [32] in figure 10.

The ratio of oil and gas to kerogen is a factor that determines whether migration can occur by bulk flow or is restricted to molecular diffusion. For low concentrations, the oil and gas may be fully dissolved in the kerogen, and, hence, diffusion is the only available mechanism. On the other hand, even if oil and gas exist in bulk form, bulk flow may not be possible, because the permeability of shale is very low (~ 0.01 nanodarcy) and the pore size is so small that capillary forces become a significant hindrance of flow (pore size is typically 100Å).

Various diffusion mechanisms for primary migrateion have been proposed. One of these is diffusion of dissolved oil and gas through aqueous pore space [33]. In this scenario, the dissolved hydrocarbons may also be transported by bulk flow of pore water, driven, for example, by compaction. Thomas and Clouse investigate primary migration by diffusion of dissolved hydrocarbons inside connected kerogen networks permeating the source rock [34, 35, 36]. In experiments, they measure the flux of bitumen through chalk samples coated with fatty acids, and report that the flux was hundredfold compared to uncoated, water filled samples. This shows that, in principle, diffusion through kerogen networks is a more effective transport mechanism than diffusion through water [34]. However, in experiments with real shale samples, the kerogen was only observed to enhance flux for high TOC values ($< 2.2\%$) [35]. In geologi-

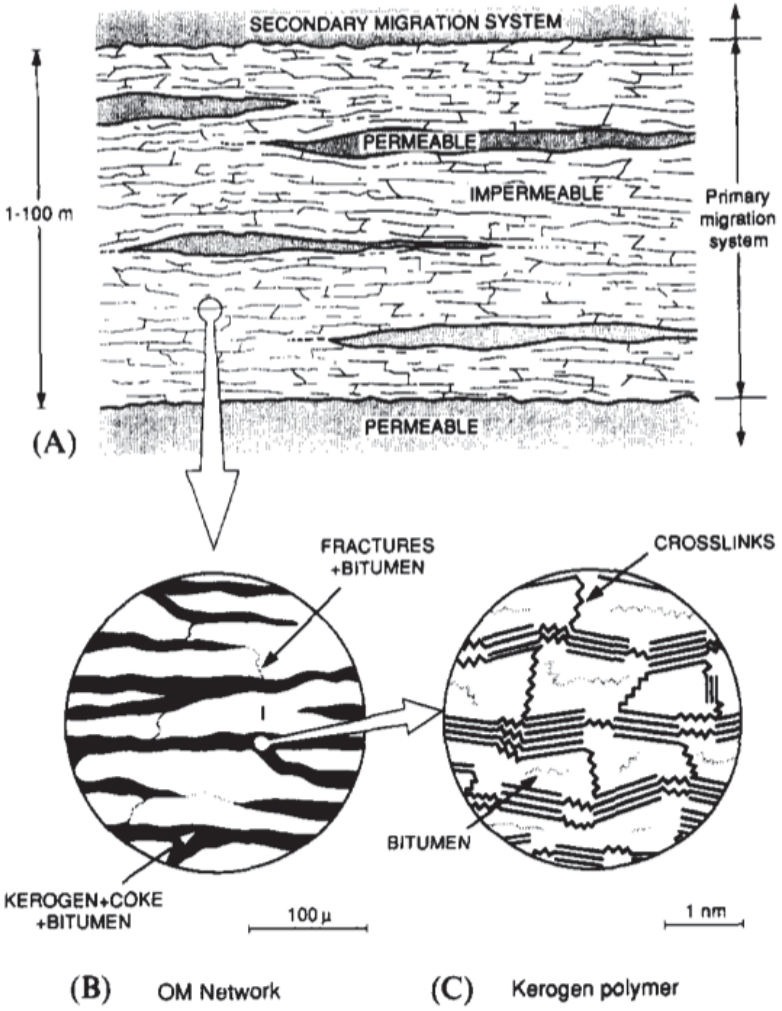

Figure 10: The length scales involved in the primary migration process. **A:** Macroscopic. **B:** Microscopic. **C:** Molecular. (Source: [32])

cal settings, they argue that diffusion is pressure driven (obeying Eq. 47), rather than concentration driven (Eq. 46) and show that realistic fluxes only suffice for filling small to intermediate size reservoirs [36].

A range of other primary migration mechanisms have been suggested, including migration of micro droplets, migration of micelles [37] and migration of oil dissolved in methane [38]. These, and the other mechanisms mentioned above, may all contribute to primary migration to various extents, depending on factors such as the state of maturation, the kerogen content and thermodynamic conditions.

Fractures may provide effective low capillarity pathways for fluid flow, and have been hypothesised to play an important role in primary migration [10, 11]. This theory is supported by an increasing body of evidence. Micro-fractures are found abundantly in mature source rock [39, 40], illustrated in figure 11 (These observations may even be under-representative, as micro-fractures are expected to heal rapidly under prevailing conditions in source rock.). The same is found in experiments involving thermal decomposition of kerogen during heating of shale samples [41, 42], illustrated in figure 12. Despite this evidence most ex-

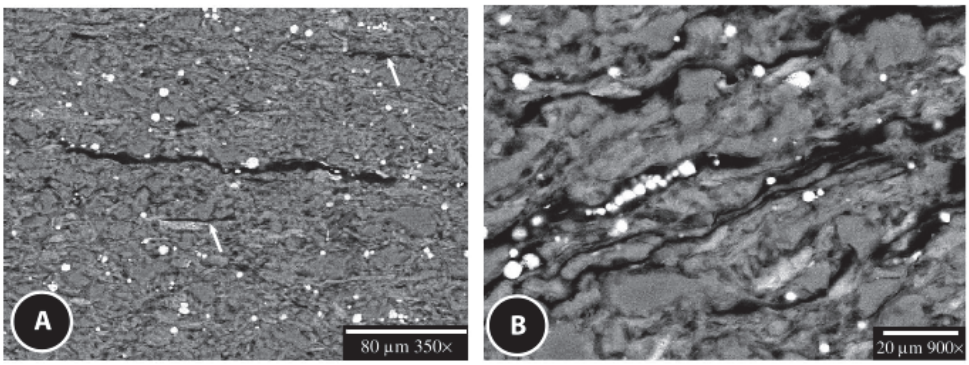

Figure 11: Scanning electron microscope (SEM) images Dunkirk shale. **A:** Sample showing an isolated large microcrack and two small ones (arrows). **B:** Sample showing a network of closely spaced microcracks (Source: [40])

perimental and modelling studies have ignored the effect of fractures [43, 44]. However, a few exceptions exist. Some modelling studies do include fracture effects, [45, 46, 47], but are based on simplified, idealised fracture geometries that are of limited relevance. Bons and Milligen [12] show experimentally

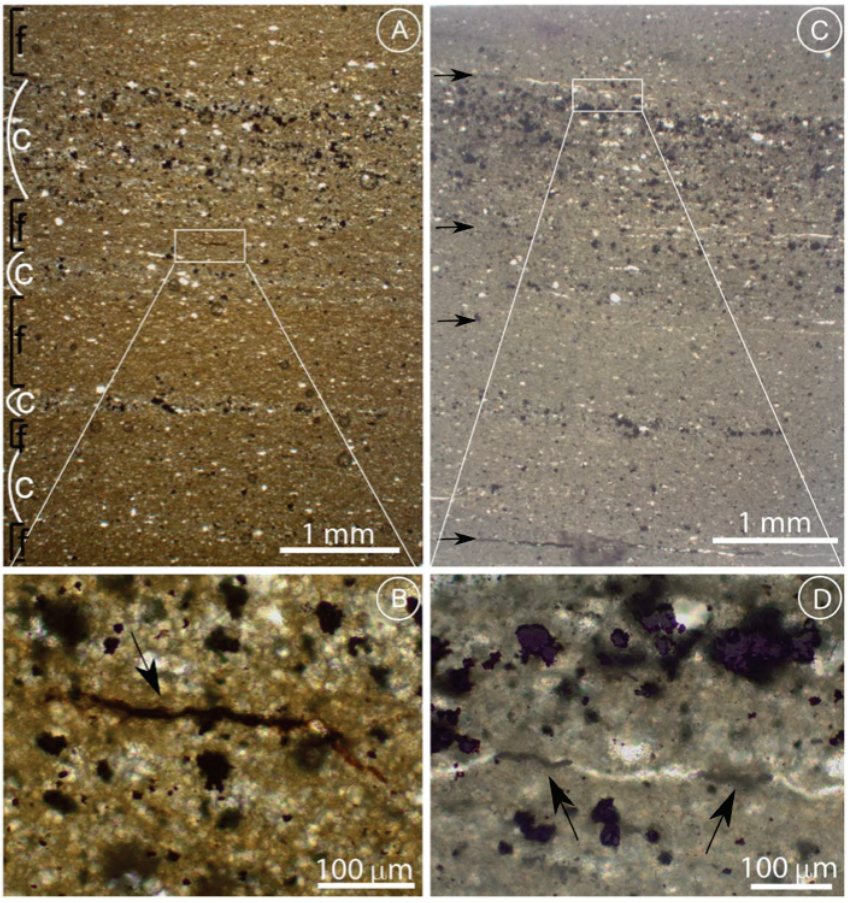

Figure 12: Thin section images of Green river shale from heating experiment. **A:** Sample before heating. (f) indicates clay-rich layers with high kerogen content, and (c) indicates coarser layers with siliciclastic grains. **B:** Enlarged view of kerogen lens from A. **C:** The same sample as in A, after heating, with arrows indicating cracks formed during heating, mainly located in the kerogen rich layers. **D:** The kerogen in B, after heating, with arrows indicating organic remains. (Source: [41])

that fracturing is activated as a transport mechanism when Darcian flow fail to accommodate sufficient transport, and speculate that it may be important for hydrocarbon migration.

Even if micro fractures may play a role for large scale migration, it is likely that diffusion plays an important role on short length scales, within solid kerogen and into fractures. Hence, when evaluating the potential importance of fractures as drainage pathways in primary migration, it is important to understand how fracturing is coupled to fluid supply and transport by other mechanisms.

4.4 Gelatine model of primary migration

In the first and last articles of this thesis, an analogue model of primary migration was investigated. The model consist of a layer of gelatine confined between two glass plates, in a so-called Hele-Shaw cell. Before filling the cell, the gelatine is mixed with sugar and yeast. Next, it is left horizontally in a fridge overnight to set. When brought back to room temperature, a fermentation process is initiated, where the yeast consumes sugar to produce CO_2. The CO_2 is dissolved in the water of the gel, but as the water becomes supersaturated, bubbles may form. It is observed that these bubbles develop into fractures, providing pathways for the CO_2 gas to drain at the external boundaries of the Hele-Shaw cell. The experimental setup is shown in figure 13, and a time sequence of an evolving fracture network is displayed in figure 14.

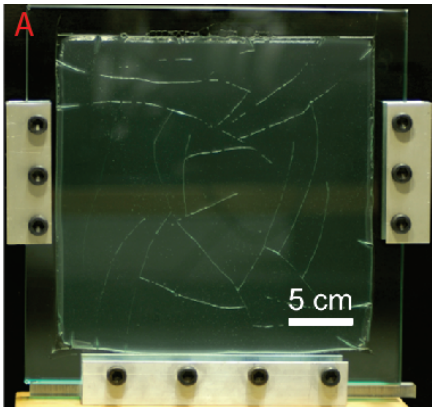

Figure 13: Setup of gelatine experiment. A layer of gelatine of dimensions $30\ \mathrm{cm} \times 30\ \mathrm{cm} \times 2\ \mathrm{mm}$ is confined in a Hele-Shaw cell.

Figure 14: Time development of fracture network in gelatine experiment.

The advantage of the model is that gelatine is transparent, facilitating imaging throughout the fracturing process. Additionally, the gel is birefringent, allowing strain fields to be observed by means of crossed polarisers (figure 15). Importantly, the system also shares several features of tight rock. Firstly, on the experimental time scale, the diffusion of CO_2 in the gelatine is slow, and only effective over short distances. Secondly, the rheomechanical properties of gelatine makes it a suitable rock analog [48]. Thirdly, the confinement of the glass plates suppress and localise elastic interactions. In real source rock, elastic interactions are localised to a certain extent because elastic interactions in three dimensions decay as the inverse of separation, and long range interactions may be shielded by the fracture network.

Given its simplicity, but at the same time complex behaviour, these gelatine experiments are used as a point of departure for the modelling approaches proposed in this thesis. It is believed that the insights gained from studying these experiments may be relevant to primary migration of hydrocarbons in tight source rock, and that the modelling approaches may later be extended to model real geological systems.

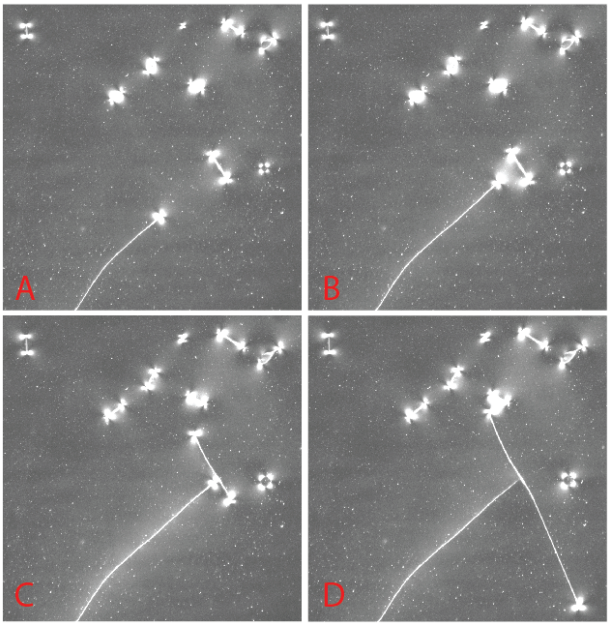

Figure 15: Time evolution of the strain field around a set of evolving fractures. The strain field is visualised using cross-polarisers. Note the concentration of strain at the fracture tips.

5 Scope and overview of scientific papers

As the previous section describes, primary migration is a complex problem, which involves a long list of processes. To address the full problem, one would need to consider the kinetics of kerogen decomposition, the coexistence of multiple fluids and phases in the pore space, the bulk flow of these components and diffusion of individual fluid components, the coupling of fluid pressure to mechanical deformation, as well as the nucleation of fractures and how these propagate. All these aspects depend on thermodynamic conditions, homogeneities in material properties and the distribution of porosity and organic matter. All of this, in turn, is associated with uncertainties. Furthermore, different effects take place at different length and timescales.

In this thesis, the choice was made to focus on a few aspects, namely fracturing and the coupling to transport in the generated fracture network. To this end, a simplified experimental model of primary migration was used (as described in section 4.4), and numerical models were constructed. By removing certain aspects from the complex primary migration problem, these models provide more controlled environments to investigate the influence of individual factors in isolation.

The remainder of this thesis consists of a collection of six scientific papers. The first and last papers describe a fracturing process in an experimental model for primary migration in a simplified two-dimensional setting, whereas the remaining four articles use numerical models to address various aspect of this complex process. An overview of each paper is provided below, including an account of my contributions to the work. A brief summary of the papers is also provided in table 1 (at the end of this section).

Paper I: Drainage fracture networks in elastic solids with internal fluid generation

This paper describes analog quasi two-dimensional experiments used to simulate primary migration. The system consists of a layer of gelatine, containing yeast and sugar, confined between two glass plates in a Hele-Shaw cell. The yeast consumes the sugar and produce CO_2 which is dissolved in the gelatine. Bubbles form as the saturation of dissolved CO_2 increases, and as gas pressure rises, these bubbles may develop into fractures which evolve to form a network through which gas may drain out of the system via the external boundaries.

This paper focus on characterising the final fracture network, which is found to be topologically intermediate between a tree (typical of drainage networks, such as river systems) and a polygonal/hierarchical network (typical of fracture networks). A simple model is proposed to generate such intermediate fracture networks and used to quantify the experimental fracture patterns.

I was involved in this paper as a co-author, and my main contribution was the development of a theory to explain the fracturing mechanism and construction of the simple model which was used to compare with experiments. I also wrote parts of the discussion and conclusion section, and participated in the editing of the paper.

Paper II: Classification of fracture patterns by heterogeneity and topology

The fracture patterns described in paper I were found to be intermediate between trees and polygonal/hierarchical networks, reflecting both the transport and fracturing nature of the process. In these experiments we also observed that fractures nucleate far from existing fractures, due to the concentration field, which controlled the fracture nucleation. Motivated by these observations, a simple two-parameter model was constructed which can generate fracture patters with varying topology and heterogeneity (whether fractures cluster together or nucleate far from each other).

A scheme is described to map real fracture networks onto the model, and allows fracture patterns to be quantified in terms of the two model parameters describing topology and heterogeneity respectively. The scheme is applied to three examples, including one fracture pattern from the gelatine experiments described in paper I.

I developed this model, following a suggestion by one of the coauthors, Paul Meakin. I implemented the model with some help from one of the other coauthors, Espen Jettestuen. I conducted the analysis included in the paper and was the main contributor to the writing of the text.

Paper III

After observing the evolution of the experimental fracture patterns described in paper I, I came up with a simplified model for the fracture network evolution, where fractures are represented by line segments which propagate at constant speed in both directions until they meet other fractures. During my participa-

tion at the Wolfram Science Summer School 2013, I discussed this idea with Dr Stephen Wolfram, and together we formulated a more general network evolution model, which is not restricted to modelling fracturing processes. This model, termed Contact Arrested Propagation (CAP), may be formulated on arbitrary networks, and on lattices in two and three dimension in particular. In this paper we investigate this abstract model and show that it has certain universal features. The model may be useful for generating artificial fracture networks and for studying certain fracturing and fragmentation processes. A major advantage of the model is that it may be easily coupled to any other model that can be formulated on a network or lattice, and the implementation is completely independent of the underlying network or lattice being used.

The implementation of the model and the analysis presented in the paper was conducted by me. I was also the main contributor in the writing of the text.

Paper IV

This paper uses the CAP model proposed in paper III to model fracturing on square and cubic lattices, coupled to fluid generation and transport. The model setup closely resembles the experiments described in paper I, where elastic interaction between fractures is limited due to the attachment of the gelatine to the glass plates. We demonstrate how fractures compete for fluid and may interact via the fluid concentration field. This form of interaction may be dominant in many systems, including primary migration systems. Since the model only involves a scalar field it may be scaled up to large systems of interacting fractures in three dimensions at relatively low computational cost compared to models that treat mechanical interactions explicitly.

I conducted the bulk part of the coding, analysis and writing of this paper.

Paper V

In this paper, a new discrete element model (DEM) is described, where an elastic material is represented as a network of nodes connected by springs. The new model, which is particularly suitable for modelling coupled processes where fracturing is driven by fluid pressure in fractures, differs from previous DEM models in the way that fracturing is implemented: rather than breaking/removing springs, fracturing is implemented by splitting nodes and reconnecting the spring network. The model allows fractures to be represented in a

realistic manner and with less lattice artefacts than in previous DEM models. Importantly, fracture volumes and surfaces may be explicitly represented, facilitating the coupling to fluid transport and mechanical interaction between the fluid and solid.

The original idea for this new model came out of a discussion between myself and one of the coauthors, Espen Jettestuen. I implemented/coded the model and was in charge of the analysis and writing of the paper.

Paper VI

This paper describes the same experiments as paper I. Here the focus is on the time evolution of the fracture network and the intermittent dynamics of fluid expulsion as fractures open and close. The power spectrum of the fracture area variation is investigated and the correlations are quantified.

I was involved as a co-author in this paper, and have contributed to the planning of experiments, discussions around the quantities to be measured and the interpretation of results. I have also been involved in the editing of the paper.

Paper	Model type	Description	Status
1	Experiment (quasi-static)	Description/quantification of the fracture networks produced in quasi two-dimensional gelatine experiments to simulate primary migration.	Published
2	Model (quasi-static)	A model for generating and classifying fracture patterns that are topologically intermediate between drainage networks (trees) and fracture networks (polygonal/hierarchical).	Published
3	Model (dynamic)	A new model termed Contact Arrested Propagation (CAP), which may be used to generate fracture networks in two or three dimensions or to simulate certain fracturing processes.	Published
4	Model (dynamic)	Extension of the CAP model to incorporate fluid transport and fluid pressure in fractures. The system is investigated in two and three dimensions.	In revision
5	Model (dynamic)	A new discrete element model for modelling elastic deformation and fracturing in response to internal fluid generation and pressure accumulation.	Published
6	Experiment (dynamic)	Investigation of the evolution and opening and closing dynamics of fractures in quasi two-dimensional gelatine experiments to simulate primary migration.	In press

Table 1: Short summary of enclosed papers.

Bibliography

[1] Y. Cohen, J. Mathiesen, and I. Procaccia. Drying patterns: Sensitivity to residual stresses. *Physical Review E*, 79(4):046109, 2009.

[2] J. Walder and B. Hallet. A theoretical model of the fracture of rock during freezing. *Geological Society of America Bulletin*, 96(3):336–346, 1985.

[3] G. W. Scherer. Crystallization in pores. *Cement and Concrete Research*, 29(8):1347–1358, 1999.

[4] B. Jamtveit and H. Austrheim. Metamorphism: the role of fluids. *Elements*, 6(3):153–158, 2010.

[5] J. H. Davies. The role of hydraulic fractures and intermediate-depth earthquakes in generating subduction-zone magmatism. *Nature*, 398(6723):142–145, 1999.

[6] R. D. McIver. Role of naturally occurring gas hydrates in sediment transport. *AAPG Bulletin*, 66(6):789–792, 1982.

[7] A. Mazzini, H. Svensen, G. G. Akhmanov, G. Aloisi, S. Planke, A. Malthe-Sørenssen, and B. Istadi. Triggering and dynamic evolution of the LUSI mud volcano, Indonesia. *Earth and Planetary Science Letters*, 261(3):375–388, 2007.

[8] H. Svensen, S. Planke, A. Malthe-Sørenssen, B. Jamtveit, R. Myklebust, T. R. Eidem, and S. S. Rey. Release of methane from a volcanic basin as a mechanism for initial Eocene global warming. *Nature*, 429(6991):542–545, 2004.

[9] H. Svensen, S. Planke, L. Chevallier, A. Malthe-Sørenssen, F. Corfu, and B. Jamtveit. Hydrothermal venting of greenhouse gases triggering Early Jurassic global warming. *Earth and Planetary Science Letters*, 256(3):554–566, 2007.

[10] B. P. Tissot and D. H. Welte. Petroleum formation and occurrence: a new approach to oil and gas exploration. 1978.

[11] R. R. Berg and A. F. Gangi. Primary migration by oil-generation microfracturing in low-permeability source rocks: Application to the Austin Chalk, Texas. *AAPG Bulletin-American Association of Petroleum Geologists*, 83(5):727–756, 1999.

[12] P. D. Bons and Boudewijn P. van Milligen. New experiment to model self-organized critical transport and accumulation of melt and hydrocarbons from their source rocks. *Geology*, 29(10):919–922, 2001.

[13] T. R. G. Kutty, K. N. Chandrasekharan, J. P. Panakkal, and J. K. Ghosh. Fracture toughness and fracture surface energy of sintered uranium dioxide fuel pellets. *Journal of materials science letters*, 6(3):260–262, 1987.

[14] L. Chiaramonte, M. D. Zoback, J. Friedmann, and V. Stamp. Seal integrity and feasibility of CO2 sequestration in the teapot dome EOR pilot: geomechanical site characterization. *Environmental Geology*, 54(8):1667–1675, 2008.

[15] The future of natural gas. Massachusetts Institute of Technology Energy Initiative, http://mitei.mit.edu/publications/reports-studies/future-natural-gas, 2011.

[16] Hydraulic fracturing. Association of American State Geologists, http://www.stategeologists.org/fact_sheet.php, 2012.

[17] L. D. Landau, E. M. Lifshitz, J. B. Sykes, W. H. Reid, and E. H. Dill. Theory of elasticity: Vol. 7 of course of theoretical physics. *Physics Today*, 13:44, 1960.

[18] O. Coussy. *Poromechanics*. Chichester: Wiley, 2004.

[19] T. L. Anderson. *Fracture mechanics: fundamentals and applications*. CRC press, 2005.

[20] D. D. Pollard and R. C. Fletcher. *Fundamentals of structural geology*. Cambridge University Press, 2005.

[21] D. P. Clausing. Comparison of Griffith's theory with Mohr's failure criteria. In *The 3rd US Symposium on Rock Mechanics (USRMS)*, 1959.

[22] A. A. Griffith. The phenomena of rupture and flow in solids. *Philosophical transactions of the royal society of London. Series A, containing papers of a mathematical or physical character*, 221:163–198, 1921.

[23] W. F. Brace. Permeability of crystalline and argillaceous rocks. In *International Journal of Rock Mechanics and Mining Sciences & Geomechanics Abstracts*, volume 17, pages 241–251. Elsevier, 1980.

[24] S. Bohn, L. Pauchard, and Y. Couder. Hierarchical crack pattern as formed by successive domain divisions. I. temporal and geometrical hierarchy. *Physical Review E*, 71(4), 2005.

[25] S. Bohn, J. Platkiewicz, B. Andreotti, M. Adda-Bedia, and Y. Couder. Hierarchical crack pattern as formed by successive domain divisions. II. from disordered to deterministic behavior. *Physical Review E*, 71(4), 2005.

[26] M. Mangan and T. Sisson. Delayed, disequilibrium degassing in rhyolite magma: decompression experiments and implications for explosive volcanism. *Earth and Planetary Science Letters*, 183(3):441–455, 2000.

[27] M. T. Mangan, T. W. Sisson, and W. B. Hankins. Decompression experiments identify kinetic controls on explosive silicic eruptions. *Geophysical research letters*, 31(8), 2004.

[28] B. P. Boudreau, C. Algar, B. D. Johnson, I. Croudace, A. Reed, Y. Furukawa, K. M. Dorgan, P. A. Jumars, A. S. Grader, and B. S. Gardiner. Bubble growth and rise in soft sediments. *Geology*, 33(6):517–520, 2005.

[29] G. Etiope and R. W. Klusman. Geologic emissions of methane to the atmosphere. *Chemosphere*, 49(8):777–789, 2002.

[30] British Petroleum. BP energy outlook 2035, 2014.

[31] M. E. Curtis, R. J. Ambrose, C. H. Sondergeld, and C. S. Rai. Structural characterization of gas shales on the micro- and nano-scales. Canadian Unconventional Resources and International Petroleum Conference, 19-21 October 2010, Calgary, Alberta, Canada.

[32] J. G. Stainforth and J. E. A. Reinders. Primary migration of hydrocarbons by diffusion through organic matter networks, and its effect on oil and gas generation. *Organic Geochemistry*, 16(1):61–74, 1990.

[33] E. E. Bray and W. R. Foster. Process for primary migration of petroleum. *Am. Assoc. Pet. Geol. Bull.;(United States)*, 64(1), 1980.

[34] M. M. Thomas and J. A. Clouse. Primary migration by diffusion through kerogen: I. model experiments with organic-coated rocks. *Geochimica et Cosmochimica Acta*, 54(10):2775–2779, 1990.

[35] M. M. Thomas and J. A. Clouse. Primary migration by diffusion through kerogen: II. hydrocarbon diffusivities in kerogen. *Geochimica et Cosmochimica Acta*, 54(10):2781–2792, 1990.

[36] M. M. Thomas and J. A. Clouse. Primary migration by diffusion through kerogen: III. calculation of geologic fluxes. *Geochimica et Cosmochimica Acta*, 54(10):2793–2797, 1990.

[37] R. J. Cordell. Depths of oil origin and primary migration; a review and critique. *AAPG Bulletin*, 56(10):2029–2067, 1972.

[38] L. C. Price, L. M. Wenger, T. Ging, and C. W. Blount. Solubility of crude oil in methane as a function of pressure and temperature. *Organic Geochemistry*, 4(3):201–221, 1983.

[39] J. Chanchani, R. R. Berg, and C.-I. Lee. Pressure solution and microfracturing in primary oil migration, upper cretaceous Austin Chalk, Texas Gulf Coast. *AAPG Bulletin*, 80(CONF-9610180), 1996.

[40] G. G. Lash and T. Engelder. An analysis of horizontal microcracking during catagenesis: Example from the catskill delta complex. *AAPG bulletin*, 89(11):1433–1449, 2005.

[41] M. Kobchenko, H. Panahi, F. Renard, D. K. Dysthe, A. Malthe-Sørenssen, A. Mazzini, J. Scheibert, B. Jamtveit, and P. Meakin. 4D imaging of fracturing in organic-rich shales during heating. *Journal of Geophysical Research: Solid Earth (1978–2012)*, 116(B12), 2011.

[42] H. Panahi, P. Meakin, F. Renard, M. Kobchenko, J. Scheibert, A. Mazzini, B. Jamtveit, A. Malthe-Sorenssen, and D. K. Dysthe. A 4D synchrotron x-ray-tomography study of the formation of hydrocarbon-migration pathways in heated organic-rich shale. *SPE Journal*, 18(2):366–377, 2013.

[43] E. Lafargue, J. Espitalie, T. Jacobsen, and S. Eggen. Experimental simulation of hydrocarbon expulsion. *Organic Geochemistry*, 16(1):121–131, 1990.

[44] J. L. Rudkiewicz, O. Brévart, J. Connan, and F. M. Montel. Primary migration behaviour of hydrocarbons: from laboratory experiments to geological situations through fluid flow models. *Organic geochemistry*, 22(3):631–IN8, 1994.

[45] Z.-H. Jin and S. E. Johnson. Primary oil migration through buoyancy-driven multiple fracture propagation: Oil velocity and flux. *Geophysical Research Letters*, 35(9), 2008.

[46] Z.-H. Jin, Scott E. Johnson, and Z. Q. Fan. Subcritical propagation and coalescence of oil-filled cracks: Getting the oil out of low-permeability source rocks. *Geophysical Research Letters*, 37(1):L01305, 2010.

[47] Z. Q. Fan, Z.-H. Jin, and S. E. Johnson. Subcritical propagation of an oil-filled penny-shaped crack during kerogen–oil conversion. *Geophysical Journal International*, 182(3):1141–1147, 2010.

[48] E. Di Giuseppe, F. Funiciello, F. Corbi, G. Ranalli, and G. Mojoli. Gelatins as rock analogs: A systematic study of their rheological and physical properties. *Tectonophysics*, 473(3):391–403, 2009.

Scientific papers

Paper I:

Drainage fracture networks in elastic solids with internal fluid generation

M. Kobchenko, A. Hafver, E. Jettestuen, O. Galland, F. Renard, P. Meakin, B. Jamtveit and D.K. Dysthe

Published in EPL (Europhysics Letters), Vol. **102**(6), 2013, pp. 66002
doi:10.1209/0295-5075/102/66002

epl A Letters Journal Exploring the Frontiers of Physics

June 2013

EPL, **102** (2013) 66002 www.epljournal.org
doi: 10.1209/0295-5075/102/66002

Drainage fracture networks in elastic solids with internal fluid generation

Maya Kobchenko[1], Andreas Hafver[1], Espen Jettestuen[1,2], Olivier Galland[1], François Renard[1,3], Paul Meakin[1,4], Bjørn Jamtveit[1] and Dag K. Dysthe[1]

[1] *Physics of Geological Processes, University of Oslo - Oslo, Norway*
[2] *International Research Institute of Stavanger - Stavanger, Norway*
[3] *Univ. Grenoble 1, ISTerre - BP 53, F-38041 Grenoble, France, EU*
[4] *Temple University, Department of Physics - Barton Hall, Philadelphia, PA 19122-6082, USA*

received 17 May 2013; accepted 12 June 2013
published online 26 June 2013

PACS 64.60.aq – Networks
PACS 47.54.-r – Pattern selection; pattern formation
PACS 64.60.av – Cracks, sandpiles, avalanches, and earthquakes

Abstract – Experiments in which CO_2 gas was generated by the yeast fermentation of sugar in an elastic layer of gelatine gel confined between two glass plates are described and analyzed theoretically. The CO_2 gas pressure causes the gel layer to fracture. The gas produced is drained on short length scales by diffusion and on long length scales by flow in a fracture network, which has topological properties that are intermediate between river networks and hierarchical-fracture networks. A simple model for the experimental system with two parameters that characterize the disorder and the intermediate (river-fracture) topology of the network was developed and the results of the model were compared with the experimental results.

Introduction. – The formation of many branched, hierarchical networks such as rivers, blood vessels, leaf veins, lightning, etc. are the responses of physical systems to the transport of fluids, substances dissolved in fluids or charge. Such directed tree networks are efficient transport systems and they have characteristic statistical properties [1–4]. It has been postulated that river networks and the landscapes associated with them minimize hydrodynamic energy dissipation [3]. The evolution of river networks is controlled primarily by erosion, an interaction between flowing water and the landscape that does not extend beyond the local drainage basin [4].

Fracture networks are localized strain responses to stress beyond the elastic limits of solids and the fracture network characteristics can reveal the nature of the elastic loading, be it external shear, compression or tension, or generated by material shrinkage [5–7] or by overpressured fluids inside the solid [8]. Even if the fluid pressure in fractures is increased only locally, the elastic interactions are *long ranged* and local pressure increases may have long-range effects such as triggering earthquakes [9,10]. While the statistical topology of river networks has been investigated for almost 70 years [11], the statistical description of fractures [12] has only recently been extended to fracture network topologies [13].

Hydraulic fracturing, used by the petroleum industry to enhance the permeability of reservoir rocks, is induced by injecting a fluid at high pressure into the rock via a cased, cemented and perforated well. In some geological processes large fluid pressures are generated pervasively inside very large rock volumes and the fluid is expelled and transported out of the system. For example, in subduction zones hydrous minerals are subject to increasing pressure and temperature until they are no longer thermodynamically stable and form anhydrous minerals and hydrous fluids with a smaller solid volume but larger total (solid plus fluid) volume [9]. Magmas are formed by partial melting of the Earth's mantle, the melt segregates and moves through the crust to form volcanic intrusions, oceanic crust and volcanoes [14]. As they are progressively burried, organic rich shales are heated and the organic material is thermally decomposed into low-molecular-mass hydrocarbons with lower densities and viscosities. The transport of these lighter hydrocarbons through the virtually impermeable

shale to adjacent high-permeability rock layers is called primary migration and if the shale layer is thick the hydrocarbon drainage must occur via fractures generated in the shale [15].

Although the generation and drainage of fluids in subduction zones, magmas and organic rich shales have each been extensively investigated, the focus of these investigations has been on physical, chemical and geological details rather than generic phenomena. In all of these systems, the solid is under confining stress, a fluid is generated internally in the solid and above some length scale, the fluid migrates through fractures generated in the solid. Here, a set of experiments, a simple theory and an algorithmic model for a system with these characteristics are presented. This system demonstrates the evolution of a new class of networks, drainage fracture networks that are intermediate between river networks and hierarchical-fracture networks. River-like drainage networks with loops has been mentioned as topologically possible, but less efficient, network in studies of transport efficiency [1]. Here we explore the physical reasons why they exist in our experiments and possibly in Nature.

Experimental set-up. – The experimental set-up consists of a Hele-Shaw cell with a gel containing water, gelatin, sugar and yeast. When the yeast consumes the sugar it produces CO_2 and CO_2 bubbles nucleate and evolve into gas-filled fractures. The gas is transported along these cracks to the edges of the gel layer. The Hele-Shaw cell consists of two $300 \times 300 \times 10\,\mathrm{mm}$ glass plates clamped together and separated by 3 mm.

The Hele-Shaw cell was filled with liquid gelatine solution after cleaning the inner surfaces with detergent and distilled water to ensure good adhesion between gelatine and glass. A gelatin solution was prepared by dissolving 58 g of gelatine sheets (from Gelita) in $1\,\mathrm{dm}^3$ of boiling water (100°C). 7.5 g of sugar was dissolved in the gelatine solution, which was then cooled to 30 °C, mixed with 2.5 g of baking yeast and stirred well to homogenize it. Half of the liquid solution was poured into an area of $L \times L, L = 250\,\mathrm{mm}$ of the Hele-Shaw cell and the other half was poured into a bottle connected to a gas volume meter. Both solutions were kept in a refrigerator at 6 °C for 10 hours to obtain a solid, homogeneous gel. It is assumed that the yeast particles are homogeneously distributed on large scales and variations in the particle size and local number density (and gas production rate) are treated as quenched disorder.

Four experiments were conducted under similar conditions at room temperature (17 ± 1 °C), where the gelatine is a transparent, brittle, nearly elastic solid [16]. Two experiments (Exp_1, Exp_2; see supplementary movie `gel_fracture_EPL.wmv`) were performed with the same concentration of yeast and sugar (as described above). In the other two experiments (Exp_3, Exp_4) half and double the amounts of yeast and sugar were used. At 17 °C, yeast is activated, consumes sugar and produces CO_2 gas.

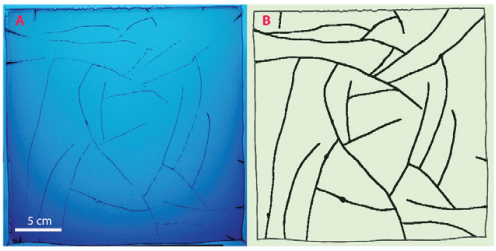

Fig. 1: Original and processed optical images of Exp_1. A: original image of fracture pattern at time $t = 22\,\mathrm{h}$. B: processed binary image used for further analysis of network topology and geometry. The boundary of the gelatine layer is not confined and it is the drainage perimeter.

Fracture nucleation and propagation was imaged every minute at a resolution of 9 pixels/mm. Measurements of the bubble sizes and fracture apertures have an estimated accuracy of ± 0.1 mm. Digital image correlation analysis showed that the motion of the camera was $\leqslant 1$ pixel length.

Results. – After ≈ 2 hours fracture nucleation and growth began and the fractures transported gas to the edges of the gel. Development of the fracture pattern continued for an additional 20 hours until the "final" pattern, shown in fig. 1, was obtained.

In parallel with the fracture experiment, the bottle for measuring the gas production rate, γ, was held at the same temperature as the Hele-Shaw cell. In the Exp_1 and Exp_2 the gas production rate increased steadily from zero, after ≈ 2 h the production rate had reached ≈ 0.7 ml/h and at 20 h it peaked at ≈ 2 ml/h.

Dynamics of fracture nucleation and growth. The first tiny bubble appeared in the gel after about 2 hours from the beginning of the experiment and 10–20 bubbles nucleated during the next 20 hours. Bubbles grew until they reached a diameter of approximately $l_0 = 2.3 \pm 0.2$ mm and then changed into elongated cracks with sharp tips after 12 ± 3 min. However, for about 50% of the fractures, an initial bubble nucleation and growth stage was not observed with the image resolution used in these experiment (see movies in the Supplementary Material: `crack_1_EPL_format.wmv`, `crack_4_EPL_format.wmv`). Crack tips propagated with increasing velocity, at both ends of the fractures, unless they became blunted or closely approached the boundary of the gelatine layer or another crack. During the free propagation regime, before cracks started interacting with other cracks or with the boundary, the crack length evolved with time as

$$l = l_0 \exp(t/\tau), \tag{1}$$

where t is the time since fracture nucleation. The increase in the timescale, τ with increasing gas production rate, γ, could be represented by $\tau = 0.54/\gamma - 0.20 \pm 0.017$ h. Each crack tip either propagated until it connected to another

fracture or reached the gel boundary, or it slowed down and eventually halted inside the gel matrix, forming a dead end. When a fracture was not connected to other fractures or the gel boundary, its aperture a increased with time due to increasing gas pressure until a maximum aperture of approximately 3 mm was reached along most of the fracture length. When two cracks intersected their apertures changed rapidly indicating pressure equilibration. When a crack reached the gel boundary, its aperture collapsed as the gas drained from the system in less than one second. Once a crack formed, it continued to serve as an intermittent drainage pathway that closed and opened. New fractures nucleated and propagated until a steady-state fracture pattern stabilized, see fig. 1A.

To analyze the development of the fracture pattern, the images of fractured gelatine were processed such that all pixels that were once covered by a fracture were preserved in accumulated images that represent the development of the fracture network. The final accumulated fracture pattern for experiment Exp_1 is displayed in fig. 1B.

In most cases, both crack tips propagated linearly, with about the same velocity, until they reached a distance of $\lambda_e = 10 \pm 5$ mm from another crack or a distance of 20 ± 5 mm from the gel edge. In such instances they would slow down, speed up, or change direction, depending on the circumstances. We will refer to λ_e as the elastic interaction length.

Using digital image correlation [17], the motion of tracer particles in the gel and of the gel edges was tracked. When cracks open, new volume is generated in the system, but no systematic expansion of the gel in the plane of the Hele-Shaw cell was found. However, by using an LVDT displacement sensor (Omega Engineering), we found that the glass plates confining the gel moved in the direction perpendicular to the plane of the Hele-Shaw cell plane, allowing the gel to increase in thickness. The total deflection of the plates corresponded to a total volume increase of $(1.9 \pm 0.1) \times 10^{-6}\,\mathrm{m}^3$. Since the gel is essentially incompressible, this corresponds to the volume of the gas trapped in the fractures and the largest total volume of the open fractures was estimated from image analysis to be $(2.2 \pm 0.1) \times 10^{-6}\,\mathrm{m}^3$.

Spatial distribution of fracture nucleation. To characterize the mechanisms of crack formation and growth we analyzed to what degree new fractures nucleate either in the middle of unfractured domains, near existing fractures, or randomly. When a crack formed it was assigned a number indicating the order in which it was formed as shown for experiments Exp_1 and Exp_2 in fig. 2A and B. Distance maps as shown in fig. 3 were computed where the colour indicates the distance $r(x, y)$ from the coordinate (x, y) to the closest fracture or free boundary. For each nucleation event i, the distance r_i, position, (x_i, y_i) and gradient $\nabla r(x_i, y_i)$ were determined just before nucleation occurred. On a line through (x_i, y_i) in the direction $\nabla r(x_i, y_i)$, the local maximum of r is denoted $r_{max,i}$.

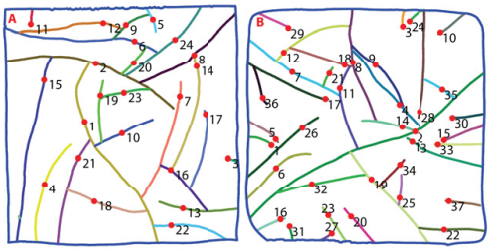

Fig. 2: A, B: nucleation sites and fracture labeling in Exp_1 (A) and Exp_2 (B). The fractures are distinguished by their colours and their numbers indicate the order in which they appeared. The red circles mark the nucleation sites.

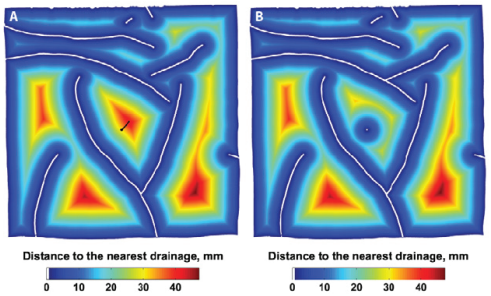

Fig. 3: Map of distance, $r(x, y)$ to the nearest fracture right before and after the nucleation of fracture 10 in fig. 2A. A: a line from (x_{10}, y_{10}) in the direction $\nabla r(x_{10}, y_{10})$ up to the position of the local maximum of r, $r_{max,10}$ is drawn in black. Panel B shows how the distance map is changed immediately following the nucleation of fracture 10. See supplementary movie `nucl_movie_EPL_standart.wmv`.

The normalized distance $r_i/r_{max,i} = 0$ or 1 correspond to nucleation at an existing fracture or in the middle of an unfractured domain. The cumulative distribution $N(r/r_{max} > r_i/r_{max,i})$, which is plotted in fig. 4, characterizes the degree of randomness in the locations of the nucleation sites and is fitted by $N = (r_i/r_{max,i})^{\mu}$, $\mu = 1.94$. $\mu \leqslant 1$ (the exact value depends on the shape of the unfractured area) corresponds to completely random nucleation and $\mu \to \infty$ corresponds to deterministic nucleation in the middle of an unfractured domain. The inset shows the cumulative distribution of r_i and demonstrates that there is a minimum distance between nucleation sites and pre-existing fractures.

Fracture growth direction. The direction of fracture propagation from the nucleation point was measured and it was found that the distribution of angles between the fracture directions and the distance gradients, $\nabla r(x_i, y_i)$, was uniform between 0 and 90 degrees.

Analysis of steady-state fracture pattern. The steady-state fracture network shown in fig. 1B was skeletonized

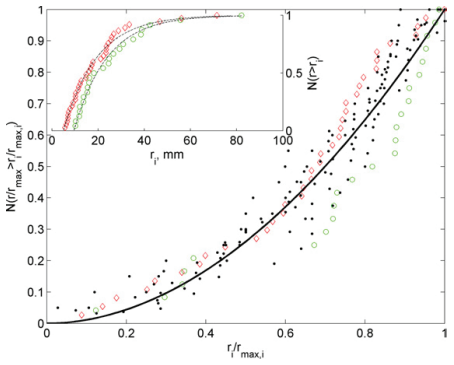

Fig. 4: Cumulative distribution of the normalized distances, $r_i/r_{max,i}$, from nucleation sites to the nearest drainage interface. Green data points correspond to Exp_1, red to Exp_2. The black dots correspond to randomly generated networks using the fragmentation fracture model. The continuous line is a fit of the data using the function $y = x^{\mu}$, $\mu = 1.94$. The inset shows the cumulative distributions of r_i. This indicates that there is a minimum distance between nucleation points and pre-existing fractures, r_{min} of about 5 and 10 mm in the 2 experiments.

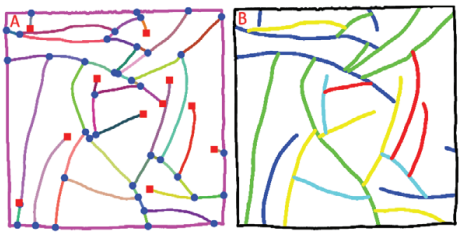

Fig. 5: Characteristics of the fracture network of Exp_1. A: fracture segments labeled with different colours. Blue discs indicate junctions between segments and red squares indicate dead ends. B: fracture network coloured according to the fracture generation number, n_C, of fracture C intersecting fractures A and B: $n_C = \max(n_A, n_B) + 1$. Black: 0; blue: 1; green: 2; yellow: 3; light blue: 4; red: 5.

and all intersections of fractures (blue circles in fig. 5A) and fracture tips (red squares in fig. 5A) were identified and labeled as *nodes*. A fracture may be divided into *segments* consisting of the part of the fracture between two adjacent nodes or between a node and an end of the fracture and these segments are identified by different colours in fig. 5A, (the outer boundary is considered to be one continuous segment).

At each node we measured the angles between intersecting segments. There were two distinct peaks: one in the range $180 \pm 5°$ and the other in the range $90 \pm 10°$. By joining segments that intersect at angles about 180°, we reconstructed the continuous fractures which formed by propagation from a single nucleation point. This fracture pattern has a temporal order of nucleation (see numbering in fig. 2). In addition a hierarchical order can be defined such that if fracture C ends at fractures A and B its generation number is $n_C = \max(n_A, n_B) + 1$, where n_A and n_B are the generation numbers of fractures A and B [6]. The draining perimeter is considered to be generation 0. In the experiments, up to five fracture generations ($n = 5$) were measured. In fig. 5B, the fractures of Exp_1 have been colour coded to indicate their fracture generation numbers. A fracture is "younger" than the youngest fracture it forms a junction with. One possible alternative generation numbering scheme emphasizing the drainage aspect of the network would be $n'_C = \min(n'_A, n'_B) + 1$, which corresponds to numbering of river segments in a drainage basin. Using this scheme the highest drainage generation is $n' = 3$.

Discussion and conclusion. – The experimental results were used to propose a mechanism of fracture nucleation and propagation. We now demonstrate that the fracture network has intermediate statistical properties between those of river-like and hierarchical-fracture–like patterns.

A diffusion-nucleation model for fracturing. The production of CO_2 provides the energy required for fracturing the gel and the fracture network evolution depends on the coupling between CO_2 transport and elastic interactions in the matrix. The observation that fractures initiate as bubbles far away from existing boundaries suggest that crack nucleation is not determined by elastic interactions. We therefore propose the following diffusion-nucleation model:

1) Most of the generated CO_2 is dissolved into the gel, which consists of 95% water. The solubility and diffusion coefficient of CO_2 in the gel are approximately the same as in pure water, $c_0 = 1.8\,\mathrm{g/l}$ and $D = 1.85 \cdot 10^{-9}\,\mathrm{m^2\,s^{-1}}$ [18]. The dissolved CO_2 has negligible mechanical effects on the gel matrix.

2) Bubbles nucleate when CO_2 generation leads to local supersaturation in the gel. Nucleation is heterogeneous and only a small supersaturation is required.

3) As bubbles grow they begin interacting elastically with the gel matrix and a transition from bubbles to fractures occurs.

4) The subsequent fracture propagation is driven by the gas pressure on the fracture walls which induces elastic stresses in the material.

Growth of a single fracture. After a fracture has nucleated it propagates when the gas pressure exceeds some critical value p_c. When fractures propagate slowly the gas pressure is constant and equal to p_c. Using the ideal gas approximation $p_c = \frac{n_{CO_2} RT}{V} = \mathrm{const}$, the change in fracture volume is

$$\frac{\mathrm{d}V}{\mathrm{d}t} = \frac{RT}{p_c} \frac{\mathrm{d}n_{CO_2}}{\mathrm{d}t}. \qquad (2)$$

The fracture aperture is limited to $a = 3\,\mathrm{mm}$ due to adhesion of the gel to the walls of the Hele-Shaw cell and the volume of gas in the fracture is $V \approx lah$, where l is the fracture length and $h = 3\,\mathrm{mm}$ is the distance between the glass plates. During propagation of a single fracture we assume a constant CO_2 flux, ϕ, over the fracture surfaces

$$\phi = \frac{\mathrm{d}n_{CO_2}}{\mathrm{d}t}\frac{1}{2lh} = \mathrm{const.} \tag{3}$$

The expression

$$l = l_0 \exp\left(\frac{2\phi RTt}{p_c a}\right), \tag{4}$$

for the fracture length can be derived by combining eqs. (2) and (3) and integrating. Here, l_0 is the integration constant, which characterizes the critical length above which a gas bubble evolves into a fracture. This corresponds to eq. (1), which was used to fit the experimental data and comparison of eqs. (1) and (4) indicate that $1/\tau \propto \phi \propto \gamma$.

Size of unfractured domains. Various factors control the final configuration of the fracture network. Since the gas production rate is virtually constant for a long period after the last fracture has stopped propagating we assume that the system reaches a quasi-steady state in which the fracture network drains the gel matrix sufficiently to hinder further fracturing. Using a diffusion-nucleation model, the characteristic size of unfractured domains, for which loss of CO_2 by diffusion is sufficient to prevent nucleation of new fractures can be estimated.

Consider a gel segment bounded by two parallel fractures separated by a distance 2δ. Assuming a constant CO_2 production rate, γ, the steady-state equation for the concentration field in the gel is

$$D\nabla^2 c + \gamma = 0. \tag{5}$$

We assume that the flux ϕ of CO_2 across a fracture surface is proportional to the difference between the concentration c of dissolved CO_2 at the surface and the concentration required for chemical equilibrium with the gas pressure $p = k_H c$ in the fracture, *i.e.*,

$$\phi = D\frac{\mathrm{d}c}{\mathrm{d}x}|_{x=\pm\delta} = k\left(\frac{p}{k_H} - c(\pm\delta)\right), \tag{6}$$

where k_H is the Henry's coefficient and k is a rate constant of CO_2 evaporation from the gel. The solution of (5) is

$$c(x) = \frac{p}{k_H} + \frac{\gamma\delta}{k} + \frac{\gamma}{2D}(\delta^2 - x^2). \tag{7}$$

We assume that to nucleate a bubble a critical supersaturation $c_c = p_c/k_H$ is needed. Inserting $c(x=0) = c_c$ into eq. (7) we may solve for the critical distance δ_c and find two scaling regimes:

- diffusion limited ($k \to \infty$), $\delta_c = \sqrt{\frac{2D}{\gamma}\frac{p_c - p}{k_H}} \propto \gamma^{-1/2}$,
- evaporation limited ($D \to \infty$), $\delta_c = \frac{k}{\gamma}\frac{p_c - p}{k_H} \propto \gamma^{-1}$.

It follows that in the diffusion-limited case $\gamma^{1/2}\delta_c$ should have a constant value and $\gamma\delta_c$ should have a constant value for the reaction-limited (evaporation-limited) case. In Exp_1 the mean production rate was $\gamma = 1.6$ ml/h and $2\delta_c = 22.2\,\mathrm{mm}$ ($\gamma\delta = 17.76$, $\gamma^{1/2}\delta = 14.0$) and in Exp_4 the mean production rate was $\gamma = 6.2\,\mathrm{ml/h}$ and $2\delta_c = 10.7\,\mathrm{mm}$ ($\gamma\delta = 33.2$, $\gamma^{1/2}, \delta = 13.3$). This is consistent with the diffusion-limited model, but not with the reaction-limited model. The shape of the cumulative distribution function (for $r_i/r_{max,i}$) shown in fig. 4, with $\mu = 1.94$, is also consistent with the diffusion-limited scenario, but not with the reaction-limited model since in the reaction-limited limit $\mu \leqslant 1$.

Elastic interactions, directed networks and loops. The short range of the elastic interactions is a consequence of the adhesion between the gel and the essentially rigid walls of the Hele-Shaw cell. A three-dimensional solid full of gas-filled fractures will also have a limited elastic interaction length due to the "screening" by open fractures. The elastic interaction between fractures in the model system results in the opening and closing of fracture apertures at junctions, which act as valves to the gas flow. This dynamic process, causing intermittent gas release, will be described in detail in a future communication. The adhesion between the gel and the glass walls of the Hele-Shaw cell also imposes an effective confinement on the system similar to the effects of compressive elastic stress on a three-dimensional system. Under such confining conditions, neighbouring fractures in analogous three-dimension systems will interact in a similar manner —when the aperture of one fracture increases due to increased fluid pressure it will increase the compressive stress on neighbouring fractures and this will reduce their apertures.

It should be noted that although $\delta_c \sim r_{min} \sim \lambda_e \sim 10\,\mathrm{mm}$ in experiments Exp_1 and Exp_2, the similarity between λ_e and the other lengths is fortuitous. The elastic interaction length λ_e does not depend on the gas production rate as do δ_c and r_{min} and elasticity does not control δ_c and r_{min}.

The direction of gas flow follows the direction of the pressure gradient, but because confinement induces elastic interactions between fractures and nearby fractures and junctions, which may act as valves when the gas pressure is reduced, the direction of the pressure gradient is not static. Because of the "valve closing" effect, fractures that are connected at one end to a fracture network that reaches the edge of the gel may propagate at the other end until that end also contacts a pre-existing fracture. The end result is a network with loops. A hierarchical-fracture network [6,7] is ideally fully connected.

Model of fracture propagation. A simple model that captures some of the essential features of our experimental system and incorporates river-like and hierarchical-fracture–like networks as limiting cases was developed (see fig. 6). A lattice model of size $L \times L$ was used, where L is

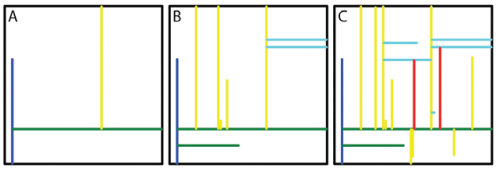

Fig. 6: Fragmentation fracture model with $\omega = 0.36$ shown at three stages of evolution, $l_t/L = 2.2, 5.1, 8.56$. The lines are coloured according to the fracture generation number, n_C, of fracture C intersecting fractures A and B: $n_C = \max(n_A, n_B) + 1$. Black: 0; blue: 1; green: 2; yellow: 3; light blue: 4; red: 5.

the size of the gelatine layer. Fractures nucleate and propagate sequentially and form a "final" pattern when the system is completely drained, *i.e.*, when the cumulative fracture length in the pattern exceeds or equals the cumulative fracture length l_t. l_t/L is 8.5 in Exp_1 and 8.7 in Exp_2. The nucleation sites are chosen according to a probability distribution $P(x, y)$ that depends on the distance from the site to the nearest fracture or boundary. We chose a power law distribution such that the probability of nucleating a fracture at site (x, y) is

$$P(x, y) = r(x, y)^{\mu-1} / \sum_{x,y} r(x, y)^{\mu-1}, \qquad (8)$$

where $r(x, y)$ is the distance from the nearest fracture or the boundary. This choice is justified by the experimental distribution (fig. 4), where the power law exponent was determined to be $\mu = 1.94 \pm 0.06$. The black dots in fig. 4 show the resulting cumulative distribution of $r_i/r_{max,i}$ of nucleation points for 20 realizations of the model. This demonstrates that although the model was constructed with a different metric from that used to measure μ an exponent of $\mu = 1.94$ makes the model nucleation distribution lie within the range of uncertainty of the experimental nucleation distribution.

Once a nucleation site is selected, the fracture orientation is randomly selected as horizontal or vertical. The fracture propagates by the same distance in both directions until it reaches and forms a junction with another fracture or the system boundary. At this instance the fracture may either cease to grow because it is drained by the joining fracture (with probability $1 - \omega$), or it may continue to grow until the other end meets an existing fracture (with probability ω). $\omega = 1$ corresponds to all fractures connected at both ends which is typical of a hierarchical-fracture pattern [6]. $\omega = 0$ corresponds to all fractures connected at one end only which is typical of river networks. The probability ω of a network can be deduced from the ratio between the number of dead ends, n_d, and the number of junctions, n_j: $\frac{n_d}{n_j} = \frac{1-\omega}{1+\omega}$ and ω are 0.41 and 0.32 for Exp_1 and Exp_2.

Conclusion. The generation and exsolution of CO_2 in a gel-filled Hele-Shaw cell generated a new type of drainage fracture network with topological properties intermediate between those of directed river networks and hierarchical-fracture networks. The valve-like opening and closing of fracture apertures at fracture junctions plays an important role in the formation of this type of fracture network. Diffusion of CO_2 in the gel inhibits the nucleation of new fractures in the vicinity of pre-existing fractures and a simple random nucleation model that takes this and the probability that fracture propagation stops before both ends of the growing fracture reach other fractures, reproduces key characteristics of the experimental fracture network.

* * *

We acknowledge support by the Petromaks program of the Norwegian Research Council. This study was supported by a Center of Excellence grant from the Norwegian Research Council to the Physics of Geological Processes Center (PGP).

REFERENCES

[1] Banavar J. R., Maritan A. and Rinaldo A., *Nature*, **399** (1999) 130.
[2] Dodds P. S. and Rothman D. H., *Phys. Rev. E*, **63** (2001).
[3] Rinaldo A., Banavar J. R. and Maritan A., *Water Resour. Res.*, **42** (2006).
[4] Zaliapin I., Foufoula-Georgiou E. and Ghil M., *J. Geophys. Res.: Earth Surf.*, **115** (2010).
[5] Goehring L. and Morris S., *Europhys. Lett.*, **69** (2005) 739.
[6] Bohn S., Douady S. and Couder Y., *Phys. Rev. Lett.*, **94** (2005).
[7] Cohen Y., Mathiesen J. and Procaccia I., *Phys. Rev. E*, **79** (2009).
[8] Sibson R. H., *J. Struct. Geol.*, **18** (1996) 1031.
[9] Davies J. H., *Nature*, **398** (1999) 142.
[10] Miller S. A., *J. Geophys. Res.: Solid Earth*, **107** (2002).
[11] Horton R. E., *Geol. Soc. Am. Bull.*, **56** (1945) 275.
[12] Alava M. J., Nukalaz P. K. V. V. and Zapperi S., *Adv. Phys.*, **55** (2006) 349.
[13] Andresen C. A., Hansen A., Le Goc R., Davy P. and Hope S. M., arXiv:1203.4510 (2012).
[14] McKenzie D., *Earth Planet. Sci. Lett.*, **74** (1985) 81.
[15] Ozkaya I., *Mar. Pet. Geol.*, **5** (1988) 293.
[16] Di Giuseppe E., Funiciello F., Corbi F., Ranalli G. and Mojoli G., *Tectonophysics*, **473** (2009) 391.
[17] Hild F. and Roux S., *Strain*, **42** (2006) 69.
[18] Li H. L., Wilhelmsen O., Lv Y. X., Wang W. L. and Yan J. Y., *Int. J. Greenhouse Gas Control*, **5** (2011) 1119.

Paper II:

Classification of fracture patterns by heterogeneity and topology

A. Hafver, E. Jettestuen, M. Kobchenko, D.K. Dysthe, P. Meakin and A. Malthe-Sørenssen

Published in EPL (Europhysics Letters), Vol. **105**(5), 2014, pp. 56004
doi:10.1209/0295-5075/105/56004

A Letters Journal Exploring the Frontiers of Physics

March 2014

EPL, **105** (2014) 56004
doi: 10.1209/0295-5075/105/56004

www.epljournal.org

Classification of fracture patterns by heterogeneity and topology

Andreas Hafver[1], Espen Jettestuen[2], Maya Kobchenko[1], Dag K. Dysthe[1], Paul Meakin[1,3] and Anders Malthe-Sørenssen[1]

[1] *Physics of Geological Processes, University of Oslo - Oslo, Norway*
[2] *International Research Institute of Stavanger - P.O. Box 8046, N-4068 Stavanger, Norway*
[3] *Temple University, Department of Physics - Barton Hall, Philadelphia, PA 19122-6082, USA*

received 26 November 2013; accepted in final form 26 February 2014
published online 13 March 2014

PACS 64.60.aq – Networks
PACS 47.70.-n – Reactive and radiative flows
PACS 64.60.av – Cracks, sandpiles, avalanches, and earthquakes

Abstract – Fracture patterns arise abundantly in natural and engineered systems, and their geometries depend on material properties and on the ways in which the material is deformed or forces act on it. Two-dimensional fracture patterns can be characterized by their network topology (how fractures connect to each other) and their heterogeneity (whether fractures appear clustered or uniformly distributed in space). We propose a generic model in which the topology can be adjusted by controlling the ratio between the number of dead ends and the number of junctions in the fracture network, and heterogeneity can be adjusted by biasing fracture nucleation to occur near or away from existing fractures. Based on this model we propose a characterization scheme for natural fracture systems and provide and demonstrate an algorithm for recovering model parameters from fracture pattern images.

Introduction. – The geometry of a fracture pattern is controlled by the forces that act on the fracturing solid, and depends on rheomechanical properties and material heterogeneities. The forces that drive fracturing may be externally imposed and/or internally generated. For example, fracturing in rocks may be driven by externally imposed tectonic forces and body forces (gravitational forces), or by internal forces, often associated with volume alterations in the solid [1]. Volume alterations may stem from volume-changing chemical transformations, phase transitions or non-uniform thermal expansion or contraction due to heating or cooling.

In porous solids, deformation may be coupled with the fluid pressure field in the pore space, and poroelastic phenomena become important [2]. If the permeability is high, fluids are effectively transported by Darcian flow, driven by gradients in fluid pressure, which prevents localized pressure accumulation and large pressure gradients. If the permeability is low and the fluid pressure changes locally at a higher rate than fluid transport can compensate for, stresses may build up and cause fracturing. This in turn alters the permeability and may create pathways for fluids to migrate through or drain from the solid [3]. Cracking of mud and other unconsolidated porous materials during desiccation is a familiar example of fracturing driven by fluid withdrawal, and hydraulic fracturing is an example of fracturing caused by fluid injection. More than a million oil and gas wells have already been hydraulically fractured [4], and recent application of this technology to the recovery of shale oil and shale gas has become a topic of great economic importance and wide public and professional interest and concern [5]. Fracture patterns produced by fluid injection have been studied experimentally and numerically by several authors, for example [6–8]. Hydraulic fracturing may also be driven by internal fluid production associated with chemical transformations in the solid. Examples include release of fluids from hydrous minerals in subduction zones, which can trigger earthquakes [9], and methane released by fracturing during degassing of sediments, which may have implications for the Earth's climate [10]. Primary migration (the formation of hydrocarbon fluids in source rocks and the expulsion of the hydrocarbons into secondary migration pathways) is believed to be accelerated

by pressure-induced fracturing when kerogen decomposes into lighter hydrocarbons [11–13].

The work described in this paper is concerned with fracturing in quasi–two-dimensional systems. Even in two-dimensional systems, fracture pattern geometry varies greatly, ranging from more-or-less polygonal or hierarchical patterns (osbserved in cracking mud, glazes on pottery or cracking paint films [1,14–16] and in two-dimensional simulations of rock weathering driven by solid volume-changing reactions [17]) to tree-like or branching patterns (observed in two-dimensional computer simulations and experiments on hydraulic fracturing [18]). A recent quasi–two-dimensional experimental model for fracturing during primary migration [19] generates fracture networks that are topologically intermediate between polygonal networks (with many loops) and trees (with many fractures terminating in dead ends). In these experiments, a layer of gelatin containing yeast and sugar is confined in a Hele-Shaw cell, and fracturing is driven by exsolution of dissolved CO_2 produced via fermentation. The intermediate topology is related to the complex dynamics of opening and closing of fractures and episodic expulsion of gas.

In the latter experiments CO_2 is generated more or less uniformly throughout the solid gelatin and diffuses down chemical potential gradients towards the boundaries of the Hele-Shaw cell and into fractures. Accordingly, fracturing initiates in the bulk, where CO_2 saturation is highest, and is inhibited near pre-existing fractures. As a result, there is no fracture branching, and fracture junctions only form when one fracture reaches another. In other systems, fractures nucleate at the external boundary or near existing fractures, for example when a brittle solid is cooled from the outside, when desiccation depends on transport of fluid to the exterior via open surfaces or when volume-changing chemical reactions localize near boundaries, where gradients in chemical potential are steepest [20–23]. In such cases, fractures penetrate from the outside of the solid towards the inside, and branching may occur. In nuclear fuel pellets both types of fracturing occur. The generation of fission gases generates fractures within the pellet [24], and the internal heating, which swells the inside of the pellet more than the outside, generates fractures that penetrate into the pellet from the outside [25]. In other systems, heterogeneity may play an important role, and can be a factor that leads to more randomly distributed nucleation.

In the next section we present a generic two-parameter model for simulating fracture patterns in two-dimensional systems. One parameter controls the ratio between the number of fracture junctions and the number of dead ends, quantifying the network topology. The other parameter controls the bias in nucleation position determined by the distance to the nearest fracture or external surface. This quantifies the heterogeneity of a fracture pattern, as nucleation close to existing surfaces leads to clustering of fractures. In the subsequent sections we demonstrate how model parameters may be recovered from the image of a generated pattern and show how the same scheme may be applied to quantify the geometry of real fracture networks.

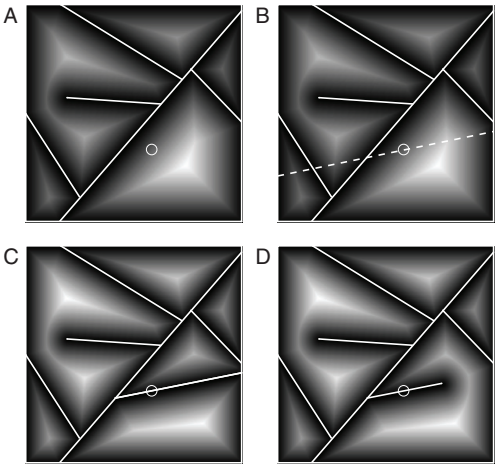

Fig. 1: Visualization of the model algorithm. (A) A map of distances $d_{i,j}$ to the nearest fracture (indicated by the grey scale) is calculated and the new fracture is nucleated at a random position, weighted by the distance map according to eq. (1) (indicated by the white circle). (B) A fracture direction is chosen randomly. (C) With probability ω the new fracture propagates until both ends meet existing fractures or boundaries. (D) With probability $1-\omega$ the new fracture halts when one of the ends meets an existing fracture or boundary.

Model. – The following generic model can be used to generate fracture patterns that vary in heterogeneity and topology. It is not constructed to mimic an actual fracturing process, although there may be instances where the driving mechanism can be related to the model parameters. Fractures are generated successively according to the following algorithm, illustrated in fig. 1:

1. Select a nucleation site $(i,j) \in \{1,L\} \times \{1,L\}$ with probability
$$P_{i,j} = d_{i,j}^{\gamma}/Z, \tag{1}$$
where $d_{i,j}$ is the distance to the nearest existing fracture or boundary and $Z = \sum_{i,j=1}^{L} d_{i,j}^{\gamma}$;
2. Select a random propagation direction;
3. Propagate the new fracture in both directions
   - until each end meets an existing fracture or boundary (with probability ω) or;
   - until one of the ends meets an existing fracture or boundary (with probability $1-\omega$) (the fracture extends from the nucleation point by equal distances in both directions).

The significance of the parameters ω and γ is illustrated in fig. 2, which shows examples of networks generated with

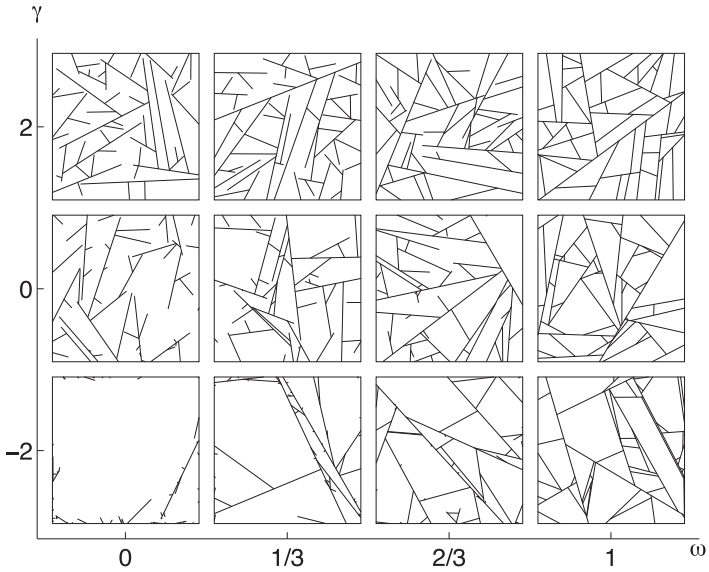

Fig. 2: Examples of model fracture networks produced with various values for γ and ω. The heterogeneity of the fracture patterns increases as γ is reduced, whereas ω regulates the network topology from tree (0) to polygonal (1). All examples were generated with $L = 256$ and contain 50 fractures.

this model. The parameter ω, which can be varied from 0 (trees) to 1 (polygons), is a measure of the network topology, and it can be related to the expected ratio of dead ends to junctions, R, by

$$R = (1 - \omega)/(1 + \omega). \tag{2}$$

The parameter ω quantifies the tendency of fractures to divide domains, which in turn may be related to the network's ability to relieve stresses or drain fluids. In the gelatin experiments of [19], for example, fractures tend to halt if they are able to expel gas through existing pathways. The parameter γ quantifies where new fractures nucleate relative to existing fractures, and may depend on loading, material heterogeneities and the mechanisms driving the fracturing process. For negative γ new fractures nucleate close to existing ones, so the process is surface driven and produces heterogeneity. For positive γ the process is bulk driven and leads to homogeneous patterns.

Regularisation of (1) becomes a problem as the resolution L tends to infinity for negative γ. In this case Z diverges, indicating that fractures prefer to nucleate arbitrarily close to existing fractures. This is not a problem for our finite-resolution simulations, but the probability for nucleation close to a fracture is sensitive to resolution. In practice we believe that the case $\gamma \ll 0$ is of limited interest, as nucleation near existing fractures dominates even for moderately low γ values. It should, however, be kept in mind that higher resolution is required to distinguish fracture patterns as γ becomes more negative.

Measurement of network parameters. – Figure 2 illustrates that both γ and ω have visually distinct effects on the generated fracture patterns, suggesting that these parameters may be suitable quantities for characterizing real fracture networks. We introduced a special case of this model in [19] and were able to estimate model parameters from the time evolution of experimental networks, but in order to be more useful for characterizing real fracture patterns, we require that they can be estimated from a single image of a developed fracture network.

The quantity ω is readily found by counting the number of dead ends and junctions in the network and taking the ratio R. ω can then be recovered from eq. (2).

An approximate temporal hierarchy can be deduced from the intersections in a fracture network: If a fracture i terminates on a fracture j, it indicates that i existed before j. Fracture i is then called a direct descendant of j, and j is a direct ancestor of i. This observation is exploited in the algorithm for estimation of γ from images, which is described below and illustrated in fig. 3:

1. Identify fractures and network connectivity:
   (a) Binarize and skeletonize the fracture network.
   (b) At each junction, determine which of the adjacent segments form part of the same fracture, and remove a pixel between continuous fractures and incident (descending) fractures. After this procedure, each fracture corresponds to a connected set of pixels (not necessarily on a straight line).

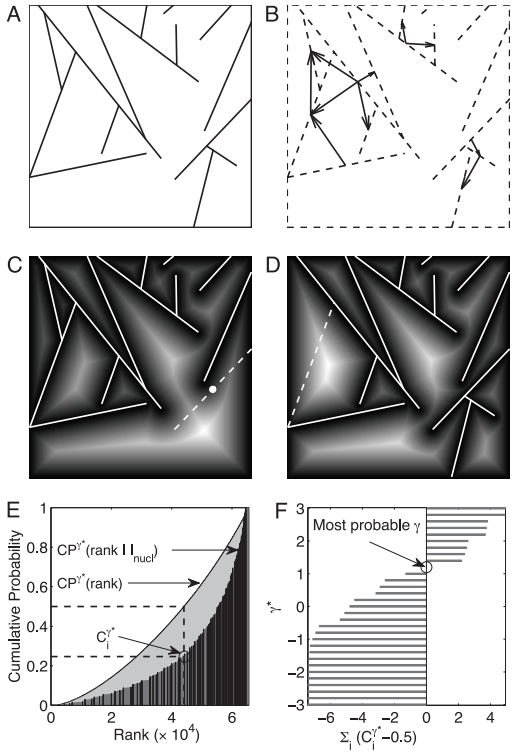

Fig. 3: Illustration of the algorithm for measuring γ. (A) The fracture pattern to be analysed. (B) An approximate temporal hierarchy can be deduced from the fracture intersections. The fracture pattern at the time of nucleation of a particular fracture is assumed to consist of all fractures not descending from it (arrows point from ancestors to descendants). (C) Assumed distance map at the time of nucleation of the fracture (dashed line). This fracture has a dead end, and, according to the model, must have nucleated at the midpoint (white dot). (D) Assumed distance map at the time of nucleation of the fracture (dashed line). This fracture has no dead end, hence the nucleation point can be anywhere on the dashed line. (E) For a range of trial values γ^* and for each fracture i, the cumulative nucleation probabilities $CP_i^{\gamma^*}(\text{rank})$ and $CP_i^{\gamma^*}(\text{rank}|I_{nucl})$ are plotted (where I_{nucl} is the set of putative nucleation sites, highlighted in black). $C_i^{\gamma^*}$, the value of the latter at the point where the former reaches 0.5, is recorded (probabilities are given by eq. (1). (F) The most likely value of γ corresponds to the interception in the plot of $\sum_i (C_i^{\gamma^*} - 0.5)$ *vs.* γ^*.

(c) A fracture's ancestors are found by searching for fractures within two pixels from its endpoints.

2. For each fracture $i \in \{1, 2, \ldots, N\}$:

(a) Make a binary image including all fractures but fracture i and its direct or indirect descendants;

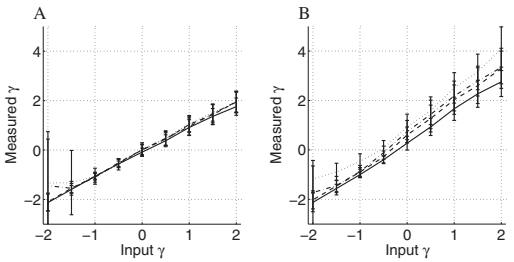

Fig. 4: γ measured from model systems of size 800×800 containing 50 fractures. (50 repetitions per (ω, γ) duplex). Measured γ as a function of input γ is plotted as mean $\pm$ standard deviation. (A) Using known temporal sequence. (B) Using approximate temporal sequence.

(b) Calculate the distance transform of this image, and rank points in the image according to their distance $d_{i,j}$ from existing fractures;

(c) Identify a set of putative nucleation points, I_{nucl}:
- If fracture i has one ancestor, let I_{nucl} be the center point;
- Otherwise let I_{nucl} be the set of all pixels on fracture i;

(d) For a list of trial values γ^*:

i. Calculate the cumulative distribution $CP_i^{\gamma^*}$ (rank) of nucleation probabilities by accumulating the probabilities $P_{i,j} = d_{i,j}^{\gamma^*}/Z$ for the ranked points.

ii. Repeat i) but restrict the sum to putative nucleation sites to obtain $CP_i^{\gamma*}(\text{rank}|I_{nucl})$.

iii. Store $C_i^{\gamma^*}$, the value of $CP_i^{\gamma^*}(\text{rank}|I_{nucl})$ at the point where $CP_i^{\gamma^*}(\text{rank}) = 0.5$.

3. The most likely γ^* value is the one that minimizes $\left|\sum_{i=1}^{N}(C_i^{\gamma*} - 0.5)\right|$.

Figure 4 shows the result of measuring γ from images of networks generated with the model. When the known temporal sequence is used, our algorithm successfully recovers the model parameters, with the exception of small γ values. When the approximate temporal hierarchy is used, there is a linear correspondence between the estimated and input values of γ, although there is a systematic overestimation of γ which increases with both ω and the input γ. The discrepancy is not surprising given that the distance maps used in the measurement algorithm assumes the existence of too many fractures at the time of nucleation. This shifts the distance map towards smaller distances and result in a bias towards higher $C_i^{\gamma^*}$ values in step 2(d)iii. of the measurement algorithm.

Using least-squares fitting we determine that the discrepancy can be compensated for by transforming the measured γ value according to

$$\gamma \to 0.7\gamma_e - 0.6\omega - 0.3. \tag{3}$$

It may be possible to reduce the systematic errors by approximating the time evolution differently. Instead of keeping all fractures but a fracture's descendants and itself, we attempted to keep only direct ancestors, but this resulted in poorer estimates than the method proposed here. One could imagine more elaborate schemes, such as averaging over all allowed temporal sequences, but the number of possibilities grows rapidly with increasing system size, making it impractical. Tests using random temporal sequences resulted in apparently random γ values, showing again that the temporal sequence matters.

Applications to natural fracture networks. – Figure 5 show three applications of the proposed classification scheme to natural fracture systems. The pattern in fig. 5(A) was produced during CO_2 expulsion from a layer of confined gelatin containing yeast that ferments sugar and generates CO_2, and it is taken from [19]. For this example we determine that $\omega \approx 0.6$ and $\gamma \approx 1.4$ using the procedure described above. The intermediate value of ω reflects the many dead ends in the network. They arise because fracturing is driven by gas pressure in the fractures, and once a pathway exists for the gas to escape through, further fracture propagation is inhibited. The positive γ is in accordance with the CO_2 transport in the gelatin being diffusion limited, as discussed in [19]; fractures nucleate far from existing fractures, where the CO_2 supersaturation is highest.

Figure 5(B) shows ice fractures on Mars [26]. For this example we measure $\omega \approx 0.5$ and $\gamma \approx 0.3$. The pattern is slightly more heterogeneous than fig. 5(A), with more variation in domain sizes and fracture spacing. The patterns in fig. 5(A) and fig. 5(B) are topologically similar, but in some cases the fractures in fig. 5(B) are difficult to trace so this is subject to interpretation.

Figure 5(C) is taken from [27] and shows spheroidal weathering fractures observed along a road section at Nico Malan Pass, South Africa. For this example we measure $\omega \approx 0.9$ and $\gamma \approx -0.1$. The pattern is hierarchical with sequentially subdivided domains, reflected in the high value obtained for ω. The sequential splitting of domains also accounts for the slightly negative γ value. For this example the fracture tracing is sometimes ambiguous, and some regions are finely fragmented. With better resolution one would therefore expect to measure a lower γ value.

In certain experiments the temporal evolution of a fracture system is recorded, and our scheme can be used to estimate γ based on actual distance maps at the time of nucleation. We did this for the gelatin experiments in in fig. 5(A) and obtained $\gamma = 2.3$, which is close to the value, $\gamma = 1.94$, reported by Kobchenko *et al.* [16]. The value we found by mapping the crack pattern onto the generic model and correcting with (5) was $\gamma = 1.4$, and even though both γ values suggest prounounced nucleation far from other cracks the numerical values differ. There may be several reasons for this difference: the statistical uncertainty stemming from the small number of fractures

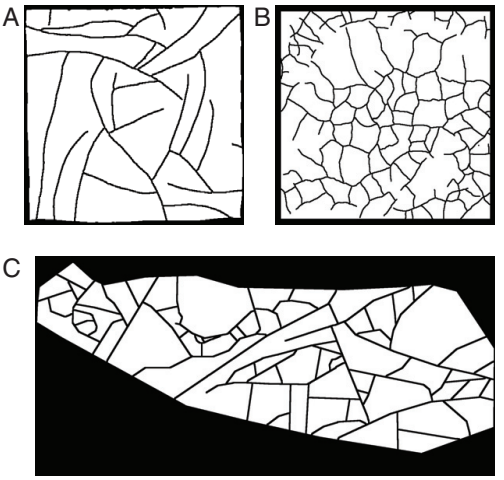

Fig. 5: Examples of natural fracture systems: (A) Fracturing in a layer of gelatin enclosed in a Hele-Shaw cell driven by the uniform production of CO_2 (from [19]). Measured (corrected) parameters: $\omega = 0.6$ and $\gamma = 1.4$. (B) Ice fractures on Mars (from [26]). Measured (corrected) parameters: $\omega = 0.5$ and $\gamma = 0.3$. (C) Spheroidal weathering fractures from Nico Malan Pass, South Africa (S32.50780, E026.80417) (from [27]). Measured (corrected) parameters: $\omega = 0.9$. and $\gamma = -0.1$.

and the differences between the model and the real physical system. For example, some fractures in fig. 5(A) grow simultaneously, so the assumption of a strict sequential growth is not valid. In general we assume that the rate of nucleation is low compared to the propagation speed for the model to produced the correct dynamics. Even if this is not the case we can think of our scheme as a method to obtain quantitative measures that can be used to compare patterns. The details of the driving mechanism and evolution are factors that determine where the pattern is mapped in the model's parameter space.

Discussion and conclusion. – We have presented a simple generic model for generating two-dimensional fracture networks, and the two model parameters can be used to classify fracture networks according to their spatial heterogeneity and topology. One of the parameters controls the bias in the position at which new fractures nucleate, away from or towards external surfaces or existing fractures, which adjusts the homogeneity of the fracture pattern. The other parameter controls the topology, defined by the ratio between the number of dead ends and the number of junctions in the network, and it can range from 0 (trees) to 1 (polygons). We devised a scheme for measuring the model parameters from images of fracture patterns and were able to recover the parameters from generated networks. We also classified three natural fracture systems to demonstrate the scheme.

Our work complements the vast amount of literature focusing on the scaling of unfractured domain sizes

and fracture lengths, in the field, in laboratory experiments and in simple fracturing and fragmentation models [28–30]. The parameters ω and γ are, in principle, independent of the scale of the pattern. In practice, parameter estimates are better for larger systems with many fractures (due to better statistics), but more inaccurate if the unfractured domains are small compared to the lattice resolution.

The two parameters of our classification scheme are intuitively related to the appearance of a pattern, are relatively simple to measure and work for intermediate network topologies. However, we stress that the model is not intended to mimic the dynamics of a fracturing process, and it does not address all aspects of fracture network geometry. For example, the model does not respect the effects of elastic interactions, which would affect the direction of fracture propagation and intersection angles between fractures. To include this, one could bias the direction of fracture propagation depending on the direction of surrounding fractures. The assumption of random fracture directions is justified in systems where stress is localized by the attachment to a substrate, such as drying mud or paint films [14–16] or experiments in Hele-Shaw cells [18,19].

Certain features of fracture networks cannot be produced by the model, but can still be accommodated by the classification scheme: Firstly, the model prohibits fracture branching, but this can be handled in the classification scheme by grouping of branches. Secondly, the model evolves fractures sequentially and avoids situations where co-evolving fractures mutually descend from each other in the approximated temporal hierarchy. To resolve this, one may assume that fractures forming a loop in the temporal hierarchy nucleated at the same instant. An extension of the model to three dimensions is possible by representing fractures as planes propagating radially outward from nucleation sites. A decision would have to be made concerning, for example, what happens as fractures meet, but such details should not be a problem for the classification of natural networks, where ω may be defined as the ratio of the total length of the free fracture boundaries to the total length of intersection lines between pairs of fractures.

* * *

This work was supported by the Norwegian Research Council, through the Petromaks project and a Center of Excellence grant to the Physics of Geological Processes Center (PGP).

REFERENCES

[1] Cohen Y., Mathiesen J. and Procaccia I., *Phys. Rev. E*, **79** (2009).
[2] Biot M. A., *J. Appl. Phys.*, **12** (1941) 155.
[3] Bons P. D. and van Milligen B. P., *Geology*, **29** (2001) 919.
[4] Association of American State Geologists, *Hydraulic fracturing* (2012), `http://www.stategeologists.org/fact_sheet.php`.
[5] Massachusetts Institute of Technology Energy Initiative, *The future of natural gas* (2011), `http://mitei.mit.edu/publications/reports-studies/future-natural-gas`.
[6] Flekkøy E. G., Malthe-Sørenssen A. and Jamtveit B., *J. Geophys. Res.*, **107** (2002) 2151.
[7] Niebling M. J., Toussaint R., Flekkøy E. G. and Måløy K. J., *Phys. Rev. E*, **86** (2012) 061315.
[8] Ghani I., Koehn D., Toussaint R. and Passchier C. W., *Pure Appl. Geophys.*, **170** (2013) 1685.
[9] Davies J. H., *Nature*, **398** (1999) 142.
[10] Etiope G. and Klusman R. W., *Chemosphere*, **49** (2002) 777.
[11] Ozkaya I., *Mar. Pet. Geol.*, **5** (1988) 293.
[12] Ozkaya I., *Mar. Pet. Geol.*, **5** (1988) 170.
[13] Kobchenko M., Panahi H., Renard F., Dysthe D. K., Malthe-Sørenssen A., Mazzini A., Scheibert J., Jamtveit B. and Meakin P., *J. Geophys. Res.: Solid Earth*, **116** (2011) B12201.
[14] Bohn S., Douady S. and Couder Y., *Phys. Rev. Lett.*, **94** (2005).
[15] Bohn S., Pauchard L. and Couder Y., *Phys. Rev. E*, **71** (2005).
[16] Bohn S., Platkiewicz J., Andreotti B., Adda-Bedia M. and Couder Y., *Phys. Rev. E*, **71** (2005).
[17] Iyer K., Jamtveit B., Mathiesen J., Malthe-Sørenssen A. and Feder J., *Earth Planet. Sci. Lett.*, **267** (2008) 503.
[18] Lemaire E., Levitz P., Daccord G. and Van Damme H., *Phys. Rev. Lett.*, **67** (1991) 2009.
[19] Kobchenko M., Hafver A., Jettestuen E., Galland O., Renard F., Meakin P., Jamtveit B. and Dysthe D. K., *EPL*, **102** (2013) 66002.
[20] Bahr H.-A., Fischer G. and Weiss H.-J., *J. Mater. Sci.*, **21** (1986) 2716.
[21] Goehring L. and Morris S. W., *J. Geophys. Res.: Solid Earth*, **113** (2008) B10203.
[22] Yakobson B., *Phys. Rev. Lett.*, **67** (1991) 1590.
[23] Malthe-Sørenssen A., Jamtveit B. and Meakin P., *Phys. Rev. Lett.*, **96** (2006) 245501.
[24] Kutty T., Chandrasekharan K., Panakkal J. and Ghosh J., *J. Mater. Sci. Lett.*, **6** (1987) 260.
[25] Olander D., *J. Nucl. Mater.*, **389** (2009) 1.
[26] Portyankina G., Pommerol A., Aye K.-M., Hansen C. J. and Thomas N., *J. Geophys. Res.: Planets*, **117** (2012) E02006.
[27] Royne A., Jamtveit B., Mathiesen J. and Malthe-Sorenssen A., *Earth Planet. Sci. Lett.*, **275** (2008) 364.
[28] Bonnet E., Bour O., Odling N., Davy P., Main I., Cowie P. and Berkowitz B., *Rev. Geophys.*, **39** (2001) 347.
[29] Darcel C., Bour O., Davy P. and De Dreuzy J., *Water Resour. Res.*, **39** (2003).
[30] Korsnes R., Souza S., Donangelo R., Hansen A., Paczuski M. and Sneppen K., *Physica A: Stat. Mech. Appl.*, **331** (2004) 291.

Paper III:

Network Formation by Contact Arrested Propagation

A. Hafver, E. Jettestuen, J.M. Baetens and A. Malthe-Sørenssen

Published in Physica A, Vol. **413**, 2014, pp. 240-255
doi:10.1016/j.physa.2014.07.006

Physica A 413 (2014) 240–255

Contents lists available at ScienceDirect

Physica A

journal homepage: www.elsevier.com/locate/physa

Network formation by contact arrested propagation

Andreas Hafver [a,*], Espen Jettestuen [b], Jan M. Baetens [c], Anders Malthe-Sørenssen [a]

[a] Physics of Geological Processes, University of Oslo, P.O. Box 1048 Blindern, 0316 Oslo, Norway

[b] International Research Institute of Stavanger, P.O. Box 8046, N-4068 Stavanger, Norway

[c] KERMIT, Department of Mathematical Modelling, Statistics and Bioinformatics, Coupure links 653, 9000 Gent, Belgium

HIGHLIGHTS

- A new network growth model is presented, termed Contact Arrested Propagation (CAP).
- The model may be formulated on arbitrary networks or on lattices in any dimension.
- We investigate the scaling of model properties and discover universal features.
- Suggested applications of the model include fracture and fragmentation processes.
- The model could be used to generate three-dimensional fracture networks.

ARTICLE INFO

Article history:
Received 22 January 2014
Received in revised form 5 March 2014
Available online 5 July 2014

Keywords:
Networks
Fracturing
Fragmentation
Percolation
Cellular automata
Substitution systems

ABSTRACT

We propose here a network growth model which we term Contact Arrested Propagation (CAP). One representation of the CAP model comprises a set of two-dimensional line segments on a lattice, propagating independently at constant speed in both directions until they collide. The generic form of the model extends to arbitrary networks, and, in particular, to three-dimensional lattices, where it may be realised as a set of expanding planes, halted upon intersection. The model is implemented as a simple and completely background independent substitution system.

We restrict attention to one-, two- and three-dimensional background lattices and investigate how CAP networks are influenced by lattice connectivity, spatial dimension, system size and initial conditions. Certain scaling properties exhibit little sensitivity to the particular lattice connectivity but change significantly with lattice dimension, indicating universality. Suggested applications of the model include various fracturing and fragmentation processes, and we expect that CAP may find many other uses, due to its simplicity, generality and ease of implementation.

1. Introduction

Networks and the processes forming them are topics of interest in a wide range of disciplines. Branching, tree-like networks are common in systems where effective transport of mass, energy or charge is required, including river networks, leaf veins, blood vessels and lightning patterns. Rinaldo, Banavar and Maritan discuss scaling properties of such networks [1] and how they may result from an imperfect search process to optimise network function [2]. Kramer and Marder [3],

* Corresponding author. Tel.: +47 99573565.
E-mail address: andreas.hafver@fys.uio.no (A. Hafver).

http://dx.doi.org/10.1016/j.physa.2014.07.006

Fig. 1. Snapshots of fracture evolution driven by CO_2 exsolution following fermentation in a confined layer of gelatine containing yeast and sugar. These experiments are presented in Ref. [28].

Takayasu and Inaoka [4] and Leheny and Nagel [5] have shown how river networks may be modelled using simple landscape erosion models, and others have used even simpler models to model drainage network formation, including Leopold and Langbein [6] and Meakin et al. [7], who represented the process by self-avoiding random walks on lattices. Other models for drainage network formation include diffusion limited aggregation models, studied by Meakin [8] and Masek and Turcotte [9], which produce fractal networks.

Fractal networks also arise in percolation systems, which are reviewed by Stauffer and Aharony [10] and by Sahimi [11]. Percolation models have received attention both from mathematicians and from scientists in more applied fields. For example, percolation models have been used for estimating the permeability in petroleum reservoirs [12] or conductivity of disordered materials [13], and invasion percolation models are used to model fluid–fluid displacement processes in porous media [14].

A range of models for generating artificial fracture networks are used in the geosciences to model flow processes in fractured porous media, with applications to, for example, hydrology, petroleum systems or the spread of chemical or nuclear contaminants in geological formations. Adler and Thovert [15] discuss several such network models from a theoretical perspective. Similarly, many authors have proposed simple models of fragmentation processes, including Steacy and Sammis [16], Hernández and Herrmann [17] and Fortes and Andrade [18]. Korsnes et al. [19] devise a fragmentation network model to study the dynamic process of breaking and healing of sea ice, and Iyer et al. [20] use a statistical network approach to model reaction-assisted hierarchical fracturing of rock.

A vast literature has also been devoted to the study of random graphs with random connectivity, starting with Erdös and Rényi [21]. Recently, much attention has been given to the study of so-called complex networks with non-trivial topology, for example social, communication and biological networks. Albert and Barabási review common statistical properties of complex networks and the mechanisms responsible for their formation [22]. They also introduced the preferential attachment model for organisation of complex networks [23]. Watts and Strogatz propose a model that can tune networks from regular to random by starting from a regular graph and rewriting connections randomly [24].

Wolfram [25] has pioneered a variety of network forming processes and models based on simple deterministic rules, and has applied these ideas across scientific disciplines, from the context of biological growth to a fundamental theory of physics. Networks formed by replacing nodes based on the local network structure has been explored further by Morrow et al. [26], Southwell et al. [27] and others.

The model presented here was inspired by the kind of fracture networks described by Kobchenko et al. [28] and illustrated in Fig. 1. Uniform production of CO_2 by a fermentation process causes nucleation of bubbles, and the bubbles develop into fractures, as a consequence of accumulating gas pressure. Fractures propagate until meeting other fractures or an external boundary, allowing the gas to escape through open network pathways. As an idealisation, this process may be viewed as a set of line segments propagating on a lattice according to some rule. The latter idea was refined and generalised into the generic model defined in the next section, which we choose to term Contact Arrested Propagation (CAP).

The CAP model may be related to several of the network forming processes mentioned above. It is general, and may be defined on arbitrary networks, including random graphs, complex networks or lattices (i.e. spatially embedded networks). In the spirit of Wolfram, the model evolves according to a simple deterministic rule, and, when represented on a lattice, it may be studied within the framework of percolation theory. Certain realisations of the CAP model bear resemblance to existing fracture and fragmentation models, such as those referred to above, and this is therefore a field where our model may find useful applications.

In this study, we focus our attention on certain representations of the CAP model on one-, two- and three-dimensional lattices, but investigate them as abstract systems without regard to any particular application. This approach allows us to identify whether aspects of the model's behaviour are generic, or rather artefacts of the representation on a particular background. We return to possible applications of the model in Section 4.2.

2. Model

Before presenting a formal definition of the CAP model, we illustrate it by providing a simple example of a particular model representation. In this example, the elements of our system are the edges of a square lattice, and the edges may

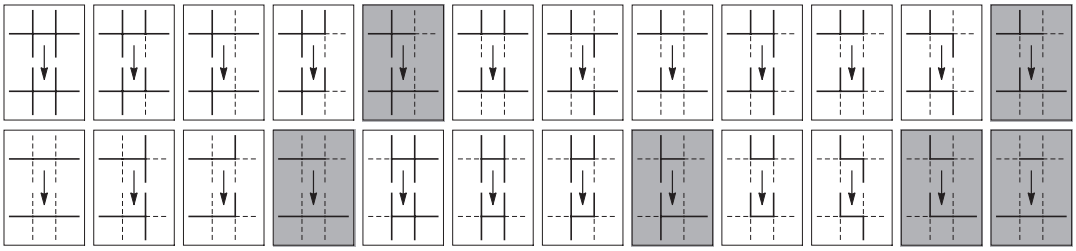

Fig. 2. Transition rules on a square lattice. Active edges (highlighted) may activate adjacent edges, depending on their local environment (i.e. the states of neighbours). Configurations that lead to activation of neighbours are highlighted with grey background.

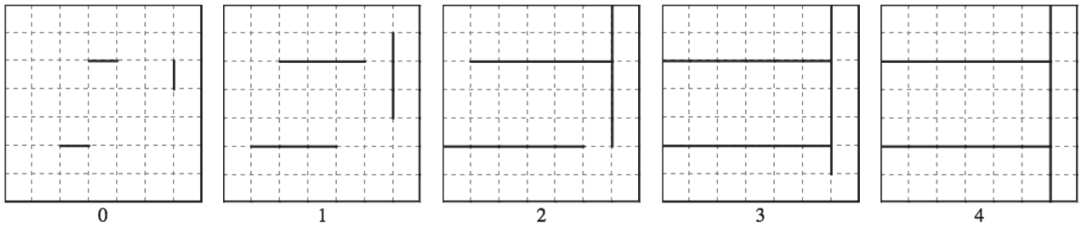

Fig. 3. Sequence of evolution steps for CAP system on a square lattice.

be either active or inactive. The system is initialised with a certain number of active edges, and at each iteration an active edge may propagate by activating parallel adjacent edges. The condition for propagation in a particular direction is that all edges adjacent on that side are inactive. This can be stated as a set of transition rules, as illustrated in Fig. 2. On this particular lattice, an active element may have 64 distinct neighbour configurations, which reduce to 24 by accounting for symmetries.

A typical evolution of a CAP network on a square lattice is shown in Fig. 3. It is clear that the chosen rules produce line segments that propagate straight ahead until encountering other segments, illustrating that the CAP model may be set up to produce behaviour resemblant of fracturing processes, such as those in Fig. 1. However, the specification of the evolution rules in Fig. 2 is cumbersome and specific to the square lattice. Below we provide a more abstract formulation of the CAP model, which allows its extension to arbitrary networks.

2.1. Formal definition of the CAP model

The basic entity of the CAP model is a collection of elements, E, where each element $e \in E$ is assigned a state variable $s_e \in \{0, 1\}$ and is connected to a set of neighbourhoods $N_e = \{N_e^1, N_e^2, \ldots\}$. These neighbourhoods are ordered lists of neighbouring elements, i.e. $N_e^i = \{n_e^{i,1}, n_e^{i,2}, \ldots\} \subset E$. The ordering of the neighbourhood lists is discussed below.

Evolution of the system is governed by the following rule: if $s_e = 1$, the first element of neighbourhood N_e^i will be activated (i.e. $s_{n_e^{i,1}} \to 1$), provided that all the elements in N_e^i are in state 0. Once activated, elements will remain in state 1. Eventually, the system will reach a final configuration where no further activation is possible.

In the present study we have chosen a synchronous update scheme, because using an asynchronous scheme would require a justification for the particular choice of update sequence. The effects of synchronous and asynchronous update methods have been discussed by several authors in the context of cellular automata, including Schönfisch and de Roos [29] and Bandini, Bonomi and Vizzari [30].

2.2. Representations of the CAP model

The definition of an element and its neighbourhoods is a matter of choice and depends on the underlying network. Fig. 4 shows a few examples of model representations on various lattices. On one- and two-dimensional lattices we choose to identify elements by lattice edges and group adjacent elements into neighbourhoods according to the vertices they share (Fig. 4 (A)–(D)). In the two-dimensional systems (Fig. 4 (B)–(D)), for a given element e, the neighbourhoods are sorted in ascending order, according to the dot product of unit vectors pointing, respectively, from the centre of e and the neighbour $n_e^{i,j}$ towards their common node. In this way, propagation is favoured along paths that extend straight ahead. This is generalised to three dimensions by using planes as elements and grouping neighbours into neighbourhoods by shared edges (Fig. 4 (E)).

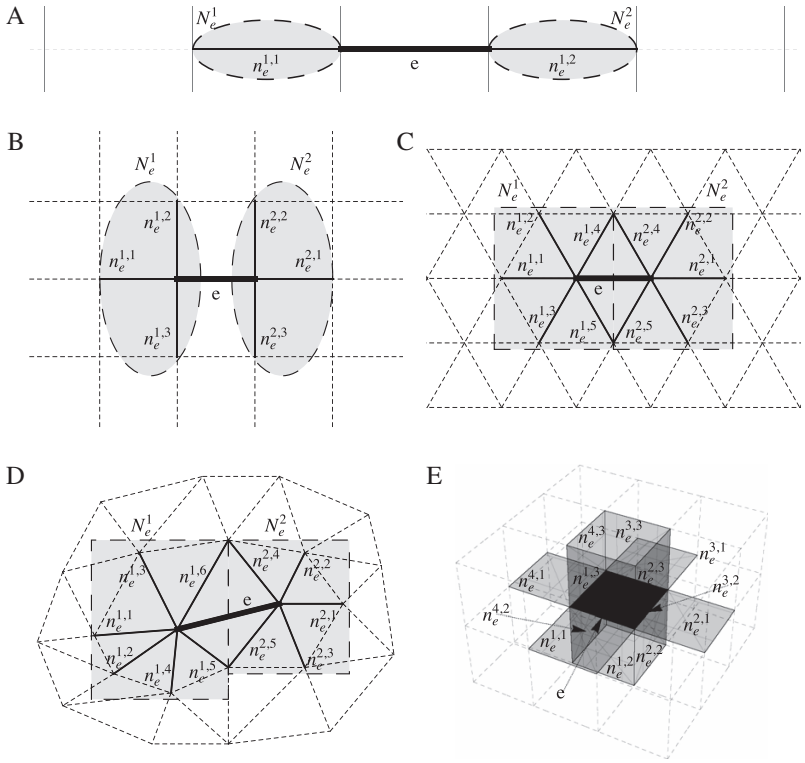

Fig. 4. Examples of model representations on various background lattices, illustrating how a typical element is connected to neighbourhoods of adjacent elements. (A) Linear lattice. (B) Square lattice. (C) Regular triangular lattice. (D) Unstructured triangular lattice. (E) Cubic lattice.

The neighbourhoods are sorted in ascending order according to the dot product of unit vectors lying inside each element and pointing perpendicularly towards their common edge. Fig. 5 shows examples of networks produced by the CAP model using the representations illustrated in Fig. 4.

As indicated in Fig. 2, the CAP model could be implemented as a generalised cellular automaton, where each element is updated at every time step according to its state and the state of its neighbours. However, since any element changes its state at most once during a simulation, the system may be implemented more efficiently as a substitution system. With this approach, one starts from a list of initially active elements ("seeds"), and at every iteration each element in the list is replaced by the adjacent elements that it activates. In Appendix A we describe a substitution algorithm which is completely background-independent.

3. Results

In this section, CAP networks on linear, square, regular triangular, unstructured triangular and cubic lattices, as illustrated in Figs. 4 and 5, are considered. All systems were evolved from a random initial condition with a specified density, ρ_i, of initial seeds. System size is measured as the number of elements on the respective lattices. Data was collected from 30 repeated simulations for every set of parameters.

3.1. Density evolution

For the one-dimensional CAP system, growth will only terminate once all elements have been activated, and the final density, ρ_f, will be 1, regardless of the initial density, ρ_i. For the two- and three-dimensional systems, ρ_f is governed by the competition between the number of initial seeds that are growing and how far each seed is able to propagate. In general, the propagation rule will prohibit some elements from being activated, and, unless $\rho_i = 1$, the final density will remain below 1. If ρ_i is high (i.e. close to 1) very few seeds will be able to activate neighbours, and ρ_f will remain close to ρ_i. If the density of seeds is very low (i.e. ρ_i close to 0), most seeds can propagate far in each direction before encountering other active elements, and the density may increase manyfold.

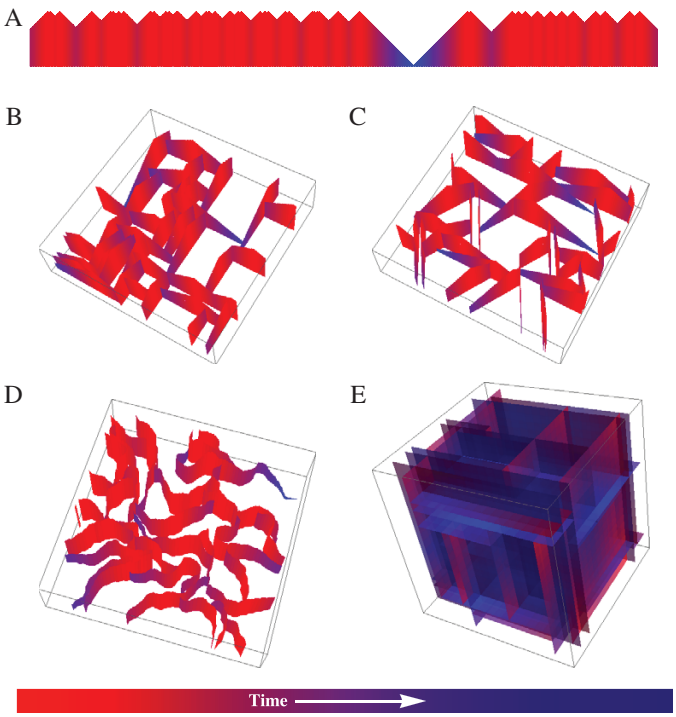

Fig. 5. Examples of CAP networks generated on various background lattices. The colour transition from red to blue indicates the passage of time. In the one- and two-dimensional examples, time evolution is also indicated by the height of the segments, such that peaks correspond to the initial seeds, which spread out with time. (A) Linear lattice. (B) Square lattice. (C) Regular triangular lattice. (D) Unstructured triangular lattice. (E) Cubic lattice. (For interpretation of the references to colour in this figure legend, the reader is referred to the web version of this article.)

Fig. 6 shows how the change in density, $\Delta\rho = \rho_f - \rho_i$ and ρ_f change as a function of ρ_i for the two- and three-dimensional systems. The graphs show that maximal growth occurs at a particular value of ρ_i. Among the two-dimensional systems, this optimal ρ_i is fairly similar and close to 0.1, but the value of the maximal growth varies significantly between the square and the regular and unstructured triangular lattices. The reason for this is that elements on the square lattice have three neighbours per neighbourhood, whereas the structured triangular lattice has five neighbours per neighbourhood and the unstructured lattice was found to have 5.1 neighbours per neighbourhood on average. Growth is more easily restrained when neighbourhoods are larger, because the number of potential intersections is higher.

For the three-dimensional system maximum growth occurs at a slightly lower value, $\rho_i = 0.064$, and the maximum change in density is 0.5, higher than for any of the two-dimensional systems. The explanation for this is that seeds in the two-dimensional systems only propagate in two directions, and, hence, only two intersections are required to halt their propagation. In the three-dimensional system, on the other hand, the seeds spread as planar surfaces, and many intersections are necessary to halt the propagation. As can be seen from the inset in Fig. 6(D), the final density of the cubic system is quite insensitive to the initial density over a large range of intermediate values. For all systems, the density curves seem to converge with increasing system size.

Some of the effects above are captured by a mean-field approximation of the propagation process, based on a difference equation formulation of the model (see Appendix B). The mean-field approximations for particular systems are shown as dashed lines in Fig. 6. It is clear that the approximation is poor for low ρ_i, which is not surprising, since the mean-field approximation relies on a homogeneous density field, and this assumption breaks down at low density (because active elements are mostly surrounded by inactive elements). One would expect the latter effect to be particularly pronounced in systems with few neighbours per neighbourhood. This is indeed observed in Fig. 6, where the fit at lower densities is better for the triangular than for the square and cubic systems.

The dotted black lines in Fig. 6(A)–(C) show a first-order approximation, as derived in Appendix C. This approximation assumes that any two seeds within distance t of a potential intersection point will cause an intersection after t iterations, ignoring the possibility that one or both seeds are intersected earlier by other elements. This approximation works well at low densities, where ignoring secondary interactions has the least effect, but also at high densities, where few seeds can

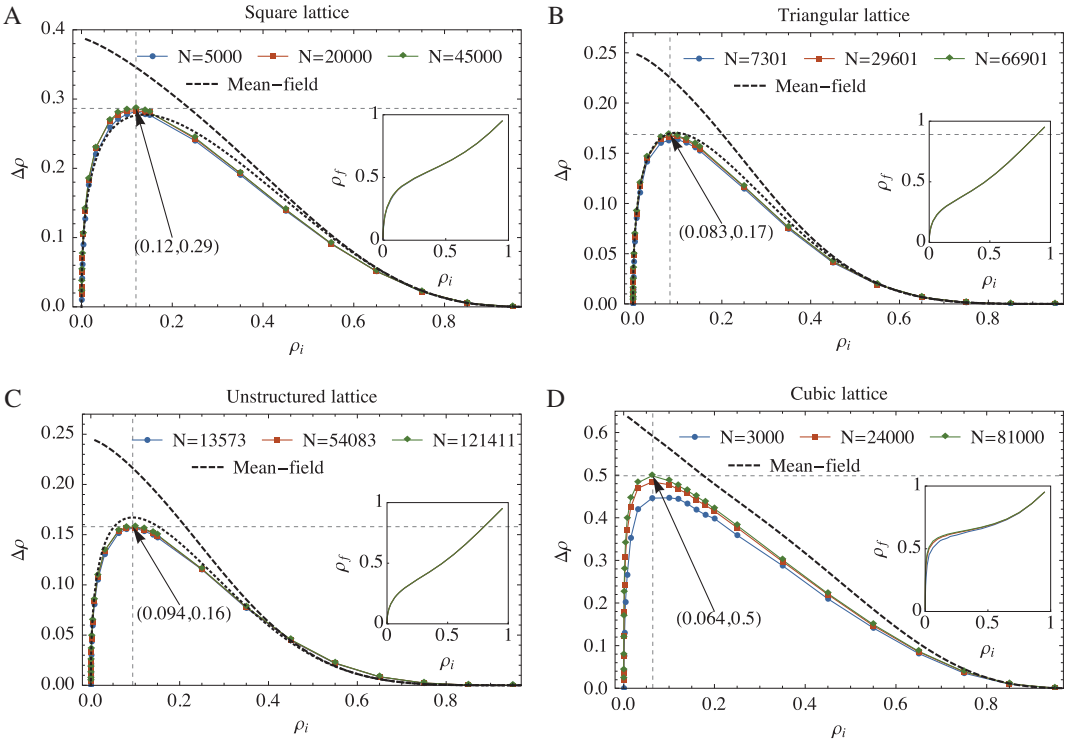

Fig. 6. Density change, $\Delta\rho$, as a function of initial density, ρ_i, for various system sizes, N. Dashed and dotted curves show mean-field and 1st-order approximations, respectively. Insets show the final density $\rho_f = \rho_i + \Delta\rho$ as a function of ρ_i. (A) Square lattice. (B) Regular triangular lattice. (C) Unstructured triangular lattice. (D) Cubic lattice.

propagate at all, and hence secondary intersections may safely be neglected. The first-order approximation is not applicable to three-dimensional systems, because propagation from a seed on a three-dimensional lattice is more difficult to stop, and planes may grow around each other.

3.2. Global growth rate

As shown in Fig. 7, it is found that the total growth rate $G(t)$ of a CAP system may be approximated by a function of the form

$$G(t) \propto \rho_i^{\alpha_T} e^{-t/\beta_T(\rho_i)}. \tag{1}$$

This is valid for intermediate values of ρ_i, when the initial density is sufficiently low, so that the final state is not dominated by the random initial condition, and when the system size is sufficiently large, so that seeds predominantly stop growing because of collisions with other active elements rather than with the system boundaries.

For the one- and two-dimensional systems it holds that $\alpha_T = 1.0$, and the growth is decreasing exponentially in time. β_T, which may be interpreted as the characteristic time scale of the growth process, is found to scale with ρ_i as $\beta_T \propto \rho_i^{-\tau}$, with $\tau \approx 1.0$ for the linear lattice, $\tau \approx 0.5$ for the square lattice, $\tau \approx 0.5$ for the triangular lattice and $\tau \approx 0.5$ for the unstructured lattice. For the cubic system we find $\alpha_T \approx 1.9$, which reflects the fact that the growth rate on such a lattice may increase initially before it reaches a peak and starts decaying. The characteristic time again scales as a power of ρ_i, this time with $\tau \approx 0.3$.

3.3. Growth of individual seeds

The change in density of a CAP system can be expressed as

$$\Delta\rho = \rho_i \langle S \rangle, \tag{2}$$

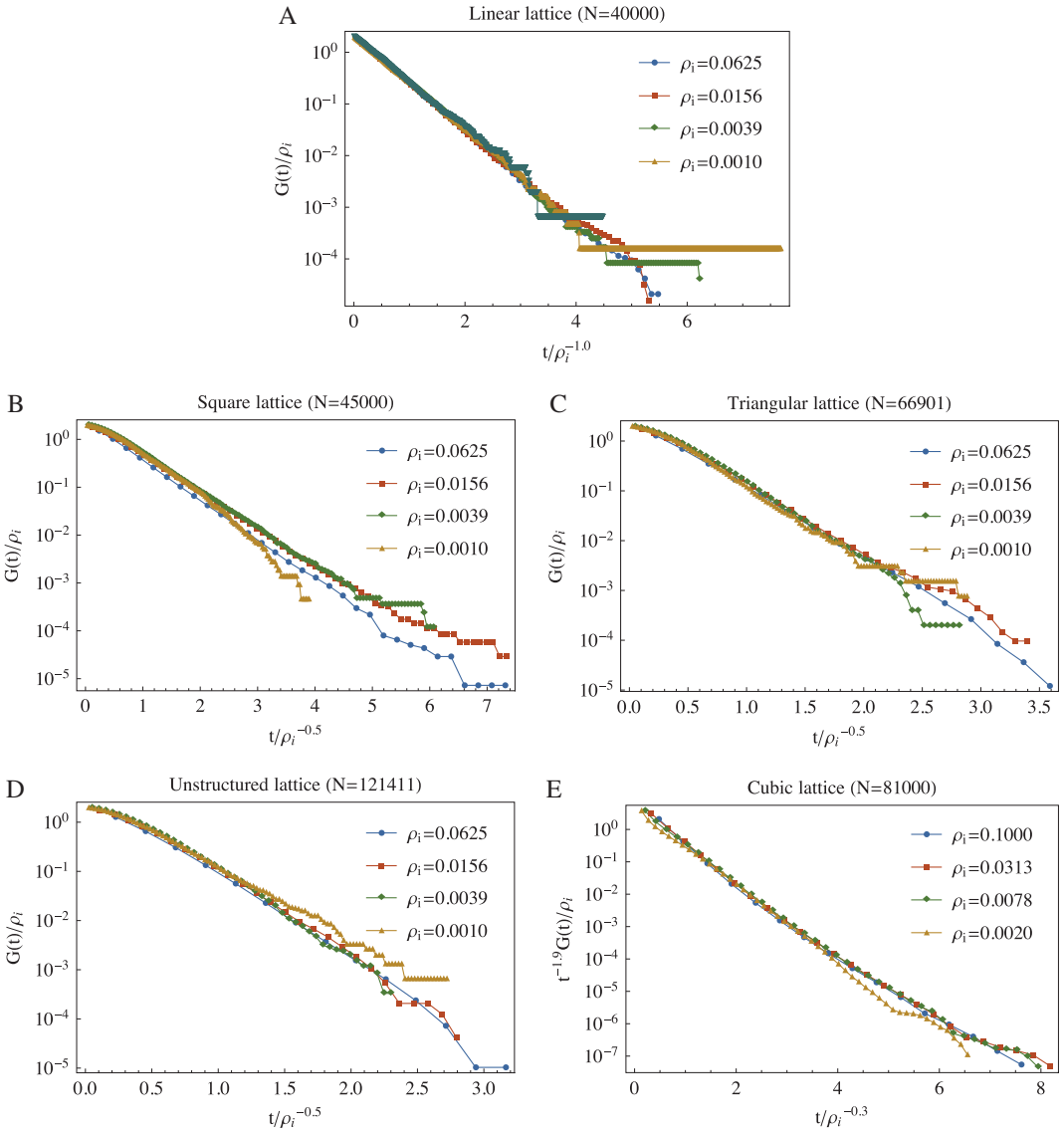

Fig. 7. Data collapse of the total growth rate G as a function of time, for various initial densities, ρ_i. The vertical axis is logarithmic and the horizontal axis is linear. (A) Linear lattice. (B) Square lattice. (C) Regular triangular lattice. (D) Unstructured triangular lattice. (E) Cubic lattice.

where $\langle S\rangle$ is the average number of elements that are activated by propagation from a given initial seed (an element may be activated simultaneously by more than one neighbour, so this is slightly modified at high ρ_i). We choose to refer to S as size. In addition to $\langle S\rangle$, which may be deduced from Fig. 7, it is also possible to measure the distribution of S for various initial densities and system sizes on the various lattices (Fig. 8). The distribution of S is well described by a gamma distribution, for all lattices. That is,

$$\gamma(S, \alpha_S, \beta_S) = \frac{1}{\beta_S^{\alpha_S}\Gamma(\alpha_S)} S^{\alpha_S - 1} e^{-(S/\beta_S)}, \tag{3}$$

where α_S is the shape parameter, β_S is the scale parameter and $\alpha_S\beta_S = \langle S\rangle$. Note that size, S, refers to a length for the one- and two-dimensional systems and an area for the three-dimensional system.

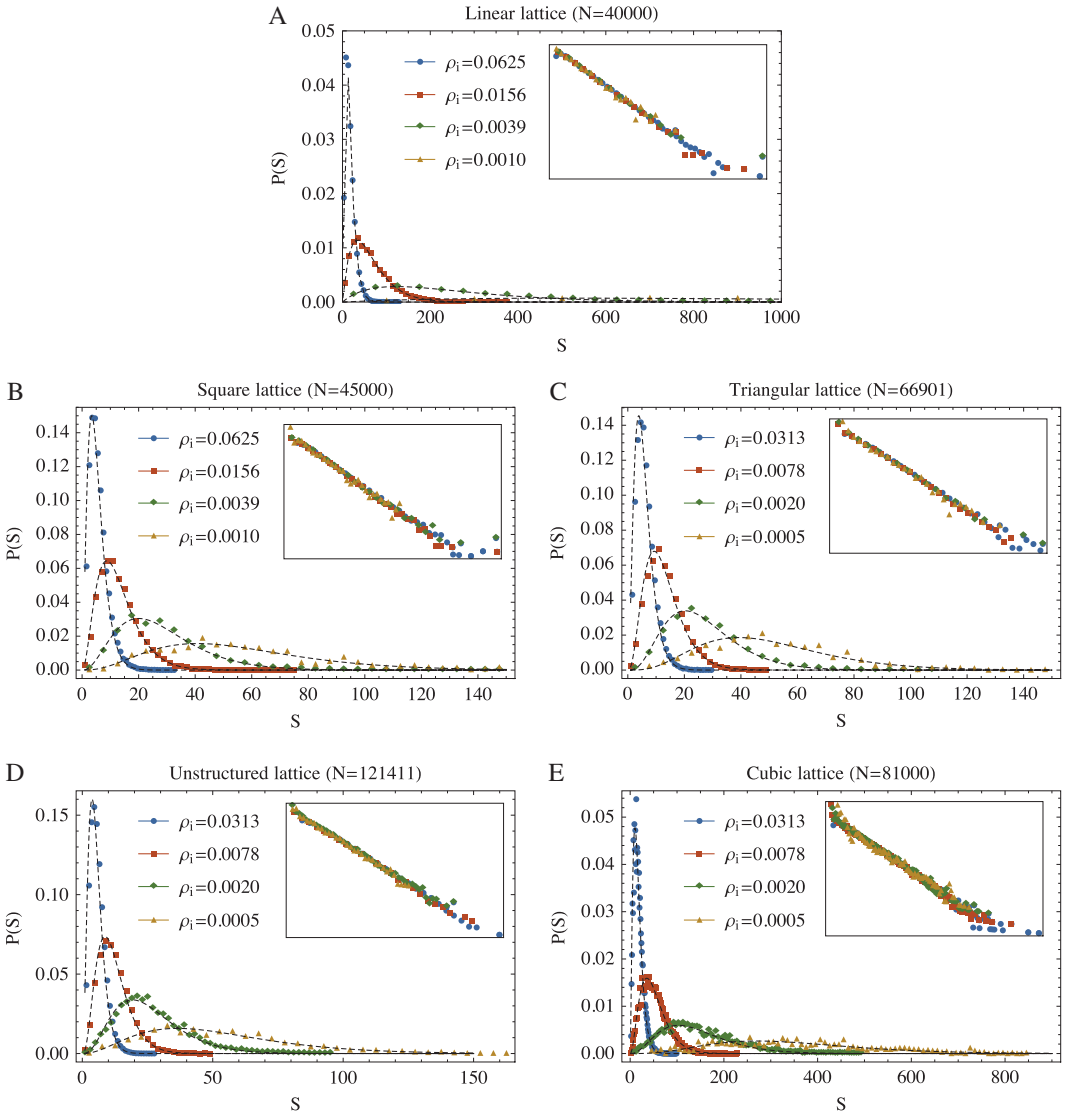

Fig. 8. Size distribution, S (number of elements activated from a seed), fitted to a gamma distribution $\gamma(S, \alpha_S, \beta_S) = S^{\alpha_S - 1} e^{-(S/\beta_S)} / \beta_S^{\alpha_S} \Gamma(\alpha_S)$. Insets show data collapse by plotting $\ln\left[S^{1-\alpha_S} P(S) \beta_S^{\alpha_S} \Gamma(\alpha_S)\right]$ vs. S/β_S. (A) Linear lattice. (B) Square lattice. (C) Regular triangular lattice. (D) Unstructured triangular lattice. (E) Cubic lattice.

For intermediate initial densities, we find that the scale parameter varies with ρ_i as $\beta_S \propto \rho_i^{-\sigma}$, where $\sigma = 1.0$ for the linear lattice, $\sigma = 0.5$ for the square lattice, $\sigma = 0.5$ for the triangular lattice, $\sigma = 0.5$ for the unstructured lattice and $\sigma = 0.7$ for the cubic lattice.

The shape parameter varies much less with ρ_i. We find $\alpha_S = 2.2\rho_i^{-0.0}$ for the linear lattice, $\alpha_S = 2.4\rho_i^{-0.1}$ for the square lattice, $\alpha_S = 2.5\rho_i^{-0.1}$ for the triangular lattice, $\alpha_S = 3.1\rho_i^{-0.0}$ for the unstructured lattice and $\alpha_S = 1.9\rho_i^{-0.1}$ for the cubic lattice. Note that since these exponents are very small, their estimation is associated with large errors.

Interestingly, the gamma distribution was previously found to describe the distribution of fracture lengths in a fragmentation model by Fortes and Andrade [18], which in some sense represents the continuum limit of the CAP model on two-dimensional lattices. Additionally, in Appendix C.1 we show analytically that the sizes in a one-dimensional CAP system are gamma distributed, with shape parameter $\alpha_S = 2$ and scale parameter $\beta_S = 2\rho_I^{-1}$.

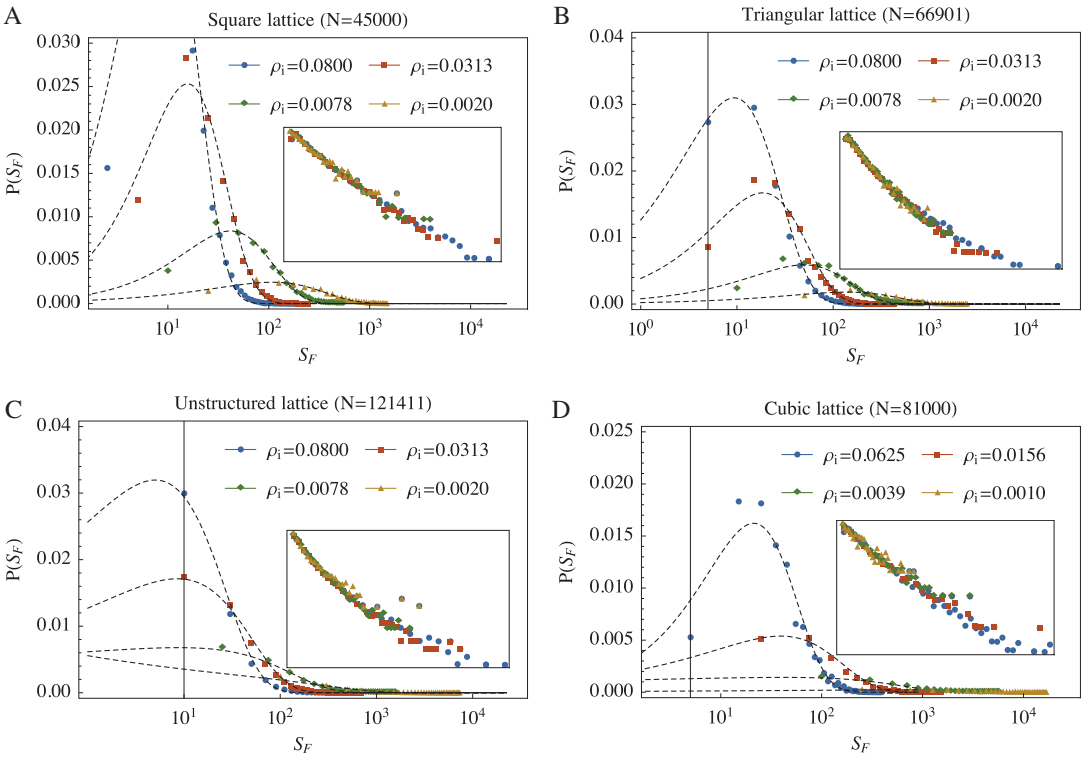

Fig. 9. Distribution of fragment sizes, S_F, fitted to a gamma distribution, i.e. $\gamma(S_F, \alpha_F, \beta_F) = S_F^{\alpha_F - 1} e^{-(S_F/\beta_F)} / \beta_F^{\alpha_F} \Gamma(\alpha_F)$. Insets show data collapse by plotting $\ln\left[S_F^{1-\alpha_F} P(S_F) \beta_F^{\alpha_F} \Gamma(\alpha_F)\right]$ vs. S_F/β_F. (A) Square lattice. (B) Regular triangular lattice. (C) Unstructured triangular lattice. (D) Cubic lattice.

3.4. Fragment size distribution

In the linear system, all elements will be activated before the growth terminates. However, in the two- and three-dimensional systems, some of the elements will generally remain inactive. The size of the fragments between active elements is found to be gamma distributed according to

$$\gamma(S_F, \alpha_F, \beta_F) = \frac{1}{\beta_F^{\alpha_F} \Gamma(\alpha_F)} S^{\alpha_F - 1} e^{-(S_F/\beta_F)}, \tag{4}$$

as shown in Fig. 9. Again, this is in accordance with the fragmentation model in Ref. [18], and interestingly the same distribution is reported for Voronoi cell sizes of Poisson distributed points in two and three dimensions by Ferenc and Néda [31].

For intermediate initial densities we find that the scale parameter varies with ρ_i as $\beta_F \propto \rho_i^{-\eta}$, where $\eta = 0.9$ for the square lattice, $\eta = 0.9$ for the triangular lattice, $\eta = 0.9$ for the unstructured lattice and $\eta = 1.1$ for the cubic lattice.

Just as we found for the size distribution in the previous section, the shape parameter of the fragment distribution varies little with ρ_i. We find $\alpha_F = 2.9\rho_i^{-0.1}$ for the square lattice, $\alpha_F = 2.4\rho_i^{-0.0}$ for the triangular lattice, $\alpha_F = 2.1\rho_i^{-0.1}$ for the unstructured lattice and $\alpha_F = 1.6\rho_i^{-0.0}$ for the cubic lattice. Note that since these exponents are very small their estimation is associated with large errors.

3.5. Percolation

The CAP systems studied here are similar to bond-percolation systems, with the important distinction that the former evolve from the initially random configuration according to a certain rule. The dynamic nature of the CAP model is a feature shared with invasion percolation (IP) systems [14], and one could think of the CAP model as a special case of an IP system with a particular invasion rule. Since propagation continues until contact, percolation is always achieved in CAP systems, so, when defined in terms of ρ_i, the percolation threshold is 0. Yet, the way in which percolation is reached will depend on the

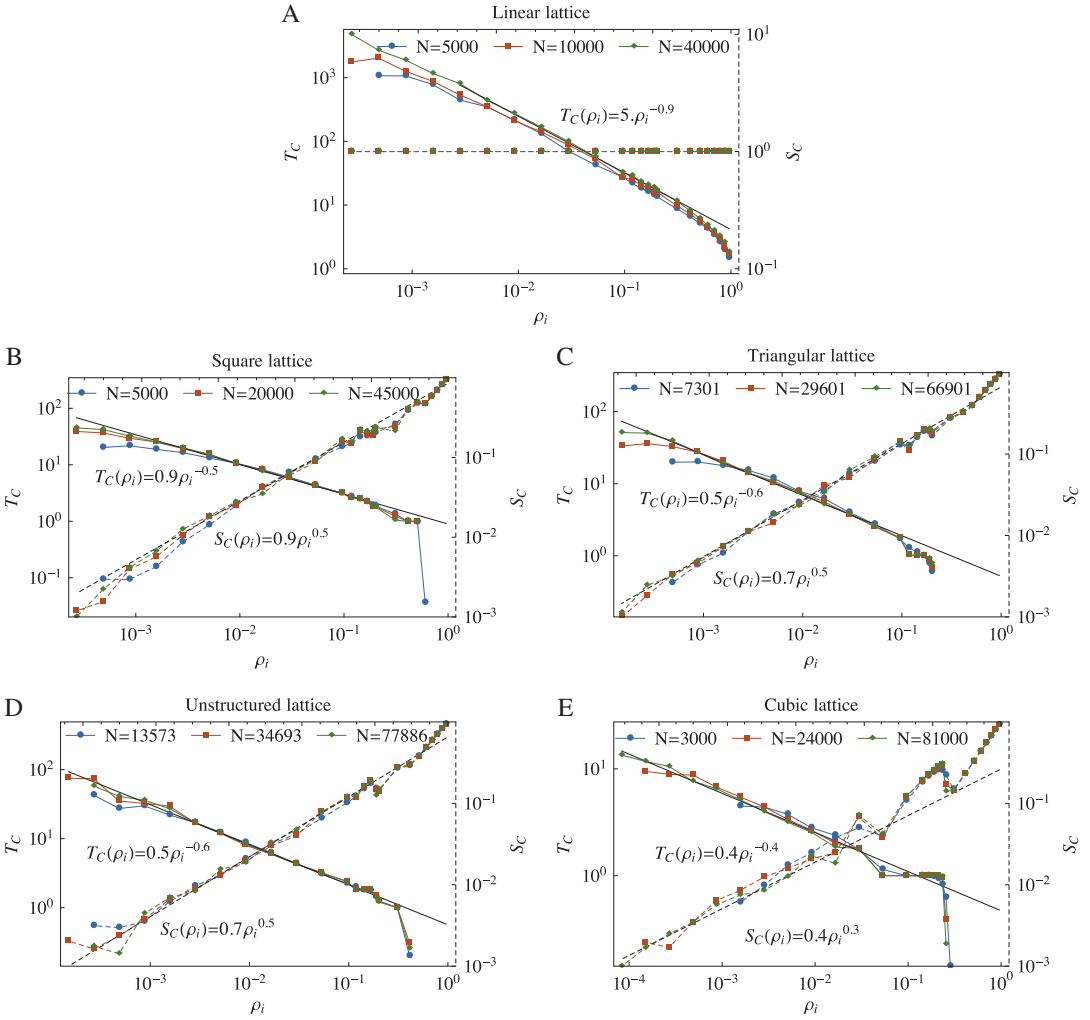

Fig. 10. Time to percolation, T_C, and size of the percolating cluster at the time of nucleation, S_C, as a function of initial density, ρ_i, for various system sizes, N. Note that percolation was measured in one direction, i.e. it was tested if two opposite sides of the system were connected by a path of active elements. (A) Linear lattice. (B) square lattice. (C) Regular triangular lattice. (D) Unstructured triangular lattice. (E) Cubic lattice.

initial density and may be quantified. The time to percolation in the CAP model is somewhat analogous to the concept of a breakthrough time in IP systems, i.e. the time it takes for an invading fluid to form a continuous path connecting an inlet to an outlet. Here, however, we define percolation in analogy to conventional site or bond percolation models, as the existence of a connected path between two opposing external boundaries in the system.

If the density of initial seeds, ρ_i, is equal to or higher than the percolation threshold of the underlying lattice, percolation trivially occurs after 0 iterations and the percolating cluster will look like the percolating cluster in a normal percolation system. If the initial density is lower than the percolating threshold of the underlying lattice, percolation will only be reached after a sufficient number of intersections. Fig. 10 shows the time (i.e. number of iterations) to percolation, T_C, vs. ρ_i (full lines) and the relative size of the percolating cluster at the time of percolation (normalised by the system size), S_C, vs. ρ_i (dashed lines).

At high initial densities, when percolation exists in the initial conditions, $T_C = 0$ and $S_c \approx \rho_i$ for all systems. This is because the initial network is highly connected, so that most active elements form part of the percolating cluster. Note that for the linear system, the percolation cluster always includes every element of the system, i.e. $S_C = 1$.

For the two- and three-dimensional systems we observe irregularities in the plots of S_C. When ρ_i falls slightly below the percolation threshold, a sharp transition can be seen: in this situation only a few more seeds need to be activated in

Table 1
Summary of scaling exponents for scaling with ρ_i obtained for various lattices. For the one-dimensional system, analytic exponents are included in brackets.

	Linear	Square	Triangular	Unstructured	Cubic
Characteristic time (τ)	1.0 (1)	0.5	0.5	0.5	0.3
Characteristic size (σ)	1.0 (1)	0.5	0.5	0.5	0.7
Characteristic fragment size (η)	–	0.9	0.9	0.9	1.1
Time to percolation (μ)	1.0 (1)	0.5	0.6	0.6	0.4
Percolating cluster size (ν)	–	0.5	0.5	0.5	0.3

order to achieve percolation. However, propagation is executed in parallel, and during the first iteration more seeds will be activated than required to reach percolation. This explains the discontinuities in S_c coinciding with the density where $T_c \to 0$ in Fig. 10. Similar transitions occur as ρ_i is reduced further and the number of iterations to percolation increases. For the two-dimensional systems the first two transitions are apparent in Fig. 10(B)–(D). For the three-dimensional system the transitions are more pronounced, and we recognise three of them in Fig. 10(E). One could avoid the irregularities in the S_C curves for high ρ_i by updating elements sequentially instead of synchronously at each iteration. Percolation could then be reached before all sites have been updated, thereby reducing the number of redundant activations. To do this, one could either assign an order to the seeds (which may require some motivation), or, alternatively, the update sequence could be chosen randomly at each iteration. Schönfisch and de Roos [29] note that correlations in the update sequence of cellular automata typically lead to artefacts, suggesting that random update sequence may be preferred.

For intermediate values of ρ_i, T_C is seen to follow a power law, according to $T_C \propto \rho_i^{-\mu}$. For the linear lattice $\mu = 0.9$, for the square lattice $\mu = 0.5$, for the triangular lattice $\mu = 0.6$, for the unstructured lattice $\mu = 0.6$ and for the cubic lattice $\mu = 0.4$. Similarly, $S_C \propto \rho_i^{\nu}$ for intermediate values of ρ_i, with $\nu = 0.5$ for the square lattice, $\nu = 0.5$ for the triangular lattice, $\nu = 0.5$ for the unstructured lattice and $\nu = 0.3$ for the cubic lattice.

For low ρ_i, finite size effects play a role, and both S_C and T_C deviate from the power law scaling. In the one-dimensional case the time to percolation may be found analytically to scale as $T_C \approx \frac{\log N}{2}\rho_i^{-1}$ for low densities, and, although the pre-factor is size-dependent, the exponent $\mu = -1$ is found to survive in the infinite size limit (see Appendix C.1).

4. Discussion and conclusions

4.1. Universal features of the CAP model

In the previous section, we found that the CAP model evolves in a similar way on the various lattices considered. This evolution is governed by a trade off between the number of initial seeds and to what extent these initial seeds are able to propagate. A consequence of this is the existence of an optimal initial density ρ_i, for which the change in density is maximised. Our mean-field (Appendix B) and first-order (Appendix C) approximations suggest that the exact form of the density evolution curve depends on lattice connectivity, which we also observe.

The scaling exponents obtained for the various properties measured in the previous section are summarised in Table 1. From this table we recognise certain patterns. The characteristic time and size, scale with similar exponents for all the two-dimensional systems. This indicates that the particular lattice connectivity has little effect on the characteristic time and size.

The fact that the characteristic time and size for two-dimensional systems scale with approximately the same exponents is not surprising: the size has units of length for the two-dimensional system, and the scale parameter β_S may be thought of as a *'mean free path'*. Since propagation in the CAP model happens at constant speed, the characteristic time must scale with the same exponent. For the three-dimensional system, the size, S, refers to an area, and β_S could be considered as a *'mean free area'*, with units of square length. This suggests that the exponents for characteristic time and size should differ by a factor of 2, as observed.

As pointed out in Sections 3.3–3.4, the observation that both the size and fragment size follow gamma distributions is a feature shared with fragmentation models [18] and Voronoi cell size distributions of random packings [31]. We also derived the gamma distribution analytically for the size distribution of the linear system (Appendix C.1). This suggests that the form of the distributions is insensitive to the details of the model, and not a unique feature of CAP systems. We observe that the fragment size distributions scale similarly with ρ_i across the various two-dimensional systems and with a slightly lower exponent for the three-dimensional system.

We note that, in the large system limit, the time to percolation in the CAP model is a quantity that is independent of system size. This differs from the breakthrough time typically measured in invasion percolation systems, which would depend on the particular placement of inlets and outlets. The time to percolation scales with approximately the same exponent as the characteristic time for all systems. This means that after rescaling to characteristic units the time to percolation is independent of initial density. In invasion percolation models, evolution is typically stopped once breakthrough is achieved and a flow path has been established. In this sense, invasion percolation systems are percolation systems that automatically settle at the critical point of the system [14]. The CAP model could be regarded in the same way if evolution is stopped at the time of percolation.

For the two-dimensional systems, the size of the percolating cluster at the time of percolation scales with ρ_i as the inverse of the characteristic size. For the three-dimensional system, however, the size of the percolating cluster scales with approximately half the negative exponent of the characteristic size. This could reflect the topology of the three-dimensional lattice, which makes it relatively easier to create a percolating path, because the percolating cluster is not confined to a plane. With regard to the one-dimensional system we note that the time to percolation is size-dependent and scales as $\log N$ (Appendix C.1). This is a consequence of the fact that every element must be activated in order for percolation to occur in one dimension. When the system is larger, the probability of having large gaps in the initial condition is increased, and in one dimension this implies that T_C must increase. In higher dimensions, the connectivity of the lattice provides more potential percolation paths, and the existence of large gaps locally in a large system should not affect percolation globally.

We note that τ and μ are close to $1/1$, $1/2$ and $1/3$ for the one-, two- and three-dimensional systems, respectively. Similarly, the exponents for σ are respectively close to $1/1$, $1/2$ and $2/3$. The denominators correlate to the dimensionality of the lattices, leading one to question whether the deviations are due to error in measurement or finite size effects. In any regard, it is clear that the various scaling exponents primarily depend on dimensionality, whereas the scaling properties are relatively insensitive to lattice connectivity among the two-dimensional systems. This is a sign of universality in the CAP model, similarly to that found in percolation models [10], and it suggests that the CAP model may also be useful for modelling continuous processes.

4.2. Applications of the CAP model

The CAP model is both simple and general. It works on arbitrary networks, and it is not constrained to lattices, as presented here. However, the lattice representations we have considered are particularly simple and already suggest many potential applications of the model. As we have shown, the model may be set up to closely emulate certain kinds of fracturing processes, where active elements are interpreted as fracture segments which propagate until meeting other fractures. In the three-dimensional version, elements are not allowed to intersect, but planes may still grow around each other, capturing an important feature of three-dimensional fracturing processes. Although this is a crude approximation, with all fractures propagating at constant speed along predefined directions, the use of such a model could be manyfold. For example, coalescence of propagating micro cracks is an important mechanism for failure in rock subject to compressional load [32], and is, for instance, observed in borehole breakouts [33]. Analysing the generic properties of the CAP model in this context may provide insight into how failure is reached. Additionally, the CAP model may be applicable to fragmentation processes, and as noted earlier, we already found that the fragment size distributions obtained with the CAP model are consistent with previous fragmentation models, such as [18]. Fracture formation due to pressure accumulation when kerogen is converted to lighter hydrocarbons is believed to play an important role in the migration of oil and gas in source rock. In laboratory experiments, where pieces of shale were heated to induce conversion of organic material, fractures were observed to emanate from kerogen grains [34]. The CAP approach could be adopted as a model to simulate the propagation of such fractures, if the driving (i.e kerogen conversion) is assumed to happen at the same rate in each grain.

Even if the CAP model is not considered to mimic any particular fracturing process, the model may be used to generate artificial fracture networks and used as input to discrete fracture network models. Such artificial networks are used, for example, in reservoir modelling and hydrogeology [15,35,36]. For the purpose of such applications, the fully evolved CAP systems would provide an upper bound for the connectivity of a fracture set, and it might be more relevant to stop the evolution before the network is fully developed. For example it could be more realistic, in some applications, to use CAP networks that are at, or close to, the percolation threshold.

An alternative to considering active elements as forming a fracture network would be to consider the background network as a pre-existing fracture system. The evolution of the CAP model could then be regarded as a kind of invasion percolation process on this background. In fact, the prevention of invasion into perpendicular fractures (i.e. preferential propagation along straight paths) could be motivated by consideration of capillary effects, as argued by Wettstein et al. [37] in an invasion percolation model formulated on discrete fracture networks. Our CAP model could possibly be adapted to simulate fluid invasion processes of this type, as a simplified alternative to the latter model.

The scope of the CAP model may be extended further by coupling it to other models on the same lattice. For example, when applied to fracture systems, such as the gelatine experiments in Ref. [28], the propagation of a fracture may depend on the supply of fluids that drive the fracturing, and the fluid transport can be modelled using a finite element or finite difference scheme on the underlying lattice.

The conditioning of element propagation on external fields also suggests a range of other applications. Transport of melt water from glaciers is hypothesised to occur by channel formation, depending on local water supply, landscape form and ice thickness [38]. Channel formation may be thought of as a CAP process, in which the fracture propagation is driven by the prevailing water and ice pressure. Further, coupling a water infiltration model with a crack formation model would allow for an enhanced simulation of soil water flow, because drying-cracks, for instance, are known to significantly influence this process [39,40]. The explicit coupling of these processes has received limited attention, largely because crack formation is an inherently discrete process, whereas most infiltration models are continuous in nature (i.e. Richards equation) [41]. Similarly, the CAP model could be adjusted to simulate the growth of fungi, which evolve into a network of individual hyphae. The elongation of the latter is largely driven by the internal substrate concentration, which could be accounted for by extending the current CAP model [42].

The above topics are only a few suggestions that the authors will explore with collaborators in future publications. Given its simplicity, flexibility and scalability we believe that there may be many more applications of the CAP model, and we encourage other researchers to explore how it may be used in their field of research.

Acknowledgements

The presented model was developed in collaboration with Dr. Stephen Wolfram at the Wolfram Science Summer School 2013. The first author wishes to thank Dr. Stephen Wolfram, Dr. Todd Rowland and the rest of the summer school staff from Wolfram Research for their assistance, advice and encouragement. He further wishes to thank Dr. Luiza Angheluta, Prof. Jens Feder and Prof. Paul Meakin for useful discussions and suggestions.

The authors also acknowledge support by the Petromaks program of the Norwegian Research Council (grant number 193186/E30). This study was supported by a Center of Excellence grant from the Norwegian Research Council to the Physics of Geological Processes Center (PGP) (grant number 142042).

Appendix A. Implementation of the CAP model

The CAP model is conveniently and efficiently implemented as a substitution system. Starting from a list $A \subset E$ of initially active elements (“seeds”), one replaces every element $e \in A$ at each iteration by the list of neighbouring elements that they activate. When no more substitutions are possible, the evolution terminates, and we may say that the system has reached steady state.

The substitution algorithm is completely background-independent and is effectively accomplished by repeatedly applying the following single line of Mathematica code:

```
Union@Select[Flatten[nbs[[A]],1],Nor@@S[[#]]&][[All,1]]
```

Here S is the vector of element states, $\{s_1, s_2, \ldots\}$, and `nbs` is the list of element neighbourhoods, $\{\{N_1^1, N_1^2, \ldots\}, \{N_2^1, N_2^2, \ldots\}, \ldots\}$.

For simplicity, we may divide the above function into algorithmic steps:

1. The part `Flatten[nbs[[A]],1]` extracts all the neighbourhoods whose first element may possibly be activated in the current iteration.
2. Those neighbourhoods whose first element will actually be activated are found using `Select`, with selection criterion `Nor@@S[[#]]&`. The latter only yields true if none of the elements in the particular neighbourhood are already active.
3. Only the first element of each neighbourhood is activated, and these are extracted by `[[All,1]]`.
4. Elements may be activated by more than one neighbour simultaneously. `Union` is applied to eliminate duplicates. (This may be dropped, but it yields large computational speed-ups for certain systems, depending on the network connectivity.)

Appendix B. Mean-field approximation

If an element is active in the final configuration of the system it means that it was either an initial seed, or it was activated at one of the subsequent iterations. Let P_e^t and $SP_e^t = 1 - \sum_{t'=0}^{t} P_e^{t'}$ be, respectively, the probability that an element e is activated at iteration t or has survived (i.e. not been activated) until iteration t. The probability that element e is activated at iteration t can then be expressed as

$$P_e^t = SP_e^{t-1}\left(1 - \prod_{i=1}^{|N_e|}\left(1 - P_{n_e^{i,1}}^{t-1}\prod_{j=2}^{|N_e^i|} SP_{n_e^{i,j}}\right)\right). \tag{B.1}$$

Here, the multiplication by SP_e^{t-1} checks that the element has not already been activated before iteration t. The contents of the outer brackets measure the probability that the element will be activated by at least one of its neighbours in the current iteration. This equals the negation of “no neighbour will activate the element in the current iteration”. The activation by each neighbourhood may happen independently, accounting for the outermost product. A neighbour $n^{i,1}$ can only activate element e if it was itself activated in the previous iteration and if the remaining neighbours in neighbourhood i are inactive. This is accounted for by the expression in the innermost brackets.

We may simplify Eq. (B.1) if we assume that the number of neighbourhoods per element, $|N_e| = r$, and the number of neighbours per neighbourhood, $|N_e^i| = q$, are constant and equal for all elements. If we furthermore assume that every element is equal, we can approximate the above formula with

$$P_e^t = SP_e^{t-1}\left(1 - \left(1 - P_e^{t-1}(SP_e^{t-1})^q\right)^r\right). \tag{B.2}$$

By assuming $P_e^0 = \rho_i$, the final density of the system is then approximated by

$$\rho_f \approx 1 - SP_e^{\infty}. \tag{B.3}$$

In practice, the latter infinite sum may be cut off at a finite number of iterations, as P_e^t decreases rapidly with t.

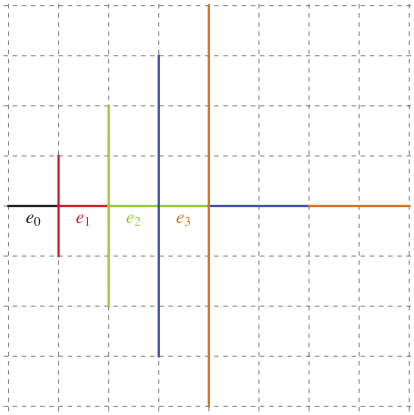

Fig. C.11. Illustration of the first order scheme on a square lattice ($q = 3$). We consider how the rightward propagation of the black seed element, e_1, may be intersected if we ignore secondary intersections. With this assumption, e_0, can only activate e_1 in the first iteration if none of the red elements are seeds. If e_1 was activated by e_0 in the first iteration, e_1 can activate e_2 in the second iteration if none of the green elements were seeds. In the same way the activation of e_2 depends on the activation of e_1 in the previous step and on the state of the blue elements at the beginning of the simulation. The activation of e_3 is further influenced by the orange elements etc. (For interpretation of the references to colour in this figure legend, the reader is referred to the web version of this article.)

Appendix C. First-order approximation

We wish to approximate the density evolution of a two-dimensional CAP system. To this end, we note that at iteration t an intersection may only happen at a particular point if there is more than one initial seed within distance t from that point. As a first-order approximation, we will assume that any two seeds within distance t of a point will lead to intersection at that point (i.e ignore secondary intersections).

Consider propagation in a particular direction from an initial seed on a two-dimensional lattice and suppose for simplicity that every element has q neighbours per neighbourhood. The probability for propagation to proceed at least one step is

$$P(t \geq 1) = (1 - \rho_i)^q. \tag{C.1}$$

Whether propagation proceeds one more step is influenced by elements within distance two of the current endpoint, as illustrated in Fig. C.11. In general we have

$$P(t \geq 2) = P(t \geq 1)(1 - \rho_i)^{2q} = (1 - \rho_i)^{3q}. \tag{C.2}$$

As illustrated in Fig. C.11 the subsequent steps will be influenced by $t(q - 1) + 2$ additional elements, where t is the number of the iteration. In general we therefore have

$$P(t \geq t') = P(t \geq t' - 1)(1 - \rho_i)^{t'(q-1)+2} = (1 - \rho_i)^{\frac{q-1}{2}t'^2 + \frac{q+3}{2}t' - 1}. \tag{C.3}$$

The probability hat propagation stops after exactly t' iterations is therefore

$$\begin{aligned} P(t') &= P(t \geq t') - P(t \geq t' + 1) \\ &= (1 - \rho_i)^{\frac{q-1}{2}t'^2 + \frac{q+3}{2}t' - 1} - (1 - \rho_i)^{\frac{q-1}{2}(t+1)'^2 + \frac{q+3}{2}(t'+1) - 1} \\ &= (1 - (1 - \rho_i)^{1+q+(q-1)t'})(1 - \rho_i)^{\frac{q-1}{2}t'^2 + \frac{q+3}{2}t' - 1}. \end{aligned} \tag{C.4}$$

Since every seed in two dimensions can propagate in two directions, the change in density of the entire system may be approximated as

$$\Delta\rho = 2\rho_i\langle t\rangle = 2\rho_i \sum_{t=1}^{\infty} tP(t). \tag{C.5}$$

A closed form of Eq. (C.5) has not been found. In practice, for finite ρ_i the sequence is well approximated numerically by truncating the summation at $i_{\max} \gg \rho^- 1$.

C.1. One-dimensional CAP systems

A one dimensional CAP system may be thought of as a particular case of a two-dimensional model, with only one neighbour per neighbourhood, i.e. $q = 1$. In this case, the first-order approximation derived above is exact, because secondary interactions are impossible. Thus, for a one-dimensional system,

$$P(t) = (2 - \rho_i)\rho_i(1 - \rho_i)^{2t-1}. \tag{C.6}$$

Since every seed in the one-dimensional system can grow in two directions the distribution of sizes, S, may be found by summing up all combinations of propagation to the left and to the right that in total yield a length S, i.e.

$$\begin{aligned} P_S(S) &= \sum_{t=0}^{S} P(S-t)P(t) \\ &= \sum_{t=0}^{S} (2-\rho_i)\rho_i(1-\rho_i)^{2(S-t)-1}(2-\rho_i)\rho_i(1-\rho_i)^{2t-1} \\ &= (2-\rho_i)^2\rho_i^2 S(1-\rho_i)^{2S-2}. \end{aligned} \tag{C.7}$$

Note that $(1 - \rho_i)^{2S} = e^{2S\log(1-\rho)}$, and furthermore, for small ρ_i, $\log(1 - \rho_i) \approx -\rho_i$. Hence, for small ρ_i, Eq. (C.7) is a gamma distribution of the form

$$P_S(S) \propto S^{\alpha_S - 1}e^{-S/\beta_S}, \tag{C.8}$$

with shape parameter $\alpha_S = 2$ and scale parameter $\beta_S = 1/2\rho_i$. Note that $\langle S\rangle = \alpha_S\beta_S = \rho_i^{-1}$, as it should be; for a one-dimensional system with N elements and initial density ρ_i, the number of initial seeds is $N\rho_i$. The system will only terminate once every element is active, hence the number of elements activated per seed is $N/N\rho_i = \rho_i^{-1}$.

For one-dimensional systems, percolation is reached at the moment when the propagation of the last seed is arrested. The time to percolation, T_C can therefore be approximated from the relation

$$N\rho_i \sum_{t=T_C}^{\infty} P(t) = 1, \tag{C.9}$$

i.e. only one fracture survives until T_c or later. After inserting Eq. (C.6), evaluating the sum and solving for T_C, one obtains

$$T_C = \frac{1}{2}\left(1 - \frac{\log(N\rho_i)}{\log(1-\rho_i)}\right). \tag{C.10}$$

To first order in ρ_i,

$$T_C \approx \frac{\log N}{2}\rho_i^{-1}. \tag{C.11}$$

On a log – log plot, the slope of $\log T_C$ vs. $\log \rho_i$ is given by

$$\begin{aligned} \mu &= \frac{\partial(\log T_C)}{\partial(\log \rho_i)} \\ &= \frac{1}{1-\rho_i}\left(\frac{1}{\log(1-\rho_i) - \log(N\rho_i)} - \frac{\rho_i}{\log(1-\rho_i)}\right) \\ &\underset{N\to\infty}{=} \frac{\rho_i}{(\rho_i - 1)\log(1-\rho_i)} \\ &\underset{\rho_i\to 0}{=} -1. \end{aligned} \tag{C.12}$$

Eqs. (C.11) and (C.12) show that the time to percolation scales with the inverse of ρ_i in the low density limit. T_C also increases logarithmically with system size, N, but the inverse scaling in ρ_i persists in the large size limit.

References

[1] J.R. Banavar, A. Maritan, A. Rinaldo, Size and form in efficient transportation networks, Nature 399 (1999) 130–132.
[2] A. Rinaldo, J.R. Banavar, V. Colizza, A. Maritan, On network form and function, Physica A 340 (2004) 749–755.
[3] S. Kramer, M. Marder, Evolution of river networks, Phys. Rev. Lett. 68 (1992) 205.
[4] H. Takayasu, H. Inaoka, New type of self-organized criticality in a model of erosion, Phys. Rev. Lett. 68 (1992) 966–969.
[5] R.L. Leheny, S.R. Nagel, Model for the evolution of river networks, Phys. Rev. Lett. 71 (1993) 1470.
[6] L.B. Leopold, W.B. Langbein, The Concept of Entropy in Landscape Evolution, US Government Printing Office Washington, DC, 1962.
[7] P. Meakin, J. Feder, T. Jøssang, Simple statistical models for river networks, Physica A 176 (1991) 409–429.

[8] P. Meakin, Formation of fractal clusters and networks by irreversible diffusion-limited aggregation, Phys. Rev. Lett. 51 (1983) 1119.
[9] J.G. Masek, D.L. Turcotte, A diffusion-limited aggregation model for the evolution of drainage networks, Earth Planet. Sci. Lett. 119 (1993) 379–386.
[10] D. Stauffer, A. Aharony, Introduction to Percolation Theory, Taylor & Francis, London and Bristol, PA, 1994.
[11] M. Sahimi, Applications of Percolation Theory, Taylor & Francis, London, 1994.
[12] A. Aharony, E.L. Hinrichsen, A. Hansen, J. Feder, H. Hardy, et al., Effective renormalization group algorithm for transport in oil reservoirs, Physica A 177 (1991) 260–266.
[13] S. Kirkpatrick, Percolation and conduction, Rev. Mod. Phys. 45 (1973) 574.
[14] D. Wilkinson, J.F. Willemsen, Invasion percolation: a new form of percolation theory, J. Phys. A: Math. Gen. 16 (1983) 3365.
[15] P.M. Adler, J.-F. Thovert, Fractures and Fracture Networks, vol. 15, Springer, 1999.
[16] S.J. Steacy, C.G. Sammis, An automaton for fractal patterns of fragmentation, Nature 353 (1991) 250–252.
[17] G. Hernández, H.J. Herrmann, Discrete models for two-and three-dimensional fragmentation, Physica A 215 (1995) 420–430.
[18] M. Fortes, P. Andrade, A model of fragmentation by nonintersecting cracks, J. Appl. Phys. 64 (1988) 5157–5160.
[19] R. Korsnes, S. Souza, R. Donangelo, A. Hansen, M. Paczuski, K. Sneppen, Scaling in fracture and refreezing of sea ice, Physica A 331 (2004) 291–296.
[20] K. Iyer, B. Jamtveit, J. Mathiesen, A. Malthe-Sørenssen, J. Feder, Reaction-assisted hierarchical fracturing during serpentinization, Earth Planet. Sci. Lett. 267 (2008) 503–516.
[21] P. Erdös, A. Rényi, On random graphs i, Publ. Math. Debrecen 6 (1959) 290–297.
[22] R. Albert, A.-L. Barabási, Statistical mechanics of complex networks, Rev. Mod. Phys. 74 (2002) 47.
[23] A.-L. Barabási, R. Albert, Emergence of scaling in random networks, Science 286 (1999) 509–512.
[24] D.J. Watts, S.H. Strogatz, Collective dynamics of small-world networks, Nature 393 (1998) 440–442.
[25] S. Wolfram, A New Kind of Science, Wolfram Media, Inc., Champaign, IL, 2002.
[26] K.L. Morrow, T. Rowland, C.M. Danforth, Dynamic structure of networks updated according to simple, local rules, Phys. Rev. E 80 (2009) 016103.
[27] R. Southwell, J. Huang, C. Cannings, Complex networks from simple rules, Complex Syst. 22 (2013) 151–173.
[28] M. Kobchenko, A. Hafver, E. Jettestuen, O. Galland, F. Renard, P. Meakin, B. Jamtveit, D.K. Dysthe, Drainage fracture networks in elastic solids with internal fluid generation, Europhys. Lett. 102 (2013) 66002–66008.
[29] B. Schönfisch, A. de Roos, Synchronous and asynchronous updating in cellular automata, BioSystems 51 (1999) 123–143.
[30] S. Bandini, A. Bonomi, G. Vizzari, What do we mean by asynchronous ca? A reflection on types and effects of asynchronicity, in: Cellular Automata, Springer, 2010, pp. 385–394.
[31] J.-S. Ferenc, Z. Néda, On the size distribution of Poisson voronoi cells, Physica A 385 (2007) 518–526.
[32] R.L. Kranz, Microcracks in rocks: a review, Tectonophysics 100 (1983) 449–480.
[33] W. Du, J. Kemeny, Modeling borehole breakout by mixed mode crack growth, interaction, and coalescence, Int. J. Rock Mech. Min. Sci. Geomech. Abstr. 30 (1993) 809–812.
[34] M. Kobchenko, H. Panahi, F. Renard, D.K. Dysthe, A. Malthe-Sørenssen, A. Mazzini, J. Scheibert, B. Jamtveit, P. Meakin, 4d imaging of fracturing in organic-rich shales during heating, J. Geophys. Res.: Solid Earth 116 (2011) 1978–2012.
[35] M. Karimi-Fard, L. Durlofsky, K. Aziz, et al., An efficient discrete-fracture model applicable for general-purpose reservoir simulators, SPE J. 9 (2004) 227–236.
[36] L. Hartley, D. Roberts, Summary of Discrete Fracture Network Modelling as Applied to Hydrogeology of the Forsmark and Laxemar Sites, Technical Report, Swedish Nuclear Fuel and Waste Management Co., 2013.
[37] S.J. Wettstein, F.K. Wittel, N.A. Araújo, B. Lanyon, H.J. Herrmann, From invasion percolation to flow in rock fracture networks, Physica A 391 (2012) 264–277.
[38] C. Schoof, Ice-sheet acceleration driven by melt supply variability, Nature 468 (2010) 803–806.
[39] H. Peron, L. Laloui, L.-B. Hu, T. Hueckel, Formation of drying crack patterns in soils: a deterministic approach, Acta Geotech. (2013) 1–7.
[40] V. Novak, J. Šimůnek, M.T.v. Genuchten, Infiltration of water into soil with cracks, J. Irrig. Drain. Eng. 126 (2000) 41–47.
[41] T. Furst, R. Vodak, M. Bil, et al., On the incompatibility of richards' equation and finger-like infiltration in unsaturated homogeneous porous media, Water Resour. Res. (2009) 2009.
[42] G.P. Boswell, H. Jacobs, F.A. Davidson, G.M. Gadd, K. Ritz, Growth and function of fungal mycelia in heterogeneous environments, Bull. Math. Biol. 65 (2003) 447–477.

Paper IV:

Modelling fracturing-assisted drainage of fluids from a solid

A. Hafver, J.M. Baetens, E. Jettestuen, D.K. Dysthe, P. Meakin and A. Malthe-Sørenssen

Manuscript in revision

Paper V:

A node-splitting discrete element model for fluid-structure interaction

A. Hafver, E. Jettestuen, J. Feder, P. Meakin and A. Malthe-Sørenssen

Published in Physica A, Vol. **416**, 2014, pp. 61-79
doi:10.1016/j.physa.2014.08.039

Physica A 416 (2014) 61–79

Contents lists available at ScienceDirect

Physica A

journal homepage: www.elsevier.com/locate/physa

A node-splitting discrete element model for fluid–structure interaction

Andreas Hafver [a,*], Espen Jettestuen [b], Jens Feder [a], Paul Meakin [c], Anders Malthe-Sørenssen [a]

[a] Physics of Geological Processes, University of Oslo, P.O. Box 1048 Blindern, 0316 Oslo, Norway
[b] International Research Institute of Stavanger, P.O. Box 8046, N-4068 Stavanger, Norway
[c] Temple University, Department of Physics, Barton Hall, Philadelphia, PA 19122-6082, United States

HIGHLIGHTS

- A novel discrete element model (DEM) for fracturing in elastic solids is proposed.
- By splitting nodes, contrary to breaking bonds, lattice artefacts are reduced.
- Fracture volumes and surfaces are naturally represented for all fracture apertures.
- The fracture representation simplifies coupling of fracturing to fluid transport.
- Applications include fracturing driven by fluid generation in geological systems.

ARTICLE INFO

Article history:
Received 2 April 2014
Received in revised form 12 July 2014
Available online 23 August 2014

Keywords:
Discrete element model
Spring networks
Fracturing
Hydraulic fracturing

ABSTRACT

A new discrete element model (DEM) has been developed for the purpose of simulating dynamic fracturing driven by the internal generation of fluids in low permeability elastic solid bodies. The elastic material is represented by a network of nodes connected by springs, and fracture nucleation and propagation is implemented by splitting nodes and reconnecting the spring network. This produces realistic fracture shapes, and reduces lattice artefacts compared with DEM models in which fracturing is implemented by breaking/removal of springs. Fracture volumes and surfaces are explicitly represented in terms of the voids in the reconnected spring network, simplifying the coupling between mechanical deformation and fluid pressure in the fractures, and facilitating the modelling of fluid transport. The model is illustrated by applying it to fracturing driven by internal fluid generation in an impermeable quasi two-dimensional system. This is relevant for many geological processes, including primary migration of oil and gas in low-permeability source rock. The model may also be adapted to hydraulic fracturing processes, which are of industrial interest in connection with unconventional oil and gas production.

1. Introduction

Coupled processes in which fracturing of a solid is driven by fluids flowing through an evolving fracture network are common in geology and engineering. Hydraulic fracturing is used industrially to recover oil and gas from shale, and it has become a technology of increasing economic and geopolitical importance, as well as public and professional concern, over

* Corresponding author. Tel.: +47 99573565.
E-mail address: andreas.hafver@fys.uio.no (A. Hafver).

http://dx.doi.org/10.1016/j.physa.2014.08.039

the past decade [1,2]. A similar process is believed to occur naturally in maturing organic-rich shale, driven by pressure build-up as kerogen is thermally decomposed into lower molecular mass, lower density hydrocarbons. This may be an important mechanism for primary migration, the process by which oil and gas is transported within and expelled from source rocks [3–5]. Fracturing due to internal pressure accumulation also occurs in other geological systems. For example, there is evidence indicating that the month-long sequence of earthquakes striking the Umbria and Marche regions of northern Italy in 1997 was sustained by the release of over-pressured trapped CO_2 [6,7]. Other examples of coupled fluid drainage and fracturing include decomposition of methane hydrate coupled with fracturing of sediments, which may have an impact on Earth's climate [8], the expulsion of water from rocks in subduction zones, which can play an important role in earthquake triggering [9], and internal generation of fission gases causing fracturing of nuclear fuel pellets [10], which is a challenge for the nuclear energy industry.

Pressure driven fracture processes have been studied analytically by several authors for simple and idealised systems [11–15]. Although such models provide useful insights, numerical modelling is required to study more complex systems. However, the numerical modelling of these coupled processes presents many challenges. In principle, molecular dynamics (MD) can be used to model fracturing of a solid in contact with a fluid on the molecular scale, but this approach is practical only on very small time and length scales. Similarly, continuum approaches, such as finite element models (FEM) may be applied to dynamic fracturing by resolving the evolving fractures with a fine adaptive mesh, but this is computationally costly.

Many authors have suggested alternative ways to accommodate fracturing in continuum models. For example, a large number of generalised FEM models, which enable representation and tracking of dynamic fracture boundaries without the need for remeshing, have been developed [16–19]. However, these frameworks tend to be more elaborate than standard FEM approaches and require special treatment of the regions near fractures. Also, the fracture volumes and surfaces are typically defined implicitly, complicating the coupling between the model used to simulate fluids in the fracture apertures and the deformation and fracturing of the surrounding solid. Phase field models [20–23] can also be used to simulate the evolution of geometrically complex fracture systems, but, to our knowledge, they have not been coupled with models for fluid transport and used to simulate hydraulic fracturing. Even if such coupling is possible, the high resolution required to resolve fractures could be a limiting factor in applications to large fracture systems.

Discrete element models (DEM), sometimes referred to as spring network models or distinct element models, are discrete alternatives to continuum models, and they can be used to model deforming solids on a macroscopic scale. Depending on the application, the discrete elements may represent actual grains of a granular material or merely be an abstract discretisation of an essentially continuous medium. In DEMs, the neighbouring elements, representing the solid material, are connected by bonds (typically springs or beams), whose properties may be adjusted to achieve a desired material rheology. Fracturing is typically implemented by breaking bonds that are strained beyond a critical threshold. Problems studied with this approach include cracking of thin films [24], formation of extensional fractures in clay [25,26], weathering processes [27], fragmentation processes [28,29], fracturing by diffusion controlled volume changing reactions [30] and acoustic emissions from micro fracturing in porous rock [31]. An alternative DEM model, in which the elements represent a Voronoi tessellation of a continuum and fractures are represented implicitly as shear bands, has been used to model failure of concrete [32,33]. As the above-mentioned examples demonstrate, DEM models are able to simulate complex fracture process realistically, and it has been shown that such models are able to reproduce isotropic elastic behaviour [34,35]. However, the representation of fractures in terms of broken springs introduces lattice artefacts. Furthermore, the reconstruction of fracture volumes and fracture geometries from broken bonds is ambiguous or unrealistic, unless the DEM model represents a granular medium, in which case fracture surfaces may be interpreted in terms of node contours. For applications in which fractures are considered to be empty and fracture surfaces are traction-free, the exact volume of a fracture or location and orientation of fracture surfaces is not important. The same is not true for applications in which fracturing is coupled to pressure forces exerted on the solid by fluids contained in fractures. As a result, studies in which DEM models have been applied to hydraulic fracturing [36,35] have represented fractures implicitly, by calculating local porosities from the DEM node positions and using a Kozeny–Carman or other empirical permeability–porosity relationship to determine local permeabilities. Fluid transport is then modelled as Darcy flow on a finer underlying mesh. In these models, the forces that fluids exert on the solid are derived from the fluid pressure gradient. A similar coupling to a fluid pressure field was used in a FEM model based on Biot poroelasticity equations in Ref. [37]. Fractured rocks are typically 'dual porosity' systems, in which most of the fluid is contained in the low permeability unfractured rock matrix, but most of the fluid flow occurs in fractures. A challenge associated with models based on a dual porosity field is the need to resolve sharp changes in pressure gradients if the permeability in the unfractured solid is small, which makes them most useful for modelling high porosity materials or fractures on a microscopic scale.

The DEM model introduced here extends previous DEM models to applications in which explicit representations of fracture volumes and surfaces are required. The novel approach differs from previous models in the way in which fractures are introduced, by splitting nodes, reconnecting the spring network and inserting fracture triangles in the resulting voids. Fracture volumes and fracture surfaces may be defined in terms of these fracture triangles, and this enables easy coupling to fluid transport and pressure forces, without the need to invoke additional computational meshes or other elaborate schemes. The triangulation of the elastic solid does not change upon fracturing, and hence there is no need to interpolate or recalculate properties of the elements during simulations.

An additional advantage of this fracture representation is that fracture propagation directions are less restricted than in typical DEM models, and fractures may follow straight paths, resulting in realistic fracture shapes even for fractures that are a few mesh units long. As a result, the stress field around fractures can be well represented with low mesh resolution,

and this reduces the computational resources required to simulate large systems of many interacting fractures. The model is particularly suitable for modelling low-permeability or macroscopic systems, in which fractures effectively constitute all of the permeability, such that pressure forces can be treated as boundary forces on fracture surfaces.

To illustrate the model, a dynamic fracturing process is considered, in which the driving force of fracturing is provided by accumulation of fluid pressure in the fractures. The modelled system represents an isotropic elastic solid containing a set of pre-existing fracture seeds and with uniform production of dissolved gas within the solid matrix. The dissolved gas can diffuse through the solid and exsolve into fractures, and the fracture system may evolve in response to the gas pressure exerted on fracture walls. This model set-up closely resembles experiments performed by Kobchenko et al. [38] in which fracturing in a layer of gelatine confined between two glass plates was driven by uniform CO_2 generation and subsequent exsolution of CO_2 gas. An example of a fracture network generated in one of these experiments is shown in Fig. 1, together with a visualisation of the stress field around a set of fractures. In these experiments, fractures nucleate as bubbles, governed by the supersaturation of CO_2, however, the nucleation is a complex process, and is ignored here, as it is not essential for conveying the ideas of the model.

2. Model

2.1. Elastic interactions

In the model presented here, the elastic solid is represented as a triangular lattice of nodes connected by springs. Each pair of nearest neighbour nodes, i and j, exert equal and opposite forces on each other, given by

$$\vec{F}_{i,j} = -\vec{F}_{j,i} = k_{i,j}(|\vec{x}_j - \vec{x}_i| - l_{i,j})\hat{n}_{i,j}, \tag{1}$$

where $\vec{x}_i$ and $\vec{x}_j$ are the node positions, $k_{i,j}$ is a spring force constant, $l_{i,j}$ is the equilibrium separation of the nodes, and $\hat{n}_{i,j}$ is the unit vector pointing from node i to node j. In order to ensure homogeneous behaviour and consistent scaling of spring forces with lattice resolution, the individual spring constants are set to $k_{i,j} = A_{i,j}k/l_{i,j}$, where $A_{i,j}$ is the area of the Voronoi interface between node pair (i, j) [32,33]. (The Voronoi interface has unit of length in two dimensions, but the system is assumed to also have a uniform thickness in the third dimension, as in the experiments of Kobchenko et al. [38].)

For a uniform triangular lattice with a node separation of $l_{i,j} = l, A_{i,j} = lh/\sqrt{3}$ for node pairs in the interior of the lattice, and $k_{i,j} = hk/\sqrt{3}$, where h is the thickness of the solid layer. The regular triangular lattice with associated Voronoi interfaces is illustrated in Fig. 2. The Voronoi areas and spring constants may be split into contributions $A^e = lh/2\sqrt{3}$ and $k^e = hk/2\sqrt{3}$ from the individual triangle elements e, and the spring force per element, for a pair of adjacent nodes i and j, is given by

$$\vec{F}^e_{i,j} = -\vec{F}^e_{j,i} = k^e(|\vec{x}_j - \vec{x}_i| - l)\hat{n}_{i,j}. \tag{2}$$

This separation of forces into element-wise contributions ensures that forces also scale appropriately at system boundaries (where node pairs are unique to one triangle element), and it ensures that elastic energy and forces are redistributed consistently, without a need for adjusting springs, when the node connectivity changes during fracturing. Several authors (e.g. Refs. [34,35]) have shown that regular triangular spring lattices can reproduce isotropic elasticity in the continuum limit. Since the springs exert only stretching and compression forces, it can be shown that the regular triangular spring network corresponds to a solid with a Poisson ratio of $\nu = 1/3$ and Young's modulus of $E = 2k/3 = 4k^e/\sqrt{3}h$.

2.2. Substrate attachment

In addition to inter-nodal spring forces, every node is connected to a rigid substrate by weak springs. The spring attachment forces are given by

$$\vec{F}^e_{i,\text{substrate}} = \frac{k^s}{6}(\vec{x}^0_i - \vec{x}_i), \tag{3}$$

where $\vec{x}^0_i$ is the original position of node i, and k^s is the substrate attachment spring force constant. These forces are conveniently defined per triangle, because the lattice topology is subject to change during fracturing. Any node may be part of six or fewer triangles, and, hence, the attachment strength effectively scales with the associated area of the node that is in contact with the substrate.

The effect of the weak bonding to the substrate is to localise mechanical interactions, which is realistic in the context of the gelatine experiments of Ref. [38], in which the gelatine layer is constrained by confinement to a Hele-Shaw cell and adhesion of the gel to the glass walls. Substrate attachment also plays a role in other quasi-two dimensional fracturing process, for example desiccation fracturing in mud or the formation of drying fractures in paint films [24,39–42].

In addition to elastic forces and substrate attachment, the solid is subject to pressure forces on fracture surfaces, and this is discussed in the following section.

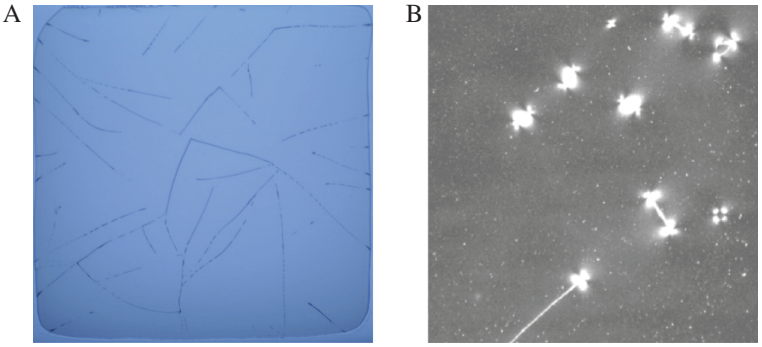

Fig. 1. A: Example of a fracture network from gelatine experiments described in Ref. [38]. B: Visualisation of the strain field around fractures, using cross polarisers.

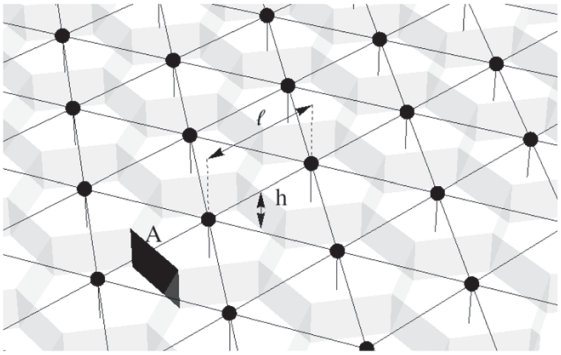

Fig. 2. The regular triangular lattice used in the DEM model. Nodes (indicated by black dots) are connected by springs to nearest neighbour nodes and to an underlying rigid substrate. The equilibrium node separation, l, and Voronoi interfaces between nodes are used to scale the spring force constants ($A = hl/\sqrt{3}$).

2.3. Fracturing and the mechanical coupling to fluid pressure

The novelty of the DEM model described here lies in the implementation of fracturing and the way that the fluid pressure in fractures is coupled with the mechanical deformation. Unlike conventional DEM models, fractures nucleate and propagate by splitting nodes, rather than by breaking springs. The procedure for inserting new fractures is illustrated in Fig. 3, and is implemented in three steps:

1. Determine where and when a fracture will nucleate/propagate according to a fracture criterion (discussed below);
2. Determine the orientation of the new fracture segment;
3. Reconnect the lattice, by disconnecting springs on one side of the fracture from the old node and attaching them to the new node. Insert two new fracture triangle elements in the resulting void.

The coupling of fluid pressure to mechanical deformation is implemented by applying normal forces on the fracture walls. In order to do this, it is necessary to define what is meant by a fracture wall, but there are several alternative ways to associate a fracture volume and fracture surface to the voids created by node splitting. One obvious approach would be to define the fracture surface as the interfaces between bulk triangles and fracture triangles (red contours in Fig. 3). However, using this approach, the relative surface area to volume ratio for a fracture depends on whether the fracture path follows one of the mesh directions or not (as can be seen from Fig. 3(E)–(F)–(G)). This problem can be resolved by using a projection of the interface instead (blue contour in Fig. 3). With the first approach, fracture surfaces elements are always oriented along one of the three mesh directions. With the second approach, fractures are smoothed, and can be made to appear straight along six different planes. Fig. 4 demonstrates how the fracture surface may be distributed among the nodes on fracture boundaries using the two proposed approaches. Since the second representation is a projection of the first, the resultant surface normal vectors per node obtained from the two approaches are equal (the red vectors sum up to the blue vector in Fig. 4), and hence the mechanical coupling to the fluid pressure in the fractures is equivalent. The force contribution to node

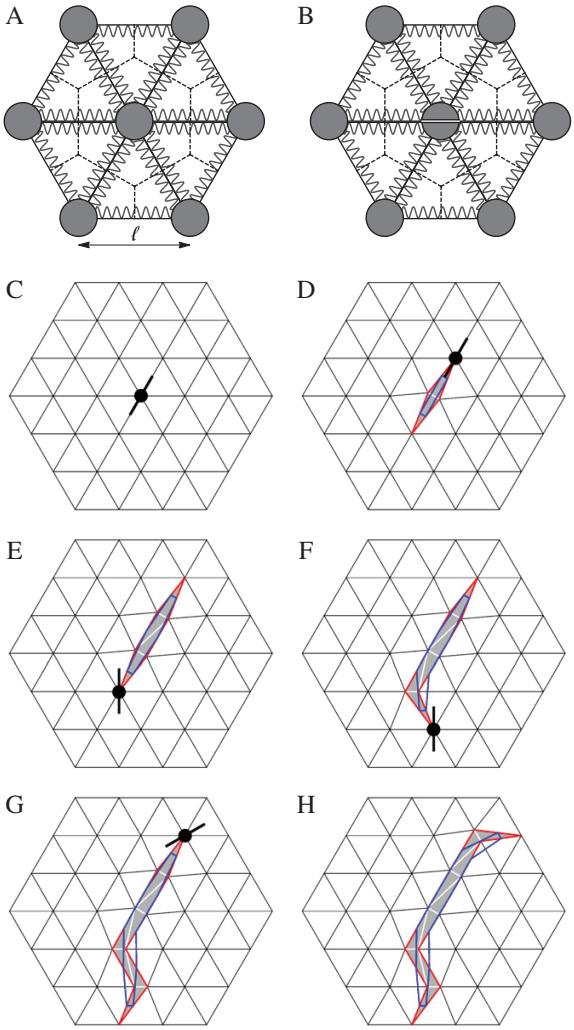

Fig. 3. Illustration of fracturing by node splitting. A: Configuration of springs and nodes before splitting. Each pair of nodes is connected by one spring per triangle. B: Configuration after splitting of the central node. Springs above the fracture plane (horizontal in this case) are reconnected to the new node. C, D, E and F: Possible growth sequence of a fracture. Black lines represent springs. The node position at which a fracture will nucleate/propagate next is indicated with a black dot. The direction in which the fracture will propagate is indicated by thick, black line segments. The fracture triangles (grey) are inserted in the open voids that form when the springs are reconnected. Two alternative ways are proposed to represent fracture contours on the reconnected mesh. Alternative 1 (highlighted in red) is to consider the interface between bulk and fracture triangles as the fracture surface. Alternative 2 (highlighted in blue) is to use a projected contour, as explained in the text and illustrated in Fig. 4. When the projected fracture contour (blue) is used, the fracture path appears straight even when the split nodes lie on alternating paths along the spring network (e.g. the vertical fracture segment formed in steps E → F → G). The fractures are drawn with fixed aperture widths for illustration purposes. (For interpretation of the references to colour in this figure legend, the reader is referred to the web version of this article.)

i from fracture triangle f with gas pressure p_f is given by

$$\vec{F}_i^f = p_f \vec{A}_i^f, \tag{4}$$

where $\vec{A}_i^f$ is defined as half the normal vector of the edge in element f that is opposite node i, as illustrated in Fig. 4.

Fig. 5 shows the difference between the fracture representation in the node-splitting model and a typical representation of fractures in bond-breaking DEM models. Unlike in the approach presented here, straight fractures in bond-breaking models consist of broken springs with alternating orientation, and the forces are asymmetrically distributed on the opposite sides of the fracture (Fig. 5(A)–(B)). Also, fractures in bond-breaking models are forced to turn in one of two directions at

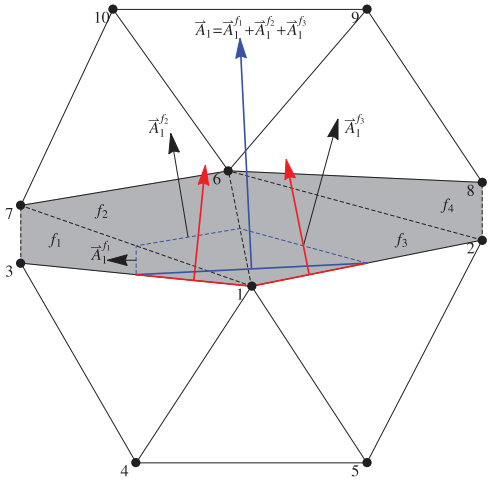

Fig. 4. Illustration of how a fracture surface area may be assigned to nodes on fracture boundaries. One way of representing the fracture surface is in terms of the interface between bulk triangles (white) and fracture triangles (grey). A part of this interface may be associated with each of the nodes on the boundary. In this example, the surface element associated with node 1 comprises half the edge between nodes 1 and 3 and half of the edge between nodes 1 and 2 (indicated by red segments with red normal vectors). An alternative way of associating a surface element to each node is to use the projected interface (highlighted in blue for node 1 in this example). The associated normal vector (highlighted in blue) can be constructed as a sum of contributions $\vec{A}_1^{f_1}$, $\vec{A}_1^{f_2}$ and $\vec{A}_1^{f_3}$ from the fracture triangles f_1, f_2 and f_3 adjacent to node 1. The vectors $\vec{A}_1^{f_i}$ correspond to half the normal vector associated with the edge of triangle f_i opposite to node 1. The blue normal vector is equal to the sum of the red normal vectors. (For interpretation of the references to colour in this figure legend, the reader is referred to the web version of this article.)

each propagation step (Fig. 5(C)). In the node-splitting model, fractures may propagate in three different directions, including straight forward (Fig. 5(D)).

Fig. 5(E)–(F) compares how fractures along lattice directions and perpendicular to lattice directions can be realised in the bond-breaking and node-splitting models, respectively. With the approach in Fig. 5(A), (C) and (E), it is ambiguous how fracture and material volumes should be represented when apertures become large, but in the node-splitting model the interpretation of fracture volumes in terms of fracture triangles works for arbitrarily large deformations.

To determine when and where fracturing will occur, the stress field at the position of each node is calculated from the inter-nodal forces acting on that node [43], i.e.

$$\sigma(\vec{x}_i) = \sum_{e,i\in e}\sum_{j\in e, j\neq i} \frac{1}{2V_i}\vec{F}_{i,j}^{e} \otimes (\vec{x}_j - \vec{x}_i), \tag{5}$$

where the first sum is over all elements e containing the node i, and the second sum is over the remaining nodes of e adjacent to i. Here V_i is the volume of the Voronoi cell associated with node i, and $\otimes$ denotes a tensor product. This formula is valid in the interior of the regular triangular mesh, and for small deformations [34,35], but cannot be expected to hold at surfaces or when the node connectivity is reduced due to broken bonds. This can be a problem in bond-breaking DEM models, but in the current model, no bonds are broken. As a result, nodes at fracture tips have the same spring connectivity as fractures in the bulk (illustrated in Fig. 6), and, consequently, Eq. (5) may be used to estimate tip stress.

In the particular application discussed here, only opening mode fractures are formed, and a tensile fracture criterion was used. A fracture propagates if the maximum principal stress at the tip, $\sigma_1(\vec{x}_i)$, exceeds a critical tensile strength T_C, i.e.

$$\sigma_1(\vec{x}_i) > T_C. \tag{6}$$

If this criterion is met, the tip node is split and the neighbouring node in the direction that is closest to the direction of the maximum hoop stress becomes the new tip. The hoop stress is the component $\sigma_{\theta\theta}$ of the stress tensor in polar coordinates, and it is related to the Cartesian stress by

$$\sigma_{\theta\theta} = \sigma_{xx}\sin^2(\theta) + \sigma_{yy}\cos^2(\theta) - \sigma_{xy}\sin(2\theta). \tag{7}$$

2.4. Gas diffusion and exsolution

Although the DEM model described in this paper can be used to simulate a variety of deformation and fracturing processes, the current work is motivated by experiments in which fracture nucleation and growth is driven by gas generation in

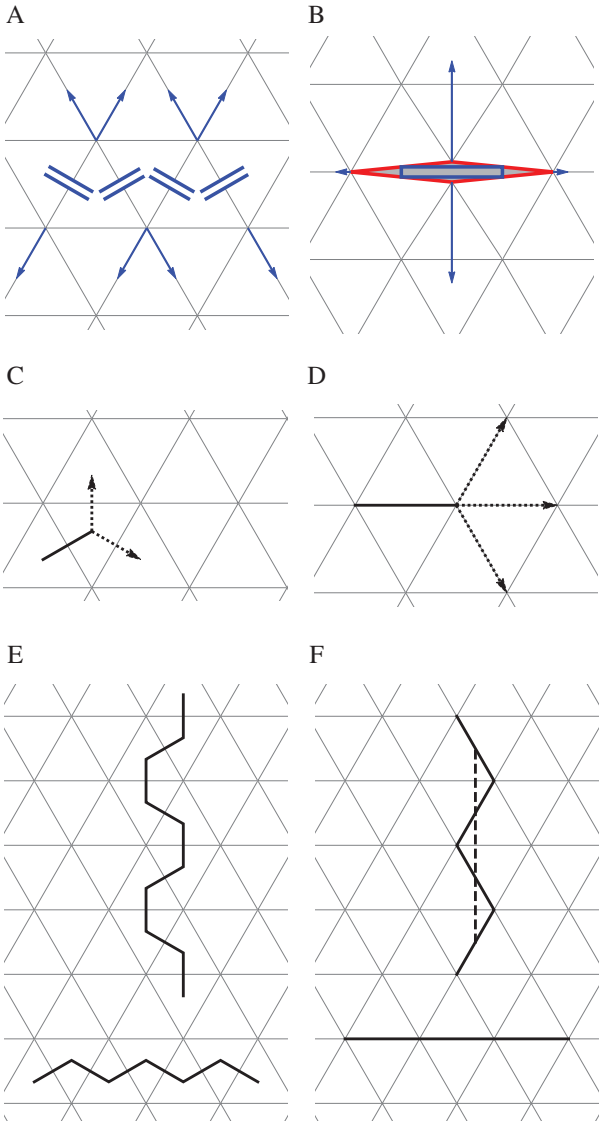

Fig. 5. Comparison of fracture representations in DEM models where fracturing is implemented by breaking of bonds (A) and by splitting of nodes (B). The directions of fracture forces exerted on the nearby nodes are indicated with blue arrows. In bond-breaking models a propagating fracture must turn in one of two directions (C). In the node-splitting model, propagating fractures may turn in one of two directions or advance without turning (D). E–F: Comparison of fractures along lattice directions and perpendicular to lattice directions in the bond-breaking and node-splitting models, respectively. In the node-splitting model, fractures along lattice directions are straight (horizontal fracture in F), and fractures perpendicular to lattice directions become straight when represented in terms of the projected fracture contour (dashed line in F). (For interpretation of the references to colour in this figure legend, the reader is referred to the web version of this article.)

the solid matrix, gas exsolution and diffusion of dissolved gas down chemical potential gradients into fractures. It is assumed that diffusion of dissolved gas in the bulk material is governed by Fick's law, i.e.

$$\frac{\partial c}{\partial t} = D\nabla^2 c + \gamma. \tag{8}$$

Here c is the molar concentration of dissolved gas, and γ is the gas production rate, which was chosen to be uniform in both time and space. Eq. (8) was solved implicitly by means of a finite difference approximation and a backward Euler scheme on the same computational mesh that was used for the elastic problem. The concentration c_i in node i at time step $n + 1$ is

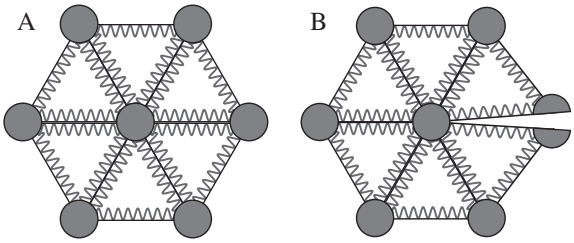

Fig. 6. Nodes in the bulk (central node in A) and nodes at fracture tips (central node in B) are connected to the same number of springs. Hence, for small apertures, the stress field at fracture tips may be approximated by Eq. (5).

thus given by

$$V_i \frac{c_i^{n+1} - c_i^n}{\Delta t} = \sum_{e, i \in e} \sum_{j \in e, j \neq i} \kappa (c_j^{n+1} - c_i^{n+1}) + V_i \gamma, \tag{9}$$

where $\kappa = hD/2\sqrt{3}$. κ is conveniently defined per triangle, such that the fluid flux may be consistently defined at external boundaries and along fracture surfaces, without the need for readjustment when new fractures are formed. The factor $h/2\sqrt{3}$ in the definition of κ results from the scaling of the diffusion flux by the distance and shared Voronoi interface areas between nodes, in the same way that the spring force constants per triangle, k^e, were scaled in the elastic part of the model described above.

For the purpose of fluid transport, each set of connected fracture triangles is treated as one single fracture node with a volume of V_F, equal to the sum of volumes of its constituting fracture elements. Combining the fracture elements in this way is equivalent to assuming that the transport in a fracture is much faster than diffusion in the solid matrix. According to Henry's law, the pressure in a fracture is in chemical equilibrium with the dissolved gas at its surface if $p = k_H c$, where k_H is Henry's coefficient. Assuming that the gas is an ideal gas, the concentration of the gas in the fracture is $c_F = p/RT$, where R is the universal gas constant and T is the absolute temperature. The amount of gas contained in a fracture is given by $c_F V_F$. Due to numerical considerations, it is advantageous to quantify fracture concentration in terms of the rescaled variable $u_F = p/k_H = c_F/\alpha$, where $\alpha = k_H/RT$ (because this allows the full transport problem to be expressed in matrix–vector notation with a symmetric matrix). For simplicity, it is assumed that the flux across fracture surfaces is proportional to the deviation from chemical equilibrium [30]. Thus, for fracture F, the concentration is updated according to

$$\alpha V_F \frac{u_F^{n+1} - u_F^n}{\Delta t} = \sum_{j \in \Omega_F} \beta A_{j,F} (c_j^{n+1} - u_F^{n+1}), \tag{10}$$

where $\alpha = RT/k_H$, β is a surface evaporation coefficient, Ω_F is the set of nodes adjacent to the fracture F, and $A_{j,F}$ is the fracture surface associated with node j. To achieve mass conservation, a flux $\beta A_{j,F}(u_F^{n+1} - c_j^{n+1})$ must be subtracted from each of the surface nodes $j \in \Omega_F$. For the surface area $A_{j,F}$ the magnitude of the blue surface normal vector illustrated in Fig. 4 (i.e. $A_{j,F} = \sum_{f \in F, j \in f} \vec{A}_j^f$) was used.

2.5. Lattice relaxation and pressure equilibration

The model is evolved in time by repeating the following procedure at every time step:

1. Update the concentrations c_i and u_F by solving Eqs. (9)–(10);
2. Obtain new fracture pressures using $p_F = k_H u_F$;
3. Repeat the following until no fracturing occurs:
   (a) Relax the lattice (described below);
   (b) Calculate the new stress state, and create new fractures if the fracture criterion (Eq. (6)) is met.

Lattice relaxation is assumed to occur very rapidly compared with transport, such that the gas content in each fracture is conserved during mechanical relaxation. When the lattice deforms during relaxation, the fracture volumes may change, and this requires adjustment of the pressures. To account for coupling between the deformation of the lattice and the fluid pressures in the fractures, the lattice is relaxed using an iterative scheme, based on the following steps, which are repeated until all of the forces are below a threshold value:

1. Bring the lattice closer to mechanical equilibrium by solving the linearised mechanical problem, keeping the current fracture pressures fixed (explained below);
2. Calculate new fracture volumes, V_F, based on new node positions, and adjust the fracture pressures according to the ideal gas law ($P_F V_F = \text{const.}$).

Since the solution of the linearised mechanical problem differs from the solution of the full non-linear problem, step 1 does not bring the lattice into equilibrium with the gas filled fractures. However, the procedure is repeated with readjusted pressures until force balance is reached, and the forces are consistent with the full, non-linear problem.

The linearised mechanical problem may be stated in matrix–vector form as $A\mathrm{d}X = B$, where $\mathrm{d}X$ is the vector containing the displacements of the nodes at a given iteration. The matrix A and vector B may be set up in various ways. A standard way to linearise the problem would be to construct a total energy function for the system and to obtain A and B by a Taylor expansion (i.e. make A the Hessian matrix of the total energy function and B the current forces on each node). In practice, however, the latter approach is inefficient, because the Hessian depends on node positions and must be recomputed at each iteration. This can pose a significant computational cost, and, therefore, an alternative method was used, which only requires A to be recomputed whenever new fracture elements are introduced.

To construct the matrix A and vector B, let $\vec{x}_i$ denote the current position of node i and let $\vec{x}'_i = \vec{x}_i + \mathrm{d}\vec{x}_i$ denote the new node position after displacement by a small distance vector $\mathrm{d}\vec{x}_i$. The new spring force $\vec{F}'^{e}_{i,j}$ exerted through element e on node $i \in e$ by node $j \in e$ after displacement, may be expressed as (according to Eq. (2))

$$\begin{aligned}
\vec{F}'^{e}_{i,j} &= k^e(|\vec{x}'_j - \vec{x}'_i| - l)\hat{n}'_{i,j} \\
&= k^e(\vec{x}'_j - \vec{x}'_i) - k^e l\hat{n}'_{i,j} \\
&= k^e(\mathrm{d}\vec{x}_j - \mathrm{d}\vec{x}_i) + k^e(\vec{x}_j - \vec{x}_i) - k^e l\hat{n}'_{i,j} \\
&\approx k^e(\mathrm{d}\vec{x}_j - \mathrm{d}\vec{x}_i) + k^e(\vec{x}_j - \vec{x}_i) - k^e l\hat{n}_{i,j} \\
&= k^e(\mathrm{d}\vec{x}_j - \mathrm{d}\vec{x}_i) + \vec{F}^{e}_{i,j},
\end{aligned} \tag{11}$$

where $\vec{F}^{e}_{i,j}$ is the spring force before node displacement. In the second to last step of Eq. (11), the unit direction vector $\hat{n}'_{i,j}$ associated with the new force was approximated by the unit vector $\hat{n}_{i,j}$ of the old force, which is valid as long as $|\mathrm{d}\vec{x}_j - \mathrm{d}\vec{x}_i| \ll l$ (i.e. for small displacements). The substrate attachment force (Eq. (3)) contributed by an element e on a node $i \in e$ already depends linearly on the node positions, and can be expressed as

$$\begin{aligned}
\vec{F}'^{e}_{i,\mathrm{substrate}} &= \frac{k^s}{6}(\vec{x}^0_i - \vec{x}'_i) \\
&= \frac{k^s}{6}(\vec{x}^0_i - \vec{x}_i - \mathrm{d}\vec{x}_i) \\
&= -\frac{k^s}{6}\mathrm{d}\vec{x}_i + \vec{F}^{e}_{i,\mathrm{substrate}},
\end{aligned} \tag{12}$$

where $\vec{F}^{e}_{i,\mathrm{substrate}}$ is the substrate attachment force before node displacement. The new forces after displacement (Eqs. (11)–(12)) must balance the pressure forces on the fracture walls. The equation giving the displacement $\mathrm{d}\vec{x}_i$ of a node i is therefore

$$\sum_{e,i\in e}\left(\frac{k^s}{6}\mathrm{d}\vec{x}_i - \sum_{j\in e, j\neq i} k^e(\mathrm{d}\vec{x}_j - \mathrm{d}\vec{x}_i)\right) = \vec{F}_i, \tag{13}$$

where $\vec{F}_i$ is the total (spring, substrate and pressure) force acting on the node before displacement. In Eq. (13), the coupling between displacements in the x- and y-directions are completely absorbed into $\vec{F}_i$, so the x- and y-displacements can be computed separately. More precisely, the displacements in the x- and y-directions can be obtained from the two matrix–vector equations,

$$A\mathrm{d}X = B_x \quad \text{and} \quad A\mathrm{d}Y = B_y, \tag{14}$$

where $\mathrm{d}X = \{\mathrm{d}x_1, \mathrm{d}x_2, \ldots\}$ and $\mathrm{d}Y = \{\mathrm{d}y_1, \mathrm{d}y_2, \ldots\}$ contain the node displacements in the x- and y-directions, and $B_x = \{F^x_1, F^x_2, \ldots\}$ and $B_y = \{F^y_1, F^y_2, \ldots\}$ contain the x- and y-components of the node forces. The off-diagonal elements of the matrix A are given by

$$A_{i,j} = -\sum_{e,(i,j)\in e} k^e, \tag{15}$$

and the diagonal elements of A are given by

$$A_{i,i} = \sum_{e,i\in e}\left(2k^e + \frac{k^s}{6}\right). \tag{16}$$

A remains constant during the relaxation and pressure equilibration, and by inverting it numerically whenever new fractures are nucleated or existing fractures grow, one can obtain the displacements at each iteration by evaluating the matrix–vector products $\mathrm{d}X = A^{-1}B_x$ and $\mathrm{d}Y = A^{-1}B_y$, instead of re-solving the linear problem. The decoupling of displacements in the x- and y-directions implies additional computational gains for large systems, because the number of numerical operations required by linear solvers typically increases more than linearly with the number of degrees of freedom.

Table 1
Summary of dimensionless model parameters.

Parameter	Unit	Dimension-less form
Equilibrium spring length, l	m	$\equiv 1$
Spring constant, $k^e = \sqrt{3}Eh/4$	m^{-1} N	$\equiv 1$
Time step, Δt	s	$\equiv 1$
Gas solubility, k_H	$\mathrm{mN\ mol}^{-1}$	$\equiv 1$
Substrate attachment, k^s	m^{-1} N	k^s/k^e
Critical tensile stress, T_C	m^{-2} N	T_C/E
Bulk permeability, $\kappa = Dh/2\sqrt{3}$	$\mathrm{m}^3\ \mathrm{s}^{-1}$	$D\Delta t/2\sqrt{3}l^2$
Production rate, γ	$\mathrm{m}^{-3}\ \mathrm{s}^{-1}$	$\gamma hl^2\Delta t$
Fracture capacity, α	–	k_H/RT
Evaporation coefficient, β	$\mathrm{m\ s}^{-1}$	$\beta\Delta t/l$

2.6. Dimensionless parametrisation

For convenience, dimensionless parameters are used in the remainder of this article, and they are listed in Table 1. The dimensionless equilibrium spring length, l, time step, Δt, spring constant, k^e, and gas solubility, k_H, have values of unity. Defining $k_H \equiv 1$ makes the auxiliary variables u and the fracture pressures equal.

3. Results

Test results are presented in this section, to demonstrate the merits of the model. The parameter space is too large to explore exhaustively, but insights can be obtained from a few simple examples.

3.1. Fracture shape

The node-splitting DEM model produces realistic fracture shapes, even at low resolution and with fractures that are a few grid units long. This is demonstrated in Fig. 7, in which the aperture of fractures is plotted for various resolutions and different fluid pressures in the fracture. The fractures have approximately elliptical shapes, as predicted by linear elastic theory for cracks with infinitesimal apertures and with uniform internal pressures [44,45]. Even for fairly large fracture aperture/fracture length ratios, this prediction appears to be valid.

3.2. Effects of fracture orientation

The fractures in the model are not constrained to follow grid directions. As a test for isotropy, Fig. 8 shows how the total energy, fracture tip energy density, stress tensor invariants and fracture volume depend on the fracture propagation direction. We find that the total elastic energy of the grid and the energy density at the crack tips are almost identical functions of the fracture length for horizontal and vertical fractures. The stress invariants $I_1 = \mathrm{tr}(\sigma)$ and $I_2 = \det(\sigma)$ at the fracture tips are also fairly similar for horizontal and vertical fractures, but are slightly lower for vertical fractures. This is due to the fact that the nodes at the tip of vertical fractures are positioned slightly off the longitudinal fracture symmetry axis. The fracture volume as a function of fracture length is not affected by the direction, which is important with respect to the coupling to fluids in fractures.

3.3. The stress field around fractures

Fig. 9 shows examples of the stress fields around vertical and horizontal fractures of the same length. A direct quantitative comparison between the two cases is difficult because it requires the stress fields to be rotated, scaled and perfectly aligned. In Fig. 10 a visual comparison is shown instead, by plotting contours of the principal shear stress (normalised by fluid pressure) for a horizontal and a vertical fracture of equal length, together with the analytic solution found by Westergaard [44]. This analytic solution, as elaborated by Sneddon [45], can be expressed in terms of the stress function

$$Z = p\left(\frac{z}{\sqrt{z^2 - a^2}} - 1\right), \quad (z = x + \mathrm{i}y), \tag{17}$$

where a is the fracture half length, and the stress components can be obtained from the relations

$$\begin{aligned} \frac{1}{2}(\sigma_{xx} + \sigma_{yy}) &= \mathrm{Re}(Z), \\ \frac{1}{2}(\sigma_{xx} - \sigma_{yy}) &= y\mathrm{Im}(Z'), \\ \sigma_{xy} &= y\mathrm{Re}(Z'), \end{aligned} \tag{18}$$

where $Z' = \partial Z/\partial z$.

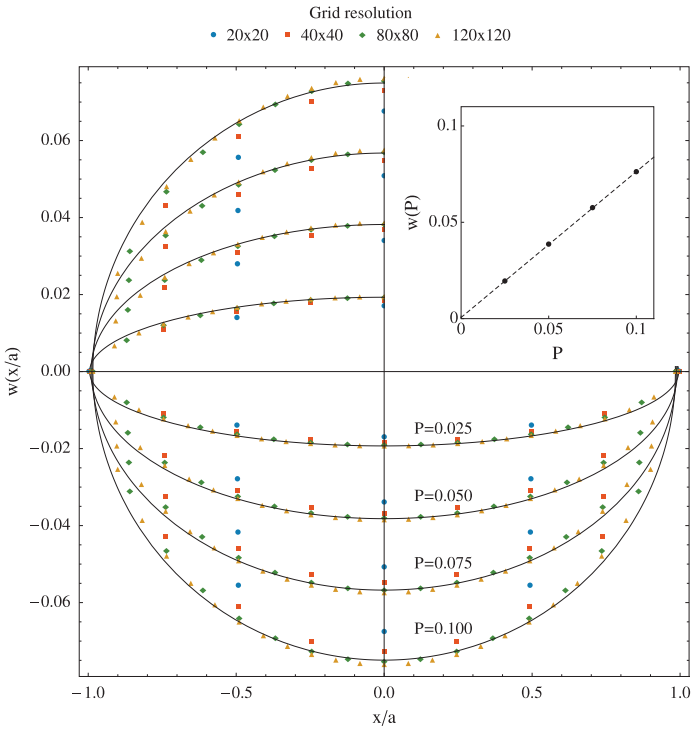

Fig. 7. Variation of the fracture aperture with grid resolution for different pressures. Each data point represents the position of a node on the fracture boundary (x is the position along the major axis of the fracture, and w is the displacement in the orthogonal direction). The black lines show fitted ellipses, indicating that fractures have approximately elliptic shapes. The inset shows that the maximum aperture is proportional to the pressure. The data were obtained using a fracture with half length $a = 0.1L$, where L is the system side length (grid resolution). External boundaries were fixed, and there was no substrate attachment.

A comparison of Fig. 10(B)–(C) with Fig. 10(A) shows that the stress field around both the horizontal and vertical fractures are fairly consistent with the analytic solution away from the crack tips (the vertical fracture has been rotated for ease of comparison). Near the crack tip, the Westergaard solution diverges, but this is not captured by a discrete model with limited resolution. It should, however, be kept in mind that the stress field divergence is an artefact of the continuum description and not a physical effect (after all, any material is discrete on short length scales, and its atomic constituents experience forces, not stress). For the vertical crack, the principal shear stress is slightly asymmetric at the crack tip. This is because the stress is evaluated at the grid nodes, and the tip nodes of vertical fractures fall slightly off the symmetry axis of the fracture plane.

3.4. Pressure development in a propagating fracture

Fig. 11 shows the time evolution of the gas pressure in a single propagating fracture, under various conditions. The fracture growth is intermittent, with a pressure drop associated with each propagation event. The results demonstrate that the pressure required to initiate fracture growth depends on the parameters that determine material properties and the strength of attachment to the rigid substrate, namely T_C and k_S.

For lower node breaking thresholds or weaker substrate attachment, fracturing occurs at lower pressures, and the waiting time before successive propagation events is shorter. The growth rate increases as α decreases or β and κ increase, because these parameters influence the time required to inflate fractures with gas. The frequency of events increases as fractures grow longer, because stress becomes more concentrated at the tips, and a smaller pressure is required to drive fracture propagation. In addition, the transport of fluid into the fractures increases because of the increase in fracture surface area. However, the substrate attachment localises elastic interactions, and the tip stress concentration eventually becomes independent of the fracture length. At some point, the fracture propagates at constant pressure, and this pressure increases with the production rate, γ, and decreases with the material strength, T_C.

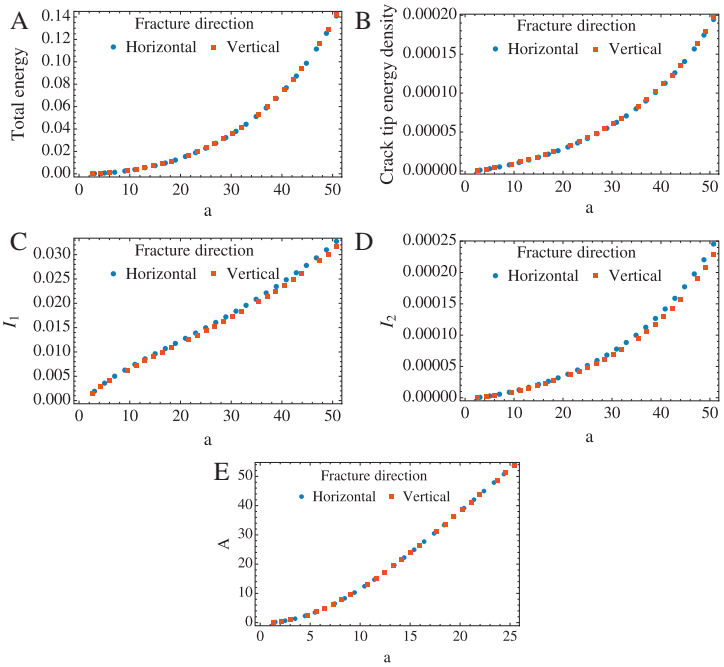

Fig. 8. A: Total energy of system containing crack of half-length a. B: Energy density at the tip of a crack with half-length a. C: First stress invariant, $I_1 = \mathrm{tr}(\sigma)$, at the tip of a crack with half-length a. D: Second stress invariant, $I_2 = \det(\sigma)$, at the tip of a crack with half-length a. E: Fracture volume as a function of fracture half-length a. Data were obtained using an approximately quadratic domain with $L = 70$. The dimensionless pressure in the fractures was $P = 0.01$, substrate attachment was turned off, and the external boundaries were free.

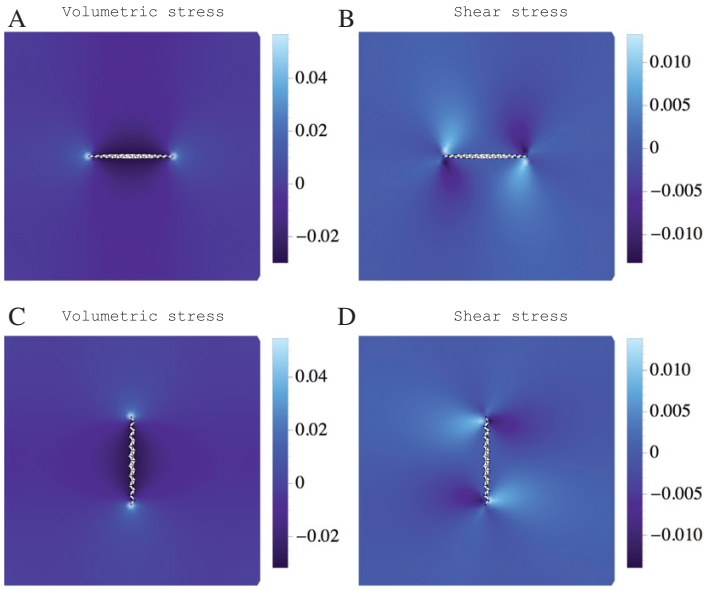

Fig. 9. A: Volumetric stress around a horizontal fracture. B: Shear stress around a horizontal fracture. C: Volumetric stress around a vertical fracture. D: Shear stress around a vertical fracture. Data were obtained using a quadratic domain with side length $L = 40$. The dimensionless pressure in cracks was $p = 0.01$, and a weak substrate attachment ($k_S = 10^{-3}$) was used.

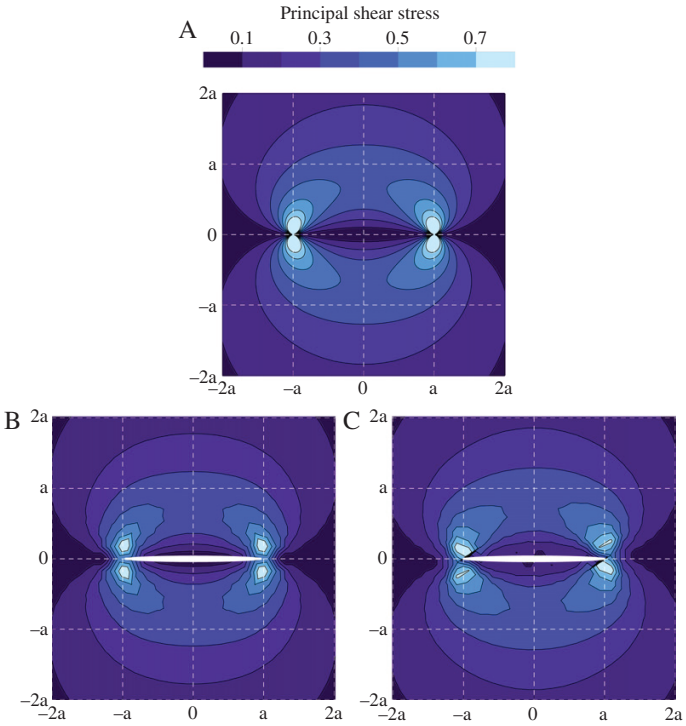

Fig. 10. The principal shear stress normalised by fluid pressure in the fracture. A: Analytic solution; B: Horizontal fracture; C: Vertical fracture (rotated for ease of comparison). The numerical examples are cropped from a larger, quadratic computational domain with side length $L = 80$. A dimensionless pressure of $p = 0.05$ and a weak substrate attachment ($k_S = 10^{-3}$) were used. The projection method was used to smooth the fracture contours in B and C.

3.5. Two interacting fractures

Fig. 12 illustrates a simulation in which two short horizontal fracture seeds were placed with a small offset in both the horizontal and vertical directions. As the fractures inflate, they interact with each other via the stress field, which affects their direction of propagation. When the breaking threshold is uniform, only the two tips directed away from the other fracture grow, because the stress field there is more favourable for growth. However, when heterogeneity is introduced, by distributing T_C randomly according to a normal distribution with 10% standard deviation, the material becomes less brittle, and the facing tips turn towards each other.

3.6. Systems of many fractures

Figs. 13–16 show examples of simulations with many (20) interacting fractures. The initial fractures seeds, formed by splitting individual nodes, were randomly distributed in space and assigned random orientations selected from $\{-\pi/3, 0, \pi/3\}$. (The fracture seed orientations are restricted to the three lattice directions, because initial fractures would need to be longer in order to continue propagating linearly in other directions.) For ease of comparison, the same set of seeds were used in all the examples. The external boundary was treated as a preexisting fracture with constant dimensionless pressure $p = 0.01$ (because of the small residual pressure, fractures that joined the boundary did not collapse completely).

In the simulation illustrated in Fig. 13 there was no distribution of material strength T_C (the material was homogeneous), and many fractures started growing at about the same time. In Figs. 14–16 the node strengths were normally distributed with a 10% standard deviation, and as a result, growth was more sequential.

Although the fluid production rate was 2.5 times higher and the fracture capacity was 75% lower (promoting faster pressure build-up) in the simulation illustrated in Fig. 15 compared with the simulation illustrated in Fig. 14, the fracture network evolved more slowly in Fig. 15 due to the faster diffusive fluid transport (κ and β were twice as large). Because fluid drainage was more effective in the simulation of Fig. 15, two fractures were not activated (the fluid pressure never built up sufficiently to propagate these fractures).

In the example in Fig. 16 the transport was so effective that only two fractures were activated, both located near the centre of the system, where the concentration of fluid in the solid matrix reaches the highest value. When these fractures connected

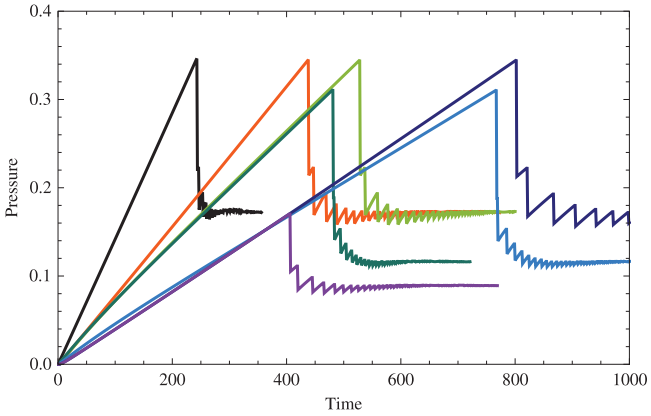

	κ	α	β	γ	k^S	T_C
	0.005	1.2	0.005	0.002	0.2	0.1
	0.005	8.	0.005	0.002	0.2	0.1
	0.0005	8.	0.005	0.002	0.2	0.1
	0.0005	8.	0.005	0.002	0.1	0.1
	0.0005	8.	0.005	0.001	0.1	0.1
	0.005	8.	0.001	0.002	0.2	0.1
	0.005	8.	0.001	0.002	0.2	0.05

Fig. 11. Simulation of the pressure evolution in a single evolving fracture, nucleated at the centre of a grid of size 200 × 20 at time $t = 0$. For all cases a uniform breaking threshold, T_C was used. In each column, two cells are highlighted in colour, indicating that the simulations differed only in the highlighted parameter. (For interpretation of the references to colour in this figure legend, the reader is referred to the web version of this article.)

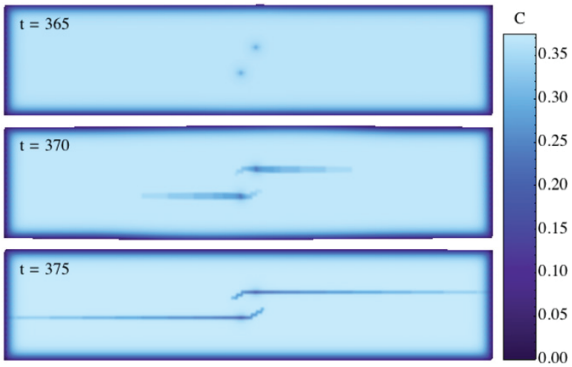

Fig. 12. Simulation of the interaction between two initially parallel fractures on a grid of size 150 × 40 with parameters $\kappa = 0.0025$ $\alpha = 4.0$, $\beta = 0.025$, $\gamma = 0.001$ and $k^S = 10^{-3}$. T_C was normally distributed, with $\langle T_C \rangle = 0.1$ and $\mathrm{std}(T_C) = 0.01$. The colour indicates the concentration of dissolved gas. (For interpretation of the references to colour in this figure legend, the reader is referred to the web version of this article.)

to the boundary, they were able to drain the system sufficiently to prevent activation of other fractures. The examples in Figs. 15 and 16 show an important feature of the system, namely that fractures not only interact by elastic coupling, but also communicate through their effect on the concentration field. The relative importance of these two interaction mechanisms depends on the various model parameters.

It is known from natural systems that propagating fracture tips tend to connect with existing fractures at right angles (see for example Refs. [40–42]). In Figs. 13–16 propagating tips do tend to turn towards nearby fractures, but not always, and sometimes the intersection is not orthogonal. To explain this discrepancy, it should be kept in mind that fracture tips in this model are restricted to propagate along 12 directions, which limits how abruptly they can turn. In the cases where the fractures do intersect orthogonally, the pressure in nearby fractures was high, such that its stress field could affect the approaching fracture from afar and the tip had a long distance over which to make the turn. In cases where tips did not turn,

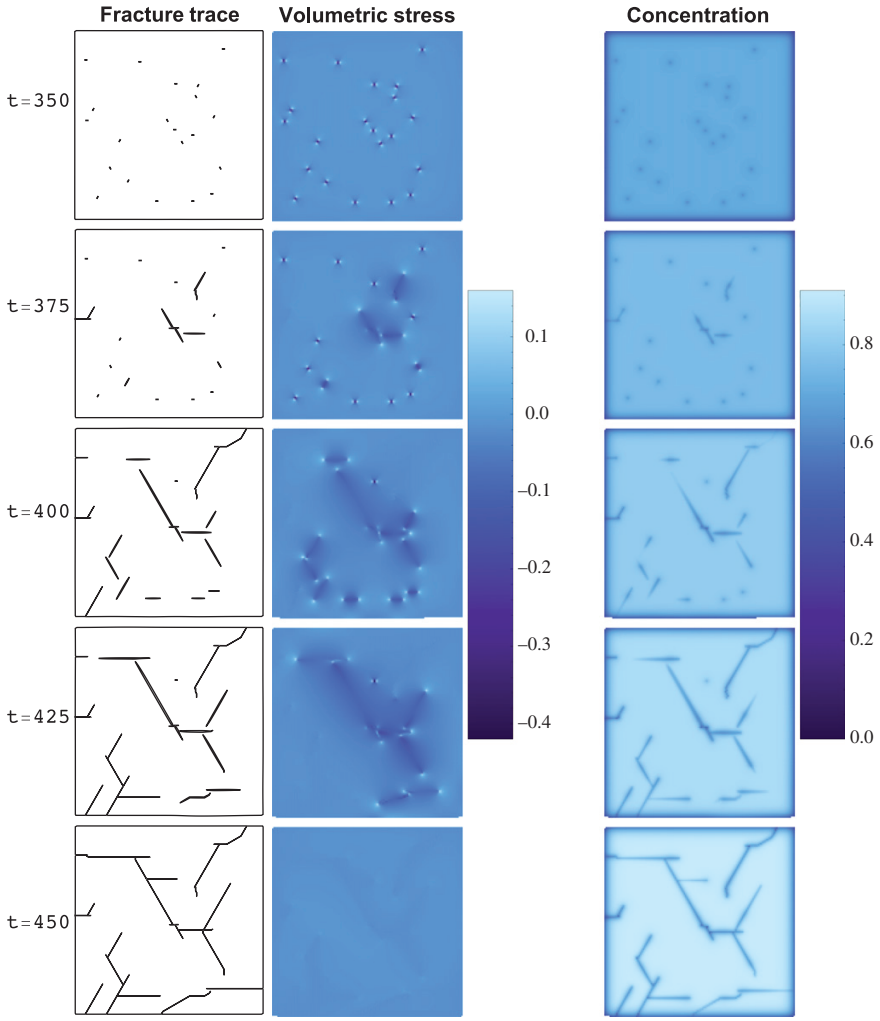

Fig. 13. Simulation with 20 fracture seeds on a quadratic grid of side length $L = 90$, showing the evolution of the fractures, volumetric stress field and concentration field. System parameters: $\kappa = 0.005$, $\alpha = 8.0$, $\beta = 0.005$, $\gamma = 0.002$, $k^S = 10^{-2}$ and $T_C = 0.1$. The initial seeds are identical to those used in the simulations illustrated in Figs. 14–16.

they were typically incident on external boundaries or deflated fractures, such that the stress field at the tip was dominated by the contribution from the propagating fracture itself until it intersected the other fracture. With better spatial resolution, we expect that these intersections would be orthogonal.

4. Discussion

The purpose of the previous sections was to motivate, describe and define a new DEM model, and point out its strengths and weaknesses. In our opinion, the main advantage of the model is that fracture volumes and surfaces are naturally represented in terms of the computational mesh. This makes it easy to keep track of fluid volumes and to impose fluid pressure on fracture walls. The model is particularly suitable for simulating very low permeability systems in which free fluid is confined to fracture apertures by large capillary forces and/or by very low permeabilities such that pressure forces can be treated as boundary forces acting on fracture surfaces. An additional benefit of the model is that the fracture shapes are realistic, even for small fracture apertures and for fractures that do not follow a particular lattice direction. In particular, straight fractures may be represented, even at the scale of individual elements. The stress field around fractures is well approximated by the model, even at crack tips and with low mesh resolution.

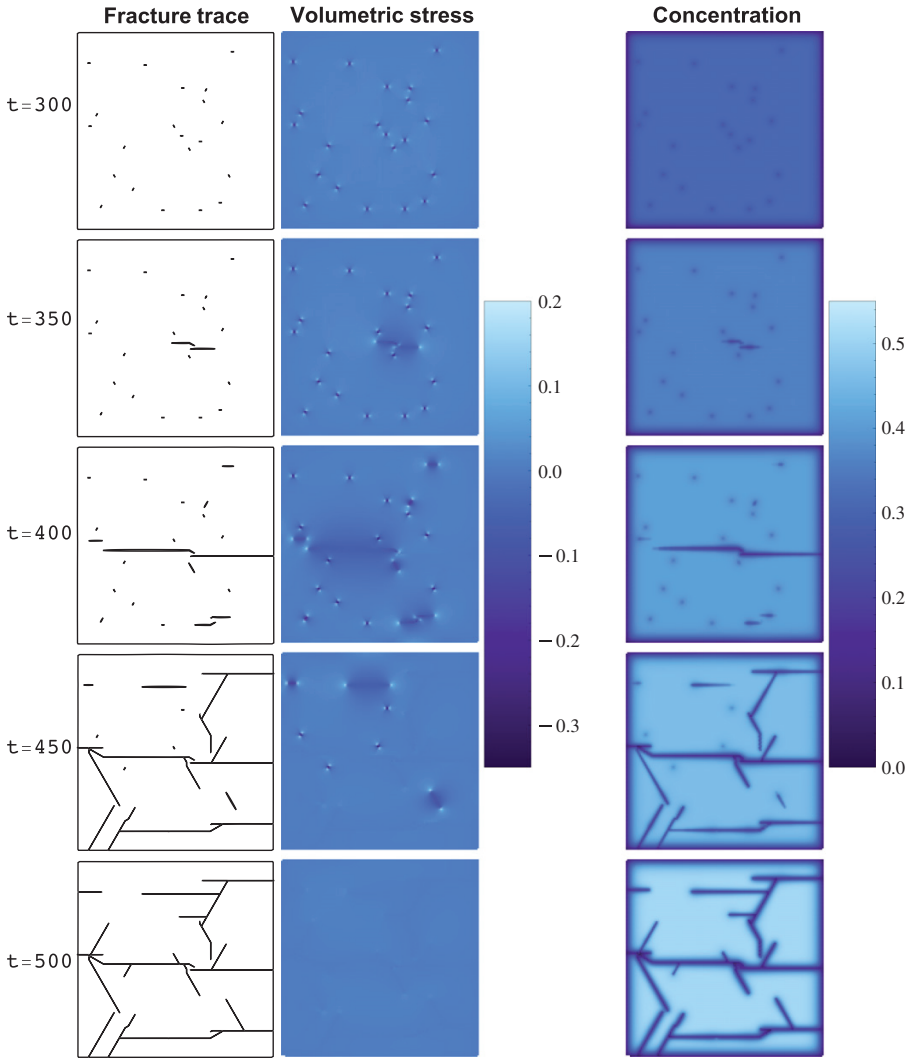

Fig. 14. Simulation with 20 fracture seeds on a quadratic grid of side length $L = 90$, showing the evolution of the fractures, volumetric stress field and concentration field. System parameters: $\kappa = 0.005$, $\alpha = 8.0$, $\beta = 0.025$, $\gamma = 0.001$, $k^S = 10^{-2}$, $\langle T_C \rangle = 0.1$ and $\mathrm{std}(T_C) = 0.01$. The initial seeds are identical to those used in the simulations illustrated in Figs. 13, 15 and 16.

The increase in the number of nodes during simulations may appear to be a disadvantage with respect to implementation. However, as we have shown, fracturing causes only local changes to the mesh topology, and the relaxation method used in the model only requires matrix updates when fractures propagate or when new fractures are nucleated. Additionally, although the number of nodes increases during simulations, the number of triangular material elements is conserved. By scaling the spring forces according to the Voronoi surfaces between nodes, and by splitting these into element-wise contributions, inter-nodal forces are appropriately re-distributed after node splitting, without the need to adjust any springs. In principle it should be possible to speed up the matrix updating further by preallocating memory for extra nodes in vectors and matrices. Updates could then be accomplished by simply subtracting and adding elements at appropriate indices, eliminating the need to reassemble entire matrices. This should allow for matrix updates with efficiency similar to traditional DEM models.

The idea of introducing fractures by splitting nodes can in principle be generalised to three-dimensional systems. The extra book-keeping required for reconnecting the mesh and inserting fracture elements upon fracturing seems to be the major complication. Two methods for representing fractures in the two-dimensional model were suggested. The first method,

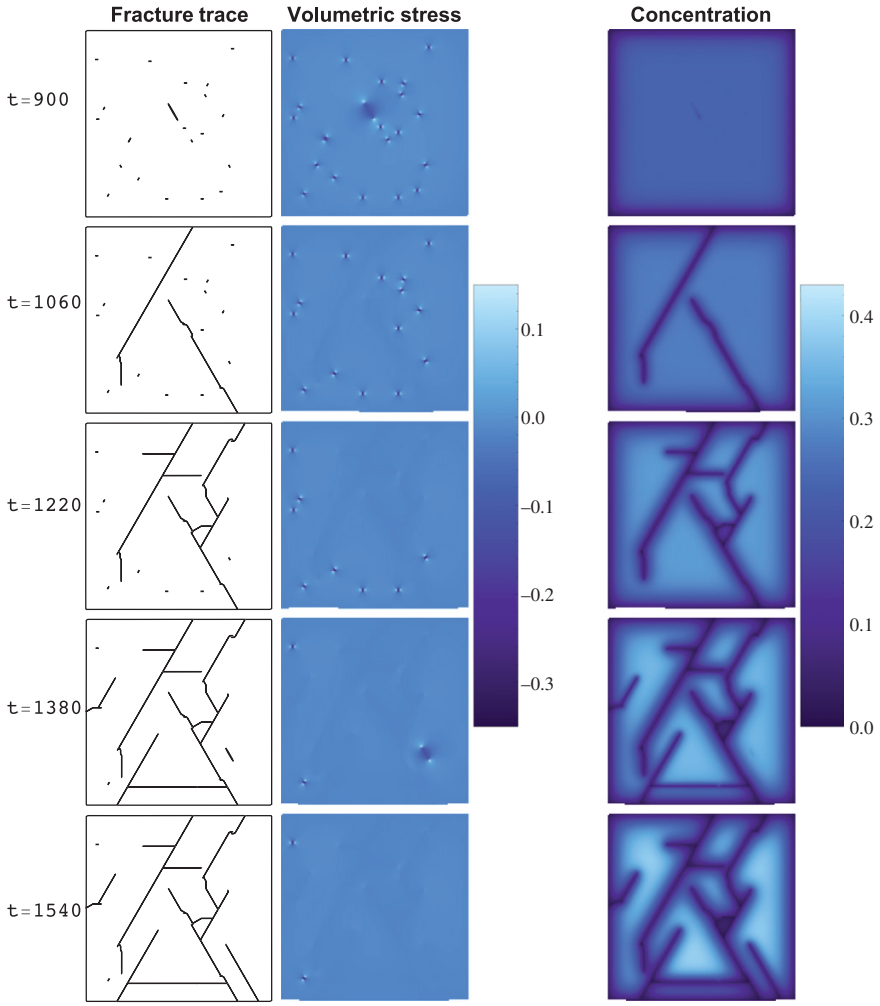

Fig. 15. Simulation with 20 fracture seeds on a quadratic grid of side length $L = 90$, showing the evolution of the fractures, volumetric stress field and concentration field. System parameters: $\kappa = 0.01$, $\alpha = 2.0$, $\beta = 0.05$, $\gamma = 0.00025$, $k^S = 10^{-2}$, $\langle T_C \rangle = 0.1$ and $\mathrm{std}(T_C) = 0.01$. The initial seeds are identical to those used in the simulations illustrated in Figs. 13, 14 and 16.

which identifies fracture walls with the interfaces of the computational mesh, is directly transferable to three dimensions. The second approach, which uses a projection of the surface obtained by the first approach, requires some modification in order to work in three dimensions, because the surface associated with each node will be defined in terms of more than two points, (i.e. points half way between the node and each of its neighbours on the fracture surface) and these points are not necessarily coplanar. A solution to this problem would be to introduce an additional auxiliary point, for example the mean of the other points defining the surface element, in order to triangulate fracture surfaces. Such an approach may reduce lattice artefacts in three-dimensional DEM models. Despite being slightly more complicated, the projection method produces fractures that are smoother than those achieved with the other method. Since it also ensures that the transport coupling is independent of grid direction, we believe that the projection method is the superior of the two approaches.

There are many ways in which the DEM model presented here could be modified for various applications. More complex inter-nodal forces could be implemented, for example by adding bending and torsional forces, or by using a different grid. Mechanical elements with properties such as creep, strain hardening and plastic deformation could also be used. To study fast processes a fully dynamic implementation, in which masses are assigned to the nodes and the system is evolved by numerically solving Newton's second law of motion, could be used, instead of using a quasi-static relaxation approach. Different fracturing criteria, such as a Mohr–Coulomb criterion for compressive and shear fractures, could also be used. This could easily be implemented for the fluid pressure-driven fracturing application discussed in this paper, however, an

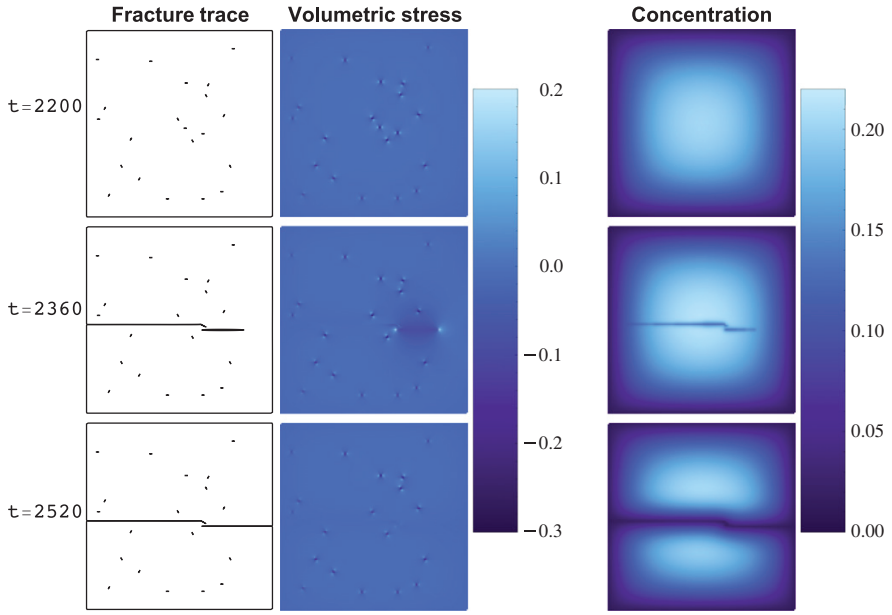

Fig. 16. Simulation with 20 fracture seeds on a quadratic grid of side length $L = 90$, showing the evolution of the fractures, volumetric stress field and concentration field. System parameters: $\kappa = 0.005$, $\alpha = 2.0$, $\beta = 0.025$, $\gamma = 0.0005$, $k^S = 10^{-2}$, $\langle T_C \rangle = 0.1$ and $\mathrm{std}(T_C) = 0.01$. The initial seeds are identical to those used in the simulations illustrated in Figs. 13–15.

appropriate method for dealing with the closure of fractures and the shear forces between closed fracture surfaces would be required. This could be achieved by using a collision-detection algorithm and imposing penalty forces to restrict overlap of fracture and bulk elements. Anisotropy in elastic properties or composite materials could be modelled by defining spring constants and material strength individually for either nodes, springs or triangular elements. Dynamic adjustment of spring equilibrium lengths would be a method for incorporating local material contraction or expansion, for example in response to volume-changing chemical reactions with the fluid. With regard to fluid transport, it might be possible to couple the DEM model with more advanced flow models, for example by decomposing fracture triangles into a finer mesh. A simple modification to the current model would be to solve fracture flow as a pressure diffusion process on the triangular fracture elements. Fracturing driven by fluids that do not obey the ideal gas equation of state could also be simulated. For example, incompressible fluids may be modelled by imposing conservation of fracture volumes during relaxation (similar to Ref. [37]).

To conclude, we believe that the model presented here addresses some of the challenges related to the modelling of coupled processes of fluid transport, deformation and fracturing.

Acknowledgements

This work was supported by the Norwegian Research Council, through the Petromaks project (grant number 193186/E30) and a Center of Excellence grant to the Physics of Geological Processes Center (PGP) (grant number 142042).

References

[1] Hydraulic Fracturing, Association of American State Geologists, 2012, URL: http://www.stategeologists.org/fact_sheet.php.
[2] The Future of Natural Gas, Massachusetts Institute of Technology Energy Initiative, 2011, URL: http://mitei.mit.edu/publications/reports-studies/future-natural-gas.
[3] B.P. Tissot, D.H. Welte, Petroleum Formation and Occurrence: A New Approach to Oil and Gas Exploration, Springer-Verlag, New York, NY, 1978.
[4] R.R. Berg, A.F. Gangi, Primary migration by oil-generation microfracturing in low-permeability source rocks: application to the Austin Chalk, Texas, AAPG Bulletin 83 (1999) 727–756.
[5] P.D. Bons, B.P. van Milligen, New experiment to model self-organized critical transport and accumulation of melt and hydrocarbons from their source rocks, Geology 29 (2001) 919–922.
[6] F. Quattrocchi, In search of evidence of deep fluid discharges and pore pressure evolution in the crust to explain the seismicity style of the Umbria–Marche 1997–1998 seismic sequence (Central Italy), Ann. Geofis. 42 (1999) 609–636.
[7] S.A. Miller, C. Collettini, L. Chiaraluce, M. Cocco, M. Barchi, B.J. Kaus, Aftershocks driven by a high-pressure CO_2 source at depth, Nature 427 (2004) 724–727.
[8] R.D. McIver, Role of naturally occurring gas hydrates in sediment transport, AAPG Bull. 66 (1982) 789–792.
[9] J.H. Davies, The role of hydraulic fractures and intermediate-depth earthquakes in generating subduction-zone magmatism, Nature 398 (1999) 142–145.

[10] T. Kutty, K. Chandrasekharan, J. Panakkal, J. Ghosh, Fracture toughness and fracture surface energy of sintered uranium dioxide fuel pellets, J. Mater. Sci. Lett. 6 (1987) 260–262.
[11] Z. Fan, Z.-H. Jin, S. Johnson, Subcritical propagation of an oil-filled penny-shaped crack during kerogen–oil conversion, Geophys. J. Int. 182 (2010) 1141–1147.
[12] E. Gundersen, E. Flekkøy, K. Bjørlykke, J. Feder, B. Jamtveit, Fracture spacing during hydro-fracturing of cap-rocks, Geofluids 11 (2011) 280–293.
[13] Z. Fan, Z.-H. Jin, S. Johnson, Gas-driven subcritical crack propagation during the conversion of oil to gas, Pet. Geosci. 18 (2012) 191–199.
[14] Z. Fan, Z.-H. Jin, S. Johnson, Modelling petroleum migration through microcrack propagation in transversely isotropic source rocks, Geophys. J. Int. 190 (2012) 179–187.
[15] Z.-Q. Fan, Z.-H. Jin, S.E. Johnson, Subcritical crack propagation and coalescence induced by the oil–gas transformation, in: 13th International Conference on Fracture, 2013.
[16] J. Oliyer, Continuum modelling of strong discontinuities in solid mechanics using damage models, Comput. Mech. 17 (1995) 49–61.
[17] J. Dolbow, T. Belytschko, A finite element method for crack growth without remeshing, Internat. J. Numer. Methods Engrg. 46 (1999) 131–150.
[18] N. Sukumar, N. Moës, B. Moran, T. Belytschko, Extended finite element method for three-dimensional crack modelling, Internat. J. Numer. Methods Engrg. 48 (2000) 1549–1570.
[19] G. Wells, L. Sluys, A new method for modelling cohesive cracks using finite elements, Internat. J. Numer. Methods Engrg. 50 (2001) 2667–2682.
[20] I. Aranson, V. Kalatsky, V. Vinokur, Continuum field description of crack propagation, 2000. ArXiv Preprint, cond-mat/0001298.
[21] A. Karma, D.A. Kessler, H. Levine, Phase-field model of mode III dynamic fracture, Phys. Rev. Lett. 87 (2001) 045501.
[22] L.O. Eastgate, J.P. Sethna, M. Rauscher, T. Cretegny, C.-S. Chen, C.R. Myers, Fracture in mode I using a conserved phase-field model, Phys. Rev. E 65 (2002) 036117.
[23] H. Henry, H. Levine, Dynamic instabilities of fracture under biaxial strain using a phase field model, Phys. Rev. Lett. 93 (2004) 105504.
[24] P. Meakin, A simple model for elastic fracture in thin films, Thin Solid Films 151 (1987) 165–190.
[25] T. Walmann, A. Malthe-Sørenssen, J. Feder, T. Jøssang, P. Meakin, H. Hardy, Scaling relations for the lengths and widths of fractures, Phys. Rev. Lett. 77 (1996) 5393–5396.
[26] A. Malthe-Sørenssen, T. Walmann, J. Feder, T. Jøssang, P. Meakin, H. Hardy, Simulation of extensional clay fractures, Phys. Rev. E 58 (1998) 5548–5564.
[27] A. Royne, B. Jamtveit, J. Mathiesen, A. Malthe-Sørenssen, Controls on rock weathering rates by reaction-induced hierarchical fracturing, Earth Planet. Sci. Lett. 275 (2008) 364–369.
[28] F. Kun, H.J. Herrmann, A study of fragmentation processes using a discrete element method, Comput. Methods Appl. Mech. Engrg. 138 (1996) 3–18.
[29] F. Kun, H.J. Herrmann, Transition from damage to fragmentation in collision of solids, Phys. Rev. E 59 (1999) 2623–2632.
[30] A. Malthe-Sørenssen, B. Jamtveit, P. Meakin, Fracture patterns generated by diffusion controlled volume changing reactions, Phys. Rev. Lett. 96 (2006) 245501.
[31] E. Aker, H. Khoa, F. Cuisiat, M. Soldal, Acoustic emission experiments and microcrack modelling on porous rock, in: EAGE Passive Seismic Workshop-Exploration and Monitoring Applications, 2009.
[32] J. Bolander, S. Saito, Fracture analyses using spring networks with random geometry, Eng. Fract. Mech. 61 (1998) 569–591.
[33] J. Bolander Jr., G. Hong, K. Yoshitake, Structural concrete analysis using rigid-body-spring networks, Comput.-Aided Civ. Infrastruct. Eng. 15 (2000) 120–133.
[34] L. Monette, M. Anderson, Elastic and fracture properties of the two-dimensional triangular and square lattices, Modelling Simul. Mater. Sci. Eng. 2 (1994) 53–66.
[35] E.G. Flekkøy, A. Malthe-Sørenssen, B. Jamtveit, Modeling hydrofracture, J. Geophys. Res. 107 (2002) 2151. (ECV 1-1–ECV 1-11).
[36] F. Tzschichholz, M. Wangen, Modellization of hydraulic fracturing of porous materials, 2001. ArXiv Preprint, cond-mat/0101369.
[37] M. Wangen, Finite element modeling of hydraulic fracturing on a reservoir scale in 2D, J. Petrol. Sci. Eng. 77 (2011) 274–285.
[38] M. Kobchenko, A. Hafver, E. Jettestuen, O. Galland, F. Renard, P. Meakin, B. Jamtveit, D.K. Dysthe, Drainage fracture networks in elastic solids with internal fluid generation, Europhys. Lett. 102 (2013) 66002.
[39] S. Bohn, S. Douady, Y. Couder, Four sided domains in hierarchical space dividing patterns, Phys. Rev. Lett. 94 (2005) 0545503.
[40] S. Bohn, L. Pauchard, Y. Couder, Hierarchical crack pattern as formed by successive domain divisions. I. Temporal and geometrical hierarchy, Phys. Rev. E 71 (2005) 046214.
[41] S. Bohn, J. Platkiewicz, B. Andreotti, M. Adda-Bedia, Y. Couder, Hierarchical crack pattern as formed by successive domain divisions. II. From disordered to deterministic behavior, Phys. Rev. E 71 (2005) 046215.
[42] Y. Cohen, J. Mathiesen, I. Procaccia, Drying patterns: sensitivity to residual stresses, Phys. Rev. E 79 (2009) 046109.
[43] M.P. Allen, D.J. Tildesley, Computer Simulation of Liquids, Oxford University Press, 1989.
[44] H.M. Westergaard, Bearing pressures and cracks, J. Appl. Mech. 6 (1939) 49–53.
[45] I. Sneddon, The distribution of stress in the neighbourhood of a crack in an elastic solid, Proc. R. Soc. A 187 (1946) 229–260.

Paper VI:

Evolution of a fracture network in an elastic medium with internal fluid generation and expulsion

M. Kobchenko, A. Hafver, E. Jettestuen, F. Renard, O. Galland, B. Jamtveit, P. Meakin and D.K. Dysthe

Manuscript in press, Physical Review E

Evolution of a fracture network in an elastic medium with internal fluid generation and expulsion

Maya Kobchenko,[1] Andreas Hafver,[1] Espen Jettestuen,[1] François Renard,[1, 2, 3] Olivier Galland,[1] Bjørn Jamtveit,[1] Paul Meakin,[1, 4] and Dag Kristian Dysthe[1]

[1] *Physics of Geological Processes, University of Oslo, Norway*
[2] *Univ. Grenoble Alpes, ISTerre, BP 53, F-38041, Grenoble, France*
[3] *CNRS, ISTerre, BP 53, F-38041, Grenoble, France*
[4] *Department of Physics, Temple University, USA*

(Dated: October 15, 2014)

A simple and reproducible analog experiment was used to simulate fracture formation in a low-permeability elastic solid during internal fluid/gas production, with the objective of developing a better understanding of the mechanisms that control the dynamics of fracturing, fracture opening and closing and fluid transport. In the experiment, nucleation, propagation and coalescence of fractures within an elastic gelatin matrix, confined in a Hele-Shaw cell, occurred due to CO_2 production via fermentation of sugar, and it was monitored by optical means. We first quantified how a fracture network develops, and then how intermittent fluid transport is controlled by the dynamics of opening and closing of fractures. The gas escape dynamics exhibited three characteristic behaviors: 1) Quasi periodic release of gas with a characteristic frequency that depends on the gas production rate but not on the system size. 2) A $1/f$ power spectrum for the fluctuations in the total open fracture area over an intermediate range of frequencies (f), which we attribute to collective effects caused by interaction between fractures in the drainage network. 3) A $1/f^2$ power spectrum was observed at high frequencies, which can be explained by the characteristic behavior of single fractures.

I. INTRODUCTION

In general, the formation of fracture networks in the rocks of the Earth's crust is driven by a combination of external stress applied at the boundaries of a system, stress generated inside the system and stress generated by gravitational body forces. Under some circumstances one of these sources of stress may be dominant. Natural hydraulic fractures can form inside a rock matrix due to internal fluid pressure build-up [1, 2]. Fluid pressure build-up may have various origins including: the compaction of the rock matrix in sedimentary basins that may trap fluids in overpressured reservoirs [3]; the compaction of gouge in fault zones [4]; magma emplacement and rapid heating of either water (phreatic explosions) or organic-rich rocks [5]; or the partial melting of minerals [6]. The internal fluid pressure can also be generated by chemical reactions which produce fluid in a tight rock matrix. The reaction-induced fracturing of low-permeability rocks during hydrocarbon generation in organic-rich shales during diagenesis [3] is an important example. In these systems, the fracture network develops in response to internal pressure generation and the resulting fracture pattern is therefore the consequence of energy dissipation at various scales in the rock body. In the present study, our goal is to better understand the spatio-temporal coupling between elastic matrix deformation, fracture generation and fluid transport.

Visualizing the coupling between fluid pressure build-up and the fracturing processes is important. X-ray micro-tomography can be used to visualize and analyze the three-dimensional morphology of fractures produced experimentally in rocks [7, 8]. The capability of investigating rock deformation and fracturing under a wide range of thermodynamic conditions (temperature, pressure) with in-situ X-ray imaging is also under development. Examples include imaging of microcracks forming during heating of shales [9], investigation of the dehydration of gypsum during heating [10] and the generation of magmatic melt in oceanic olivine-rich rocks [11]. In such studies, obtaining high temporal and spatial resolutions, under the thermodynamic conditions where the process occurs, is technically challenging, and the amount of data that can be collected is smaller than that which can be obtained under room temperature and pressure conditions. Moreover, the micro-tomography technique does not yet allow fast data acquisition for geomaterials because of their high absorption of X-rays. Other experimental techniques that enable fracturing to be investigated at high temporal and spatial resolutions are therefore complementary to X-ray tomography and in-situ studies.

To study fracture formation processes, experiments using materials analogous to rocks, such as elastic gels, clay, plasticine or sand, are widely used [12–14]. With such analog systems, the accumulation and transport of fluid, as well as hydraulic-fracture propagation, has been studied [15–18]. In all but one study, fluid was injected at a single point. Bons and van Milligen [12] simulated homogeneous gas production, by using CO_2 produced by the yeast mediated fermentation of sugar. In their experiment, sand was used as the host matrix. Sand behaves as a brittle solid during fracture formation, but grain flow occurs when fractures are reactivated after healing. This system was designed to model the transport of melt within rock. Bons and van Milligen [12] found that the power spectrum for the fluctuations in the volume of trapped gas, exhibited a $1/f$ frequency dependence at low frequencies (f) and as $1/f^2$ behavior at high frequencies. The authors argued that the system exhibited

self-organized criticality and long range memory effects.

Dahm [16] observed the propagation of hydraulic fractures that open at one end and close at the other end, providing pathways for fluid expulsion. The intermittent character of fluid transport in time and space was also observed in the experiments of Bons and van Milligen [12], and the texture of the minerals in natural calcite veins has been interpreted in terms of a crack-seal process with several generations of fracture opening [19]. However, the intermittency of this fracture opening and closing process could not be studied in-situ. In low permeability rocks, the opening, closing and healing of fractures may be the dominant fluid transport mechanism during compaction and fluid expulsion. In some systems, phenomena such as episodic fluid expulsion [20] and porosity waves [21] are also controlled by these processes.

In a previous study [18] a laboratory experiment, in which the fracture patterns generated by homogeneous gas production inside a thin elastic gelatin layer could be analyzed, served as a model system for fracturing driven by fluid generation in brittle rocks. Here, we describe an investigation in which the dynamics of 2D fracture nucleation, growth and coalescence was monitored and analyzed until a fracture network occupied the entire system. As time elapsed, the internally produced gas escaped from the fractures, which became partially healed. When the gas pressure increased again, the same fractures were reactivated and served as pathways for gas discharge. The dynamics of fractures opening, closing and interaction with neighboring fractures was recorded using optical imaging and quantified. Our main objective was to characterize how fractures initiate, grow, and coalesce, and how the produced gas is expelled from the system.

II. MATERIALS AND METHODS

II.1. Experimental set-up

We studied experimentally the accumulation, segregation, and escape of fluid from an impermeable solid, in a model system for the fracturing of organic-rich shales during hydrocarbon production [9]. A quasi two-dimensional elastic gelatin layer, in a Hele-Shaw cell with open boundaries was used to simulate an almost impermeable shale rock. CO_2 gas was produced by yeast mediated fermentation of sugar (sucrose) in the bulk of the gelatin matrix. The transparency of gelatin enabled high resolution, high contrast optical imaging and monitoring of fracture formation during CO_2 production. Although the gelatin medium does not reproduce the complexity of heterogeneous shales, it does reproduce several basic features of the fracturing process.

The Hele-Shaw cell consisted of two 10 mm thick glass plates clamped together and separated by 3 mm (Figure 1A). A white light source and photo- and video-cameras (AF-S Nikkor 18-70 mm, and DX lens on Nikon D300) were used to record the fracturing process. The

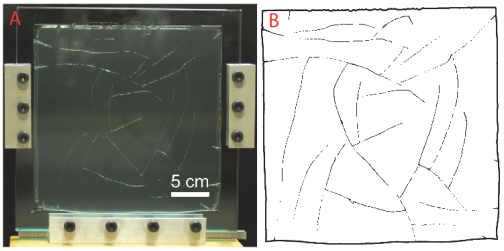

FIG. 1. **A:** (Color online) The Hele-Shaw cell consisted of two parallel 10 mm thick glass plates separated by a 3 mm wide gap that was filled with a layer of gelatin. The boundaries in the lateral directions were free of confinement and the generated gas could escape only through them. The Hele-Shaw cell stood vertically, and back lighting was used to illuminate the fracture pattern. **B:** Thresholded image of a fracture pattern recorded during experiment D (see Table I).

preparation protocol consisted of cleaning the inner surfaces of the Hele-Shaw cell before filling it with an aqueous gelatin gel (cross-linked collagenous polymers) to ensure maximum filling and adhesion of the gelatin to the glass plates. A rubber strip was placed between two glass plates, along their edges, for sealing purposes while the gel was solidifying. The sealing rubber strip was removed at the beginning of each experiment.

II.2. Materials

Dry sheets of gelatin (from Gelita) were soaked in water ($20°C$) for 5-7 min and then mixed with hot water ($100°C$) until they were completely dissolved. The same gelatin concentration was used in all experiments: 58 g of gelatin sheets per 1 dm^3 of water. Sugar was added to the hot gelatin mixture and dissolved. The gelatin and sugar mixture was then cooled to $30°C$, and mixed with fresh baking yeast while the gelatin/sugar/water mixture was still liquid, to ensure homogeneous dispersion. The liquid gelatin-yeast mixture was poured into the Hele-Shaw cell, and kept in a refrigerator ($6°C$) in a vertical orientation until the gel solidified (approximately 2 h). After the gelatin had solidified, the Hele-Shaw cell was placed in a horizontal orientation and kept for 10 h in the refrigerator, in order to obtain a homogeneous elastic gelatin matrix.

II.3. Experimental protocol

The experiments were conducted at 17°C, and under these conditions the gelatin was transparent, brittle and nearly elastic. The rheological properties of gelatins have been studied in detail [22] and application of this material as a rock analog has been proposed [13]. Inversion and fermentation of the dissolved sugar by yeast enzymes

produced CO_2. For each experiment, half of the gel was poured into a bottle, to measure the gas production rate using a simple volumeter system (Figure 2A).

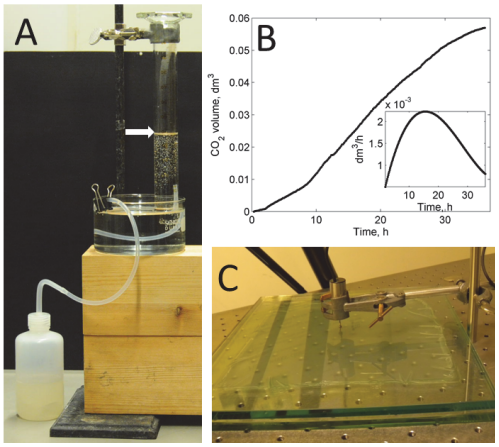

FIG. 2. **A:** (Color online) Volumeter system to measure CO_2 production rate. Gas generated in the gelatin-filled bottle is transported inside a closed glass tube filled with water. The variation of water level (arrow) indicates the amount of produced gas. **B:** CO_2 production measured using the volumeter system. Data correspond to an experiment with reference concentration of yeast and sugar x1. Inset shows the calculated rate of gas production. **C:** LVDT transducer is used to measure the out of plane movement of the Hele-Shaw cell glass plates relative to each other.

TABLE I. List of experiments and conditions. The yeast and sugar concentrations are given in Table II. Δt is the time resolution of the images.

Exp.	System size	Yeast+sugar	Δt	Duration
A	32x32 cm	x1	60 s	16 h 21 min
B	25x25 cm	x1	15 and 60 s	14 h 53 min
			video 15 fps	6 h 55 min
C	12x12 cm	x1	60 s	29 h 25 min
D	25x25 cm	x1	60 s	72 h 26 min
E	25x25 cm	2x1	15 s	36 h 16 min
F	25x25 cm	x1/2	15 s	92 h 55 min

Six experiments were conducted under different conditions (see summary in Table I and Supplementary Material for the experiment D). Two main parameters were varied: the system size (the lateral dimensions of the gelatin filled Hele-Shaw cell) and the concentrations of yeast and sugar. The duration of experiment D was longer than the durations of experiments A, B and C, to investigate the influence of gas production variation. In experiments A-E, fracturing was observed, but in experiment F the gas production was not sufficient to cause fracturing. Experiments B and D were performed under identical conditions, to test for reproducibility.

TABLE II. Variation of gas production.

Concentration	x1/2	x1	x2
Amount of yeast (g/dm^3)	1.25	2.5	5
Amount of sugar (g/dm^3)	3.75	7.5	15
CO_2 production rate (cm^3/h)	0.4	1.6	6.2

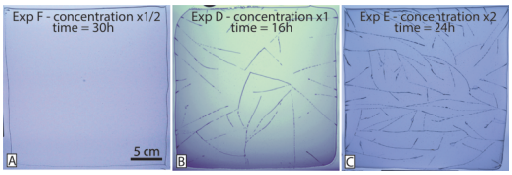

FIG. 3. (Color online) Variation of gas production rate in three experiments with the same system size. Snapshots are shown at a late stage after which no new fractures appeared. **A:** In Experiment F, the gas production rate was very slow, no fractures were observed and, gas was transported out of the Hele-Shaw cell by diffusion. **B:** In experiment D, the developed fracture pattern had a medium fracture density. **C:** In experiment, E the fully developed fracture pattern was very dense.

Fracture nucleation and propagation was monitored by taking images consisting of 4300×2800 pixels with 0.1 mm resolution with a time interval of $\Delta t = 15 - 60$ s. At the same time, in experiment B, video was recorded at a rate of 15 fps, in order to resolve the fast processes of fracture collapse and gas escape. The recording was stopped when the fracture nucleation rate became very small.

A picture of the unfractured gelatin was taken as a reference image. The reference image was subtracted from all subsequent images to correct for the background lighting. The same threshold value was used to convert the images into binary form (0 or 1) (Figure1B). Pixels with a value of 0 (white color) on the binary images correspond to unfractured gelatin matrix, while pixels with a value equal to 1 (black color) correspond to fractured sites. Additional experiments were conducted using cross-polarizers to image the elastic strain field at the fracture tips, since gelatin is a photoelastic material (Figure 4).

III. DEVELOPMENT OF A FRACTURE NETWORK

III.1. Nucleation and development of fractures

In all experiments, the gas production rate increased steadily from zero, reached a maximum after several hours and then decreased (inset of Figure 2B). All measurements were conducted when the gas production rate was relatively high, i.d. in the interval $t = 8 - 30$ h. The average production rates for these periods are given in Table II. We assume that CO_2 was produced homoge-

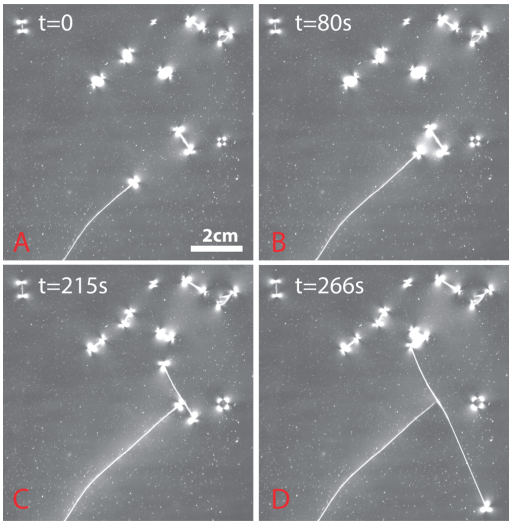

FIG. 4. (Color online) Time-lapse strain field imaged using cross-polarizers. The photo-elastic property of the gelatin enabled the observation of elastic stress concentration at the fracture tips and interactions between fractures. Dark color indicates low stress and light color correspond to high stress.

neously throughout the gelatin layer during the experiments. CO2 is produced by individual yeast cells, which are well dispersed in the gel. Because the permeability of the gel polymer network is extremely low, CO_2 was transported by molecular diffusion in the unfractured gelatin. As gas production increased, small volumes of gas accumulated randomly as bubbles. CO_2 diffused from the surrounding matrix into these bubbles, which grew and transformed into cracks. The first fracture typically nucleated $1-3$ h after the start of the experiment (Figure 5A). After nucleation, cracks began to propagate (Figure 5B), while new cracks were formed. The fractures propagated in both directions until they reached the free boundary (the perimeter of the gelatin layer (Figure 1A)) or another fracture, and if a fracture reached the open boundary gas escaped from the fracture. When one fracture reached another fracture, they coalesced and the strain field at the fracture tip decreased to a value of essentially zero (Figure 4). The pressure inside the fracture dropped, and the fracture aperture collapsed when gas escaped from a fracture. When a fractured closed, the fractured pixels disappeared from the image and the closed fracture is indicated by a dashed line in Figure 5C. Diffusion of gas into a closed fracture reopened the fracture, and as a result the fracture pixels reappeared, and the fractures could be seen as continuous lines in the digital images. The fracture opening and closing was quasi-periodic, as shown below.

The adhesion of the gel to the surface of the glass walls of the Hele-Shaw cell caused resistance to movement of

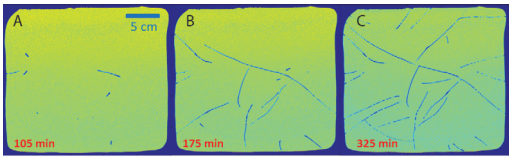

FIG. 5. (Color online) Time-lapse images of fracture formation in experiment B. Dark pixels correspond to the fractured sites. **A**: As yeast produced CO_2, gas accumulated in bubbles, which nucleated randomly in the gelatin layer, fractures began propagating. **B**: Fractures grew and propagated until coalescence. **C**: Coalesced fractures formed a network which provided pathways for fluctuating flow of CO_2 to the open boundaries, and the fractures opened and closed over time.

the gel relative to the glass plates. When cracks open, new volume is generated in the system, but image correlation analysis [23] showed that no systematic expansion of the gel in the plane of the Hele-Shaw cell occurred. However, by using an LVDT displacement sensor, we found that the glass plates confining the gel moved apart in the direction perpendicular to the plane of the Hele-Shaw cell, allowing the gel to increase in thickness and thus accommodate the generated gas volume. The LVDT measurements can be found in [18].

When a fracture is formed in the gel, the fracture cross-section has a lenticular shape with zero width at the glass plates and a maximum width mid-way between the glass surfaces. In order to open the fracture, a pressure force must be applied on the fracture walls to overcome the elastic resistance. As the pressure in a fracture increases, the fracture aperture increases and the fracture walls become more curved in the plane perpendicular to the glass surfaces and the direction of the fracture. The thickness of the fracture lines on the images represents the maximum widths of fracture openings, and it varied from 0 to 5 pixels. The number of dark pixels in an image corresponds to the projection of the gas filled fracture apertures onto the plane of the Hele-Shaw cell, the number of dark pixels is called *the fracture area*. The variation of the fracture area is used to quantify the dynamics of the fracture network evolution and subsequent fluid expulsion.

III.2. Fracture coalescence

In order to analyze the evolution of fracture networks, fractures must be identified from the moment at which they appear. As an input, the time series of binary images obtained after image analysis was used (Figure 5). The binary images were superimposed from the first up to the current time-step, so that all pixels which belonged to a fracture at any earlier time during the experiment up to the current time were included. In this way a series of images of the continuously developing fracture network was obtained, whether fractures are open or closed (Figure 6). These cumulative fracture patterns include all

the potential pathways for gas drainage.

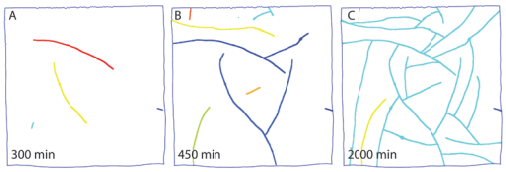

FIG. 6. (Color online) The evolution of the fracture network for experiment D. Connected fractures are indicated by the same color. **A:** New cracks nucleate. **B:** Fractures propagate and coalesce. **C:** Coalesced fractures form large connected pathway for outgoing gas.

During the early stage of an experiment, the number of pixels, which measured the fracture area, grew monotonically with increasing time because new fracture pixels were constantly added. During this stage, both the fracture lengths and fracture widths increased. In order to investigate how the fracturing network developed with time, the fracture length was used as a more accurate representation of the growth of the fracture pattern. A skeletonization procedure was applied to the overlapping images to reduce the fracture width to one pixel so that the number of fracture pixels measured the fracture length.

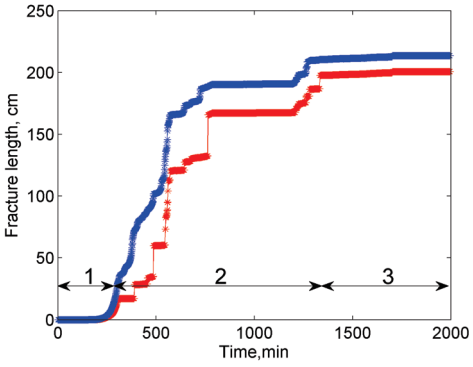

FIG. 7. (Color online) Evolution of the connected fracture pathway in experiment D. **Blue (upper) curve:** Temporal evolution of the total length of all connected fractures. **Red (lower) curve:** Temporal evolution of the largest connected fracture pathway. The abrupt staircase-like increases in the total fracture length corresponds to fracture coalescence events. The three regimes 1,2,3 are described in the text.

Figure 7 shows the evolution of the total length of all accumulated fractures with time (blue curve). Three regimes of fracture growth can be distinguished. In the first regime, fractures were nucleated and grew slowly. In the second regime existing fractures grew rapidly and new ones appeared. In the third regime there was little or no fracture growth.

Overlapping binary images were used to extract and analyze connected fractures. A label was assigned to every fracture, and they are indicated by different colors in Figure 6. The analysis of the fully developed stationary fracture pattern was performed in another study [18]. Here we use the fracture labeling and information about fracture connectivity to analyze the spatial correlation of gas drainage dynamics.

As fractures propagated, they coalesced and formed connected clusters (Figure 6C). Initially, the length of the largest connected fracture cluster evolved smoothly. When cracks started to coalesce, the length of the largest cluster increased by discrete increments, producing jumps in the red curve in Figure 7. This dominant cluster drained the largest gelatin area and its evolution dominated the drainage of the whole system.

III.3. Evolution of the total fracture area

Figure 8 shows the time evolution of the total fracture area in the gelatin layer in five distinct experiments (A-E). The number of fracture pixels was scaled by the area of the gelatin layer. Three regimes of fracturing could be distinguished. In the first (fractures nucleation and propagation) regime, the total fracture area increased exponentially. In the second regime some fractures closed while new cracks still appeared and grew in length and width. This regime is characterized by an overall increase in the fracture area with superimposed oscillations. Finally, in the third regime, no new fractures were formed. However, fractures continued to close and reopen, and the number of fracture pixels fluctuated around a slowly varying value.

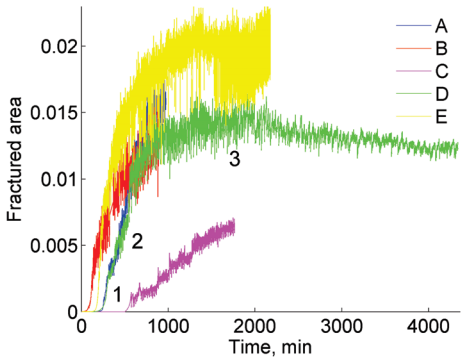

FIG. 8. (Color online) Total fracture area time series for five experiments.

The fluctuation amplitude and the time between fracture opening (fracture area increase) and fracture closing (fracture area decrease) depended on the rate of gas generation in the system as well as on system size. From

Figure 8 it can be seen that after about 2000 min, when the gas production decreased, the fluctuation amplitude in experiment D decreased by a factor of about two. This was cause by significant depletion in CO_2 production.

IV. DYNAMICS OF THE FRACTURE PATTERN

IV.1. Temporal fluctuations of single fractures

In this section, we describe the dynamics of fractures that are not connected to other fractures but have reached the open boundary of the Hele-Shaw cell (Figure 6). The number of these isolated fractures varied in the different experiments. In experiment C, almost all of the fractures were isolated, because of the small size of the system. The inset of Figure 9 shows the variation of the fracture area for one of the isolated fractures from experiment C. A clear periodicity in the fracture area fluctuations can be observed. To extract the low frequency trend from the signal, the original data were smoothed using a median filter. The obtained low-frequency trend (the smoothed signal) was subtracted from the time series and the discrete Fourier transform ($\mid Y(f) \mid$) was calculated using the fast Fourier transform algorithm. The power spectrum ($(\mid Y(f) \mid)^2$) of the signal featured a well-pronounced peak. To determine the peak frequency, the power spectrum was smoothed using a median filter (Figure 9).

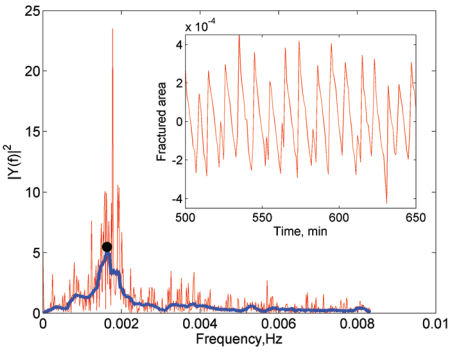

FIG. 9. (Color online) Power spectrum of the fracture area time series for one of the isolated cracks in experiment C. Red (light gray) curve: original data. Blue (dark gray) curve: filtered data. Black dot: peak frequency f_c. **Inset**: Variation of the fracture area for one isolated fracture in the experiment C after a low frequency detrending.

Power spectra of opening/closing fracture area fluctuations were calculated for all isolated fractures in experiments A, B, and C. These three experiments were conducted at the similar gas production rate. Figure 10 shows the distribution of the characteristic frequencies f_{ci}. The characteristic frequency did not depend on fracture length and it was essentially the same for the experiments with different system sizes A, B, and C - $f_{ci} = (1.97 \pm 0.64) \times 10^{-3}$ Hz.

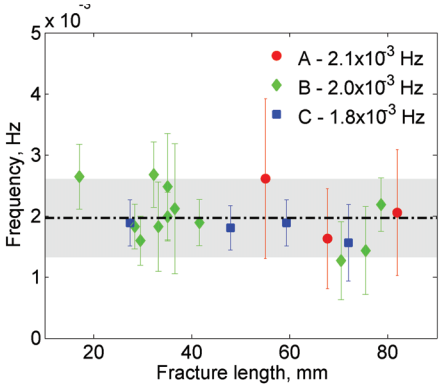

FIG. 10. Characteristic frequencies f_{ci} for isolated fractures in experiments A,B, and C versus length of the fractures l_i. The average characteristic frequency for each experiment is indicated in the upper right corner. The characteristic frequency range is indicated by the dashed line and shaded area on the plot).

The following simple model for periodic fracture opening and closing during homogeneous gas production is proposed to explain this observation. We consider an isolated crack which drains from one end to the open boundary. The rate j at which gas flows into the fracture is proportional to the area of the drainage basin of the fracture $j \propto A$, which is proportional to the product of the fracture length l and the basin width w_b: $A \propto l \times w_b$. In [18] we showed that the typical basin width is constant for a given gas production rate, and therefore the gas flux is proportional to the fracture length, $j \propto l$. The fracture capacity c is proportional to the product of the fracture length l and the average fracture aperture width, w_e, at which gas is expelled from the fracture, and since w_e is also constant $c \propto l$. Gas escape occurs when the amount of gas in the fracture exceeds the fracture capacity. From the relations $j \propto l$ and $c \propto l$, it follows that the time between two escape events (the period of fractured area fluctuations), τ, does not depend on fracture length but only on the rate of gas production per unit area.

IV.2. Single fracture behavior in the high frequency range

High frequency data from experiment B were used to determine the nature of the power spectrum decay in the high frequency range. Figure 11 shows the fracture area fluctuation power spectrum of one of the isolated fractures, and it can be seen that numerical power spectrum is consistent with a $1/f^2$ power frequency relationship at

high frequencies. Similar results were obtained for other isolated fractures.

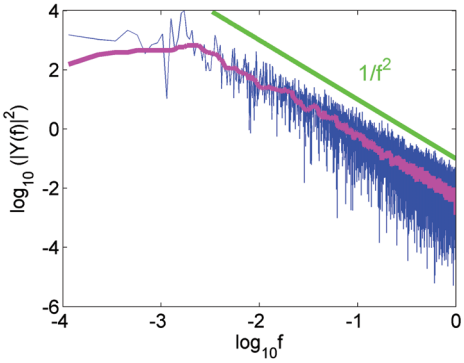

FIG. 11. (Color online) Power spectrum of the area fluctuation of one of the single fractures in the experiment B. Pink (light gray) curve represents power spectrum, smoothed with median filter. The power spectrum varies as $1/f^2$.

IV.3. Temporal fluctuations in the total fracture area

Now, we consider the variations of the total fracture area with time for all experiments (Figure 8). All data were detrended as described above (IV.1). The fluctuation of the total fracture area features different amplitudes and frequencies (Figure 12). To analyze the frequency distribution the fracture fluctuation time series for five experiments (Figure 8) were divided into intervals of equal duration. Each interval was detrended separately, scaled by the standard deviation and fast Fourier transform algorithm was applied. The power spectra obtained in the manner were smoothed with a median filter and averaged for all the intervals in each experiment. The time series from experiment D, which had the longest duration, was divided into two parts: $D1$ - from 500 min to 2000 min (the period of relatively high gas production) and $D2$ - from 2000 min until the end of the experiment, when the gas production depleted. Figure 13A shows the smoothed frequency distribution curves. They are characterized by the high frequency slope, the position of the peak and the low frequency tail. It can be seen that the peak frequency f_p is nearly the same for experiments A, B, C and D1. These peaks lie in the characteristic frequency range for isolated fractures (dashed line and shaded area on the plot). For experiments D2 and E the peak is shifted in frequency, because experiments A, B, C and D1 were conducted with approximately the same gas production rate, whereas during experiments D2 and E the gas production rate was different.

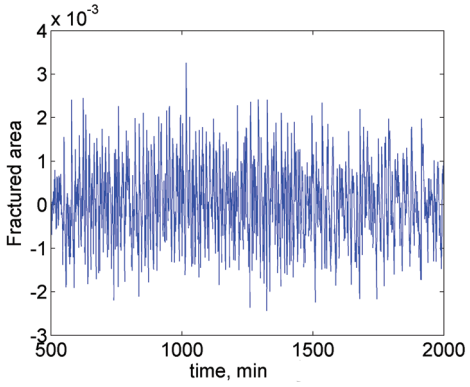

FIG. 12. Fracture area fluctuations after removing the low frequency trend between 500 and 2000 min in experiment D (see Figure 8).

The power spectrum scaled by f_{pi} (Figure 13B) shows three distinct features: 1) A periodic release of gas, with a characteristic frequency that is independent of system size and depends on the gas production rate; 2) a power spectrum of the form $1/f^2$ at high frequencies, which can be explained by the single fracture characteristic behavior (see section IV.2); and 3) a $1/f$ power spectrum over an intermediate range of frequencies, which is thought to be due to collective effects caused by communication of fractures during drainage of a connected fracture network. Using R/S analysis, Hurst exponents of $H \approx 0.5$ at small time scales (high frequencies) and $H \approx 0$ at larger time scales (intermediate frequencies) were measured. These results are consistent with the exponent relationship $\gamma = 1 + 2H$ expected for self-affine fractal processes with power spectra of the form $P(f) \propto f^{-\gamma}$.

IV.4. Spatial correlations

We now describe how different parts of the fracture pattern interact with each other. First, we consider the dynamics of isolated fractures, the fractures which are not connected to other fractures but only drain to the open boundary. The fractures are located at some distance from each other, and this distance is larger than the range of elastic interaction $\lambda = 10 \pm 5$ mm [18] (the elastic Greens function has a long range, $1/r$ form, where r is the distance between the applied force and the displacement response, however, adhesion between the gel layer and the glass plates localizes the stress and stain fields thus reducing the range of interaction). The fracture area time series for each isolated fracture has a characteristic period.

The autocorrelation function of the fracture area time series for isolated fractures allows the fluctuation periodicity to be determined. The autocorrelation function for one of the 12 fractures is presented in the Figure 14A. The fluctuation period was about 10 min. The average of

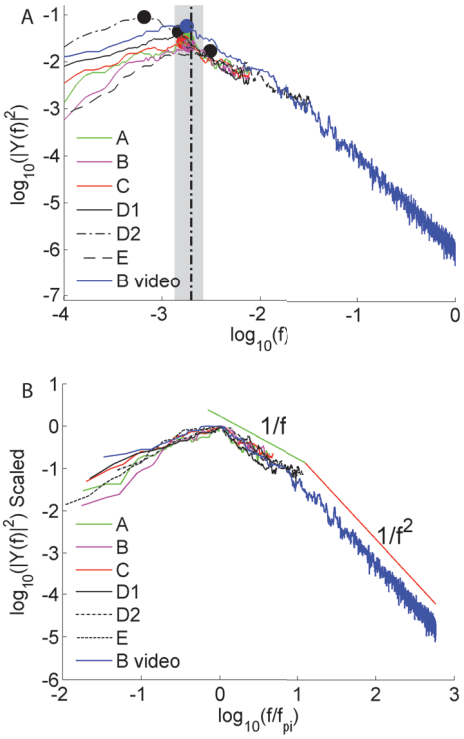

FIG. 13. (Color online) **A**: Power spectra of the fracture area fluctuations for five different experiments. The large dots display the peak height and frequency, f_{pi}, for each experiment. Peak frequencies for experiments A,B,C and D1 lie in the interval $f_{pi} = (1.69 \pm 0.14) \times 10^{-3}$ Hz. The dashed line and shaded area indicate the average and range of characteristic frequencies for isolated fractures $\bar{f}_{ci}$ (Figure 10). **B**: Power spectra of fracture area fluctuations for five different experiments, scaled by the critical frequency f_{pi} and amplitude. All data collapse onto a single master curve.

the autocorrelation functions for 12 isolated fractures in experiment B had a well-defined peak, which corresponds to the average characteristic period, $\tau \simeq 540 \pm 30$ s, for the fracture area fluctuations of all individual isolated fractures in this experiment (Figure 14B). This confirms the results obtained via Fourier analysis (Figure 10).

In order to investigate how isolated fractures interact with each other, a cross-correlation function between all possible pairs of 12 isolated fractures from experiment B was calculated. For two time signals $a_1(t)$ and $a_2(t)$, we computed the following quantity:

$$R(\tau) = \frac{1}{N - |\tau|} \left[\begin{array}{l} \sum_{\tau}^{N} a_1(t) \cdot a_2(t-\tau), \tau > 0 \\ \sum_{|\tau|}^{N} a_1(t+\tau) \cdot a_2(t), \tau < 0 \end{array} \right. \quad (1)$$

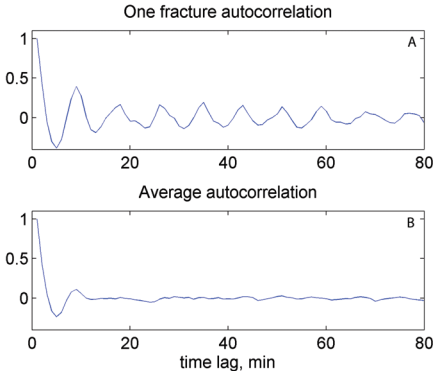

FIG. 14. Autocorrelation function for isolated fractures in the experiment B. **A** An example of the autocorrelation function for one fracture. **B** Average autocorrelation function.

where $t = [0, N]$ is time, and τ is the time lag between the two signals. Figure 15 A,B shows two examples of cross-correlation functions for the fluctuations of two isolated fractures. The opening and closing oscillations of the two fractures were synchronized. Figure 15A shows an example of in-phase oscillations, and Figure 15B shows an example of two fractures which open and close out of phase. For both examples, the average period between cross-correlation function peaks is 480 s, a periodicity similar to that indicated by Figure 10. Because the fracture area

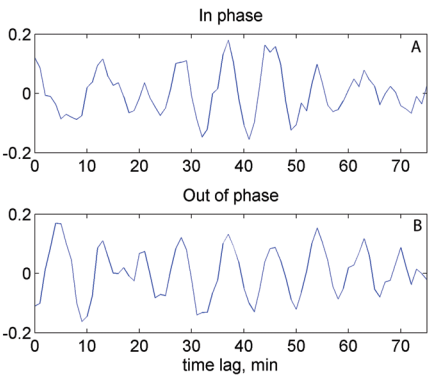

FIG. 15. Cross-correlation function for pairs of isolated fractures in experiment B. **A** The positive values of cross-correlation function during the first time period indicates a zero phase shift in fracture area fluctuations (in phase). **B** The negative values of cross-correlation function during the first time period indicates that fractures open and close with a half period phase shift (out of phase).

variations for different isolated fractures have different initial phase shifts, the average of the cross-correlation functions for all possible pairs does not exhibit any peri-

odicity (Figure 16, green curve).

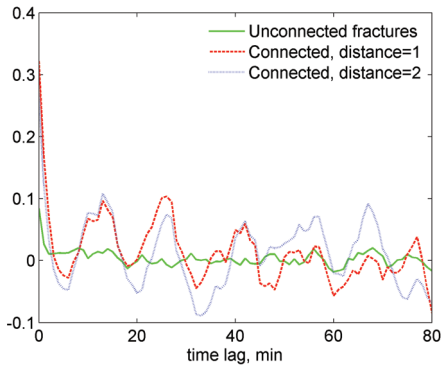

FIG. 16. (Color online) Average cross-correlation function for all pairs of fractures. **Green (solid line)**: The average of cross-correlation functions for all possible pairs of isolated fractures in the experiment B. **Blue (dotted line)**: Average correlation function for fracture branches at a topological distance of $L_t = 1$ in experiment D. **Red (dashed line)**: Average correlation function for fracture branches at a topological distance of $L_t = 2$ in experiment D.

We now address the correlation of fractures that are connected to each other and form a fracture network through which CO_2 can flow from the gelatin to the exterior of the Hele-Shaw cell. We consider fracture branches between intersection points (Figure 6). If two crack branches are connected at a junction point, we call them nearest neighbors and define the topological distance between them as $L_t = 1$. If two crack branches have one neighbor in common, we say that these branches are next-nearest neighbors and that they are separated by a topological distance of $L_t = 2$. In general, if two fractures are connected by a minimum of n other fractures, the topological distance between them is $L_t = n+1$. The fracture branches with topological distances of $L_t = 1$ and $L_t = 2$ can communicate with each other through the junction points. This means that gas can flow from one fracture to another through the junctions.

The cross-correlations between all pairs of fracture branches separated by a topological distance of $L_t = 1$, is indicated by the blue curve in Figure 16. Similarly, the cross-correlations between all pairs of fracture branches separated by a topological distance of $L_t = 2$, is indicated by the red curve in the Figure 16. The instantaneous correlation for nearest neighbors ($L_t = 1$) is larger (30%) than that for fracture branches next-nearest neighbors separated by a topological distance of $L_t = 2$ (25%). The opening and closing of nearest neighbor fractures remain correlated for at least ten periods.

V. CONCLUSION

A simple and reproducible analog experiment was developed to simulate the dynamics of fracture patterns formed in a low permeability elastic solid during internal fluid production and subsequent expulsion. In this model, gelatin was used as a brittle elastic medium, into which dissolved sugar and yeast were incorporated to generate carbon dioxide at a controlled rate. The nucleation of gas bubbles and the diffusion of CO_2 into the bubbles and fractures that evolved from them produced overpressures that created a network of fractures. The gas transport and expulsion out of the system are controlled by intermittent fracture opening and closing. Single fractures that reach the boundary of the Hele-Shaw cell exhibit quasi-periodic opening and closing dynamics, and the periodicity of gas release is independent of system size and fracture length, but depends on gas production rate. The cumulative dynamics of the drainage fracture pattern area has a $1/f^2$ power spectrum at high frequencies, which we explain in terms of single fracture dynamics, and $1/f$ dependence in the intermediate frequency range, that is argued to be due to collective effects in the drainage network. The analysis of spatial correlations in the fracture pattern shows the degree of communication between fractures through fracture junctions that act as valves.

This simple analog model exhibits rich dynamical behaviors resulting from the coupling between the generation and transport of a fluid and the deformation and fracturing of a brittle elastic solid, and it provides a proxy for several natural processes in the Earth's crust in which fluid expulsion is controlled by both internal fluid production and elastic interactions with the surrounding rocks. It was necessary to work with a simple experimental model in order to obtain the large quantities of detailed high resolution information needed to justify the statistical analysis reported here. In the future, we expect that advances in X-ray tomography, acoustic (seismic) imaging, electrical imaging and other methods will enable similar experiments to be conducted with heterogeneous geomaterials under conditions that are more relevant to geosciences and geotechnology applications. While we expect that the results of these experiments will differ in important ways from the results reported here, we also expect that fluctuations in fracture area (fluid volume) with power law spectra, correlations between the opening and closing of neighboring fractures, characteristic fracture opening and closing frequencies and persistent short time scale fluctuations in the fluid volume will likely prove to be generic characteristics of both simple experimental systems and complex natural systems. In both the 3-dimensional experiments of Bons and van Milligen [12] and the quasi-two-dimensional experiments reported here a $1/f$ gas volume/area power spectrum was found at intermediate frequencies and a $1/f^2$ power spectrum was found at high frequencies, and this supports the idea of common generic behavior.

ACKNOWLEDGMENTS

We acknowledge support by the Petromaks program of the Norwegian Research Council. This study was supported by a Center of Excellence grant from the Norwegian Research Council to the Physics of Geological Processes Center (PGP). We are grateful for two thorough and constructive reviews of this paper which helped us to improve the presentation of our work and resolve an important inconsistency in the original data analysis.

[1] E. G. Flekkoy, A. Malthe-Sorenssen, and B. Jamtveit, Journal of Geophysical Research-Solid Earth **107** (2002).

[2] P. R. Cobbold and N. Rodriguez, Geofluids **7**, 313 (2007).

[3] K. Bjorlykke and P. Avseth, *Petroleum Geoscience: From Sedimentary Environments to Rock Physics* (Springer, 2010).

[4] F. Renard, J. P. Gratier, and B. Jamtveit, Journal of Structural Geology **22**, 1395 (2000).

[5] B. Jamtveit, H. Svensen, Y. Y. Podladchikov, and S. Planke, *Physical Geology of High-Level Magmatic Systems*, edited by C. Breitkreuz and N. Petford, Geological Society Special Publication, Vol. 234 (2004) pp. 233–241.

[6] J. A. D. Connolly, M. B. Holness, D. C. Rubie, and T. Rushmer, Geology **25**, 591 (1997).

[7] O. G. Duliu, Earth-Science Reviews **48**, 265 (1999).

[8] F. Renard, European Physical Journal-Applied Physics **60** (2012).

[9] M. Kobchenko, H. Panahi, F. Renard, D. K. Dysthe, A. Malthe-Sorenssen, A. Mazzini, J. Scheibert, B. Jamtveit, and P. Meakin, Journal of Geophysical Research-Solid Earth **116** (2011).

[10] F. Fusseis, C. Schrank, J. Liu, A. Karrech, S. Llana-Funez, X. Xiao, and K. Regenauer-Lieb, Solid Earth **3**, 71 (2012).

[11] W. L. Zhu, G. A. Gaetani, F. Fusseis, L. G. J. Montesi, and F. De Carlo, Science **332**, 88 (2011).

[12] P. D. Bons and B. P. van Milligen, Geology **29**, 919 (2001).

[13] E. Di Giuseppe, F. Funiciello, F. Corbi, G. Ranalli, and G. Mojoli, Tectonophysics **473**, 391 (2009).

[14] O. Galland, S. Planke, E.-R. Neumann, and A. Malthe-Sørenssen, Earth and Planetary Science Letters **277**, 373 (2009).

[15] A. Takada, Journal of Geophysical Research-Solid Earth and Planets **95**, 8471 (1990).

[16] T. Dahm, Geophysical Journal International **142**, 181 (2000).

[17] J. L. Kavanagh, T. Menand, and R. S. J. Sparks, Earth and Planetary Science Letters **245**, 799 (2006).

[18] M. Kobchenko, A. Hafver, E. Jettestuen, O. Galland, F. Renard, B. Jamtveit, P. Meakin, and D. K. Dysthe, Europhysics Letters **102**, 66002 (2013).

[19] N. Rodrigues, P. R. Cobbold, H. Loseth, and G. Ruffet, Journal of the Geological Society **166**, 695 (2009).

[20] S. J. Roberts and J. A. Nunn, Marine and Petroleum Geology **12**, 195 (1995).

[21] J. A. D. Connolly and Y. Y. Podladchikov, Geodinamica Acta **11**, 55 (1998).

[22] G. M. Kavanagh and S. B. Ross-Murphy, Progress in Polymer Science **23** (1998).

[23] F. Hild and S. Roux, Strain **42**, 69 (2006), times Cited: 111.